Performance Limit of Centrifugal Compressor Operating with Non-Ideal Compressible Flow

F. Loekito

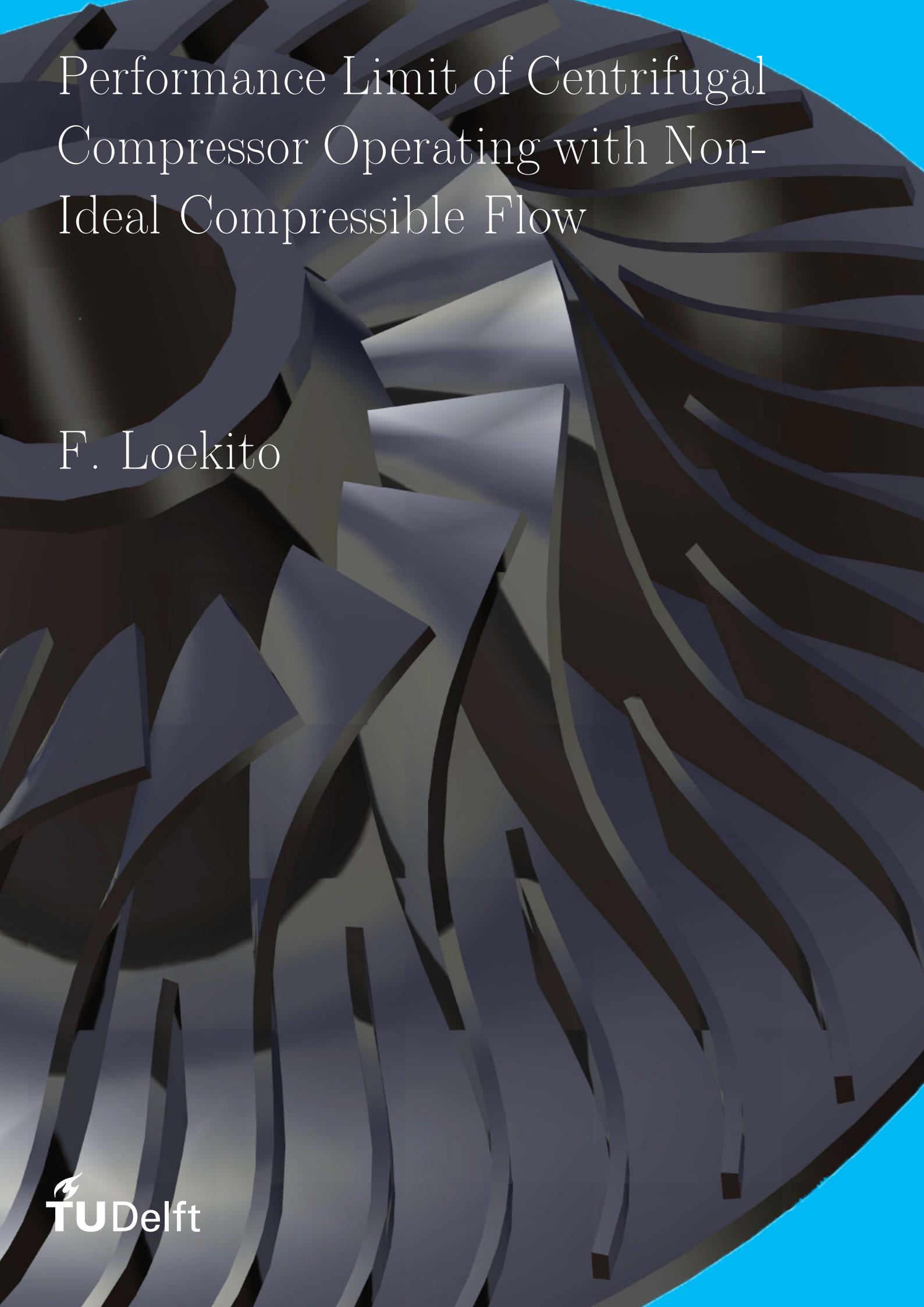

TU Delft

Performance Limit of Centrifugal Compressor Operating with Non-Ideal Compressible Flow

by

F. Loekito

in partial fulfillment of the requirements for the degree of

Master of Science
in Aerospace Engineering

at the Delft University of Technology,
to be defended publicly on Thursday, March 18, 2021 at 14:30.

Student number:	4776887	
Thesis supervisor:	Dr. ir. M. Pini	TU Delft
	ir. A. Giuffre	TU Delft
Thesis committee:	Prof. Dr. ir. P. Colonna	TU Delft
	Dr. F. Avalonne	TU Delft

TU Delft Delft University of Technology

Preface

This master thesis is the result of a year worth of research work and marks the end of my academic career at the faculty of Aerospace Engineering Delft University of Technology. The realization of this work would not have been possible without the support and guidance of many people around me.

I would like, first of all, to express my gratitude to my supervisors, Dr. ir. Matteo Pini and ir. Andrea Giuffre' for their motivation, inspiration and most of all, patience in guiding me throughout this entire thesis project. Their feedback and enthusiasm have motivated me and helped me greatly to achieve a desirable outcome on this project. By extension, I also want to thank the entire Turbomachinery group for the collaboration.

Also, I would like to thanks my family, both in Indonesia and in The Netherlands, in particular my sister, for their understanding and support. I would also like to thank the FPP guys and my friends in the Delft Indonesian Student Association for their encouragement, fun times and brainstorming sessions. Lastly, a particular acknowledgement to San, who helped me a lot during my initial struggle with Python programming.

F. Loekito
Delft, March 2021

Contents

List of Figures

List of Tables

Nomenclature

Acronyms

CFD	Computational Fluid Dynamics
ECS	Environmental Control System
LHS	Left Hand Side terms of the equation
MM	Hexamethyldisiloxane
NICFD	Non-Ideal Compressible Fluid Dynamics
RHS	Right Hand Side terms of the equation

Greek Symbols

α	Absolute flow angle	$^\circ$
β	Relative flow angle, Pressure ratio	$^\circ$, –
χ	Degree of reaction	–
δ	Thickness	m
ϵ_{wake}	Wake blockage width	m
η	Efficiency	–
Γ	Circulation, Fundamental derivative of gasdynamics	m^2/s, –
γ	Heat capacity ratio	–
μ	Dynamic viscosity	$Pa \cdot s$
ν	Kinematic viscosity	m^2/s
Ω	Rotational speed	RPM
ϕ	Flow coefficient	–
ϕ_t	Swallowing capacity	–
ψ	Work coefficient	–
ρ	Density	kg/m^3
τ	Shear stress, Torque	Pa, Nm
ζ	Enthalpy loss coefficient	–

Roman Symbols

$\dot{m}$	Mass flow rate	–
$\dot{m}$	Mass flow rate	kg/m
$\dot{S}$	Entropy generation rate	$J/(K \cdot s)$
A	Area	m^2

a	Speed of sound	m/s
C	Blade camberline length	m
c	Chord length	m
C_c	Sudden expansion coefficient	–
C_d	Boundary layer dissipation coefficient	–
C_f	Darcy friction coefficient	–
c_p	Isobaric specific heat capacity	J/(kg·K)
C_s	Slip coefficient	–
c_v	Isochoric specific heat capacity	J/(kg·K)
D	Diameter	m
D_f	Diffusion factor	–
e	Specific internal energy	J/kg
F	Force	N
g	Tip gap, gravitational acceleration	m, m/s^2
H	Height, Blade height	m
h	Enthalpy	J/kg
l	Length	m
M	Mach number	–
N	Number of active molecular degrees of freedom/molecular complexity	–
p	Pressure	Pa
Q	Volumetic flow rate	m^3/s
q	Heat transfer	J/s
R	Gas constant, Radius	J/kg/K, m
Re	Reynolds number	–
s	Blade pitch	m
U	Peripheral speed	m/s
V	Absolute velocity	m/s
v	Specific volume	m^3/kg
W	Relative velocity	m/s
x_s	Local position in the meridional direction	m
Z	Blade number, Compressibility factor	–
k	Compressor inlet shape factor	–

Superscripts

-	Average value

Subscripts

δ	Boundary layer edge
θ	Flow - in relation to flow length
r	Reduced value; normalized with respect to the critical point - in relation with thermodynamic properties
1s	Inlet optimal value (in relation with relative flow angle)
2s	Impeller isentropic outlet value
ad	Corrected value - in relation to mass flow rate
bl	Blade - in relation with blade thickness
bld	Blade loading
cl	Clearance
df	Disk friction
e	Free stream value
fl	Flow direction
h	Blade hub
hyd	Hydraulic
m	Midspan - Meridional
mix	Mixing
out	Outlet station
p	Polytropic
ps	Pressure side
PT	Pressure-temperature
Pv	Pressure-volume
R	Rotor
rc	Recirculation
S	Stator
s	Blade tip/shroud
sf	Skin friction
ss	Suction side
t	Total properties
tg	Tangential direction
tt	Total-to-total
Tv	Temperature-volume
x	x-direction
y	y-direction
z	z-direction

Station Description

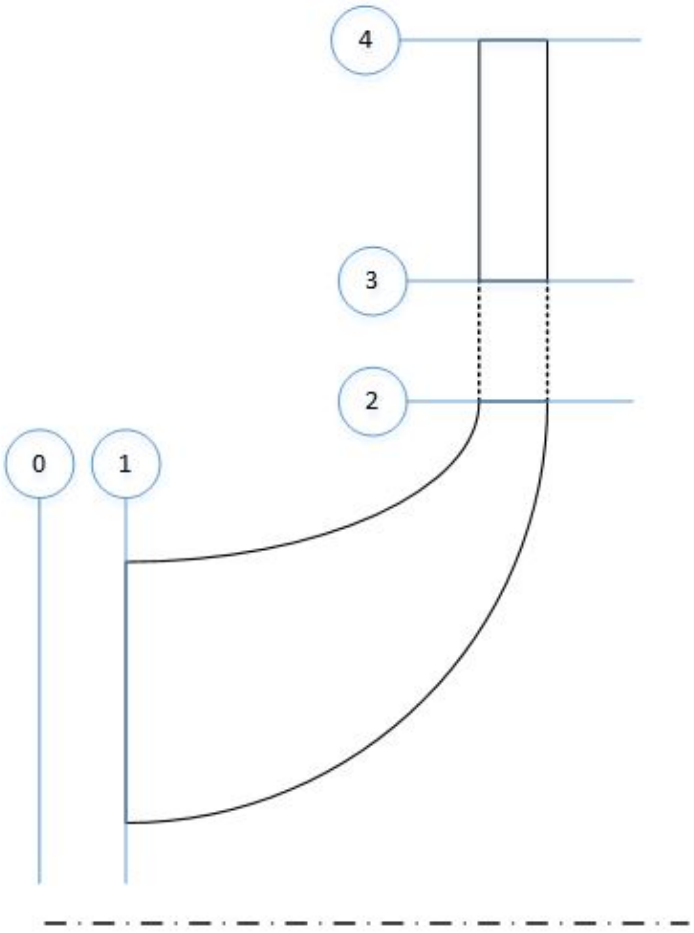

Figure 1: Stations of centrifugal compressor

Table 1: Station description of centrifugal compresor

Station number	Description
0	Ambient
1	Impeller inlet
2	Impeller outlet
3	Diffuser inlet
4	Diffuser outlet

Abstract

The use of centrifugal compressors is widespread in many different industrial applications, namely refrigeration cycles, oil and gas rotating equipments, automotive turbochargers and small aero-engines. Compared to their axial counterpart, centrifugal compressors can provide the same compression ratio within less compression stages, trading-off efficiency with compactness. Current development in this sector involves the tuning of design process to accommodate analysis of turbomachinery operating with non-conventional working fluids that exhibit non-ideal fluid-dynamic behaviour. However, best practices for the preliminary design of centrifugal compressors still rely on the perfect gas assumption. On the other hand, the improvement of the preliminary design tools may result in significant reduction of time and resources spent during the detailed design step by leveraging Computational Fluid Dynamics (CFD). In this scenario, the present research aims to devise guidelines for the preliminary design of centrifugal compressors operating with non-ideal compressible flows by assessing the performance limits of the machine using a meanline design framework, coupled, where possible, to physics-based loss models.

Loss models derived from first principles are preferred to semi-empirical loss correlations as they require less tuning with machine-specific (thus, also working fluid-specific) experimental data. In this work, two major loss sources, namely the blade boundary layer loss and the tip leakage loss, are analyzed in detail. For both loss mechanisms, the physics-based loss model are derived, and their results are compared to CFD results to check their validity and accuracy. Due to time constraints, the remaining loss sources are modelled using semi-empirical correlations available in literature. The outcome of this work are design maps for centrifugal compressors operating with different working fluids and thermodynamic conditions, which highlight the impact of non-ideal compressible fluid dynamics (NICFD) on the optimum design region as well as the maximum theoretical stage efficiency. The novel framework could be further extended and replace the traditional design guidelines based on the perfect gas assumption, aiming to improve compressor preliminary design and contribute to the development of next-generation high-performance turbomachinery.

Keywords: meanline design, centrifugal compressor, NICFD, physics-based loss models, performance limit

1

Introduction

The use and development of compressed-air system and compressors in general are synonymous with continuous industrial growth since the industrial revolution [1]. Specifically, the idea of exploiting centrifugal forces to provide additional pressure increase has been prevalent as early as the 18th century. The earliest known implementation of a centrifugal compressor, a machine which implements this concept, in the aerospace industry was the development of the Whittle turbojet engine (Figure 1.1) back in the 1940s [2]. Nowadays, the centrifugal compressor is also popular in other industrial sectors, such as power generation and refrigeration, oil and gas, as well as in transportation sectors such as automotive turbochargers [4]. In comparison to its axial counterparts, the centrifugal compressor is better for usage with low volumetric flow rate and small geometry, mostly due to the larger efficiency drop in axial compressors with comparable geometry [4]. Radial compressors are now widely used, especially for processes requiring low volumetric flow rate and high-pressure ratio per stages such as in ventilation, liquefaction plants and refrigeration cycles [5]. Ongoing research in the field of refrigeration cycle by the Power and Propulsion group at Delft University of Technology aims to use a high-speed centrifugal compressor in the refrigeration cycle of the Environmental Control System (ECS) for next-generation aircraft and large helicopters. A simplified process flow diagram of such system can be seen in Fig. 1.2 [6].

The various applications of centrifugal compressors imply the use of various working fluid in the compressors, specific to each application. This complexity leads to another recent development in the power generation and refrigeration field, the selection of working fluid as an additional degree of freedom. This breakthrough, however, also bring about more issues. A change in the working fluid may affect the underlying flow

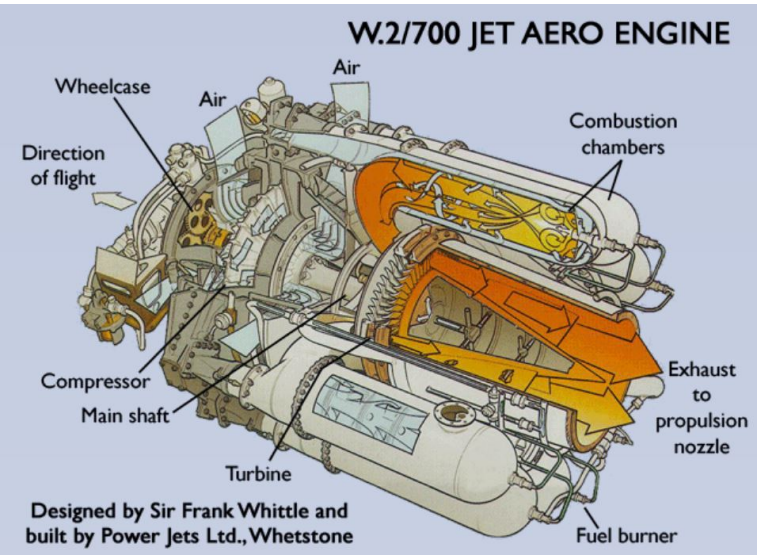

Figure 1.1: Whittle turbojet engine, courtesy of Rolls-Royce, plc. [3]

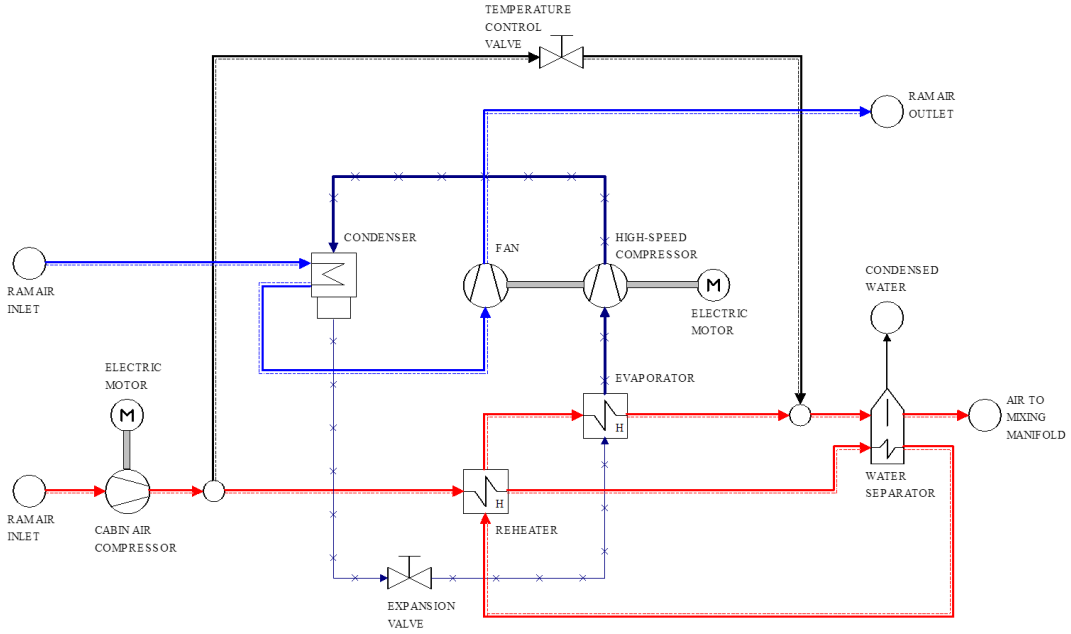

Figure 1.2: Simplified process flow diagram of the refrigeration cycle used for the ECS of next-generation aircraft and large helicopters [6]

dynamics in the impellers. For turbines, at least, as seen in Figure 1.3, for example, changing working fluid also changes its maximum attainable efficiency, which in turn affects the cycle performance.

Thus, especially in rotating equipment, the occurrence of strong thermo-physical fluid property gradients, together with compressibility effects may affect the losses generated within the compressor. The effect of these deviations is not taken into account in the traditional preliminary design guideline, which still relies on perfect gas assumption. As a consequence, the effect of flow non-ideality is not accounted for in the resulting machine preliminary design; i.e. the machine obtained is the same machine which is obtained when designing for a perfect gas, whereas the design should actually be different, as it should also consider NICFD effects.

1.1. Problem Statement

The usual turbomachinery design process starts with the definition of the operating requirements, such as the working fluid, target performance and inlet conditions. This initial step is then followed by a preliminary analysis to get the preliminary dimensions of the machine. The preliminary design phase is then iterated to achieve the target performance while respecting the given design constraints. The outcome of this iterative process is a set of data describing the machine dimensions and shape at a high level. These data are used as the input parameters of a detailed design process, where local parameters are optimized to yield an optimized detailed design. The resulting geometrical parameters are then used to construct a scale model/prototype to be used for experimental validation [5]. This design process is summarized in Figure 1.4. The present work focuses on the preliminary design phase, hence, detailed design optimization is out of the scope of this research.

The development of centrifugal compressor preliminary design itself is a popular research field, with numerous author attempting to come up with their own design routine [8], [9], [10]. All these attempts are based on empirical or semi-empirical formulation derived from polynomial regression of experimental studies on several sample compressors. A design map is also available as the end-result of these works [11]. However, the aforementioned problems with working fluid have not been attempted to be tackled. The empirical approaches mentioned earlier are based on validation on experimental data of compressors within a specific range of working parameters and most importantly with air as a working fluid. These data are not reliable for non-conventional applications, like micro high-speed centrifugal compressors operating with refrigerants. In other words, these empirical methods lack validation utilizing high fidelity models and a broad array of experimental data. The practice to employ these semi-empirical loss models to predict the performance of machines operating in the NICFD regime is, therefore, questionable. This knowledge gap leads to inaccurate

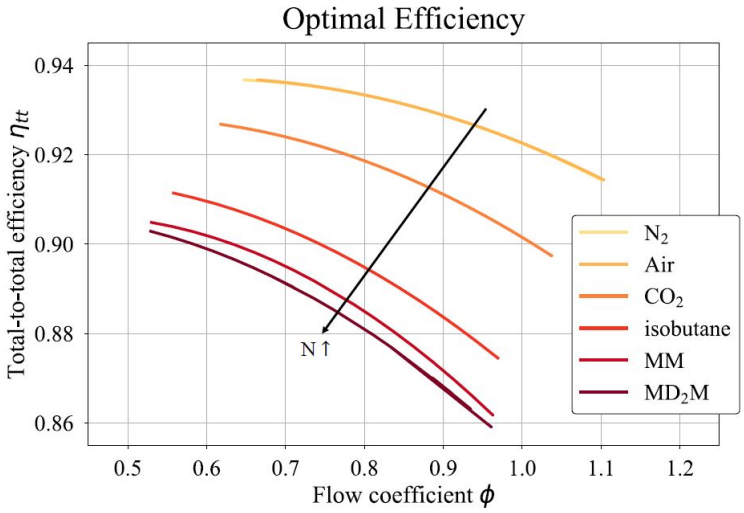

Figure 1.3: Variation of the maximum achievable efficiency for turbines operating with fluids of increasing molecular complexity [7]

centrifugal compressor preliminary design. This design inaccuracy causes more time and computational resources to be spent during detailed design optimization. Moreover, if the inaccurate preliminary design is far from the optimum design, it may also cause the optimized detailed design to converge towards the local optimum rather than the global optimum.
Hence, this work aims to bridge this knowledge gap by providing a design framework coupled to loss models derived from first principles to be used for unconventional centrifugal compressor applications. The framework developed is a one-dimensional method based on similarity analysis where classical parameters, such as the duty coefficients and thermodynamic isentropic exponents are used. The work also encompasses a val-

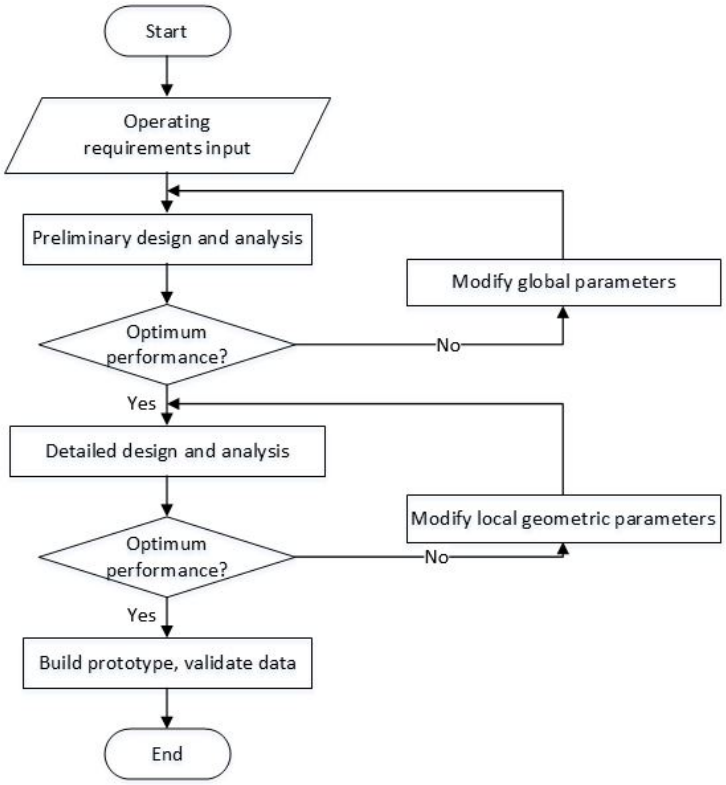

Figure 1.4: Complete turbomachinery design routine [5]

idation step by means of high-fidelity CFD. Based on the background and past works, the research question and objective of this work can then be formulated as follows.

1.2. Research Question

The main research questions to be answered in reaching the project goal is as follow:

Is it possible to formulate generic design guidelines for centrifugal compressors accounting for the effects of flow non-ideality and compressibility?

Does NICFD affect the optimum design region and the maximum theoretical machine efficiency?

Several sub-questions arise from the main research questions:

- What are the key elements towards the development of a preliminary design framework based on dimensional analysis for centrifugal compressors?
  - Which non-dimensional global compressor parameters would be suitable as the input parameter of the framework?
  - Which parameter should be used to characterize the non-ideal compressible fluid dynamics (NICFD) effects?
- What is the physics behind loss generation inside centrifugal compressor flow passage?
  - What kind of loss production mechanisms are happening in the flow?
  - Which parameters should be used to characterize each loss mechanism?
- What is the effect of flow non-ideality on the centrifugal compressor design?
  - What is the effect of fluid molecular complexity on each loss production?
  - What is the effect of flow non-ideality and compressibility on loss production?

1.3. Research Objective

The main research objective of this thesis is:

> "To derive generic design guidelines for centrifugal compressors operating with non-ideal compressible flows by investigating the performance limits of the machine using a 1D design framework coupled to physics-based loss models".

The sub-goals of this projects are:

- Development of a 1-D design framework for centrifugal compressors operating with a generic working fluid.
- Development and implementation of physics-based loss models
- Comparison with high-fidelity CFD result
- Investigation of the impact of NICFD on centrifugal compressor optimal design and performance

2

Similitude Theory

This chapter introduces the method used to explore the centrifugal compressor design space. Dimensional analysis, as the basis of similitude theory, is discussed. Then, the general formulation of the similarity equation is introduced and described in details.

2.1. Dimensional Analysis

The dimensional analysis is a procedure where a large group of variables representing a physical phenomenon is reduced to a smaller group of dimensionless variables. When the number of independent variables is not too great, the effort needed to perform experimental analysis between the variables could be reduced. Applying this approach for turbomachinery analysis also allows performance prediction based on scale model testing, and the determination of the machine's performance based on a specified range of a group of non-dimensional variables [4]. The latter, which is usually represented in maps and graphs such as efficiency and performance maps, is crucial for the further understanding of the machine's general behaviour with respect to said variables.

The dimensional analysis is well-explained by the Buckingham-Pi theorem[12].Take, for example, an arbitrary physical equation with n variables:

$$u_1 = f(u_2, u_3, ..., u_n) \tag{2.1}$$

A set of reference dimension can then be chosen, for example, M, L, T; F, L, T; etc. Using the M, L, T system, for example, r (the required number of reference dimension) is equal to 3. This number also corresponds to the number of repeating variables required to represent the original equation. In this case, the relationship between the original variables and the Π reads:

$$\Pi_1 = \frac{u_1}{{u_2}^{\alpha} u_3^{\beta} {u_4}^{\gamma}} \tag{2.2}$$

Rearranging the original equation into a set of dimensionless pi (products) terms:

$$\Pi_1 = \phi(\Pi_2, \Pi_3, ..., \Pi_{n-r}) \tag{2.3}$$

An example of this analysis is as follows. Consider an incompressible flow through a straight horizontal circular pipe, as seen in Figure 2.1 The pressure drop along the pipe is affected by the fluid density (ρ), the

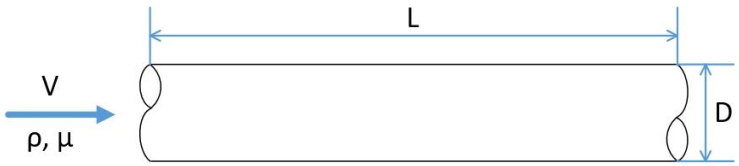

Figure 2.1: Incompressible flow through a straight horizontal circular pipe

fluid velocity (V), the fluid viscosity (μ) and the pipe geometry (D and L). The pressure drop can be written as a function of five parameters:

$$\Delta p = f(D, L, \rho, \mu, V) \tag{2.4}$$

Using the M, L, T system $r = 3$ and:

$$\begin{aligned} \Delta p &= ML^{-1}T^{-2} \\ D &= L \\ L &= L \\ \rho &= ML^{-3} \\ \mu &= ML^{-1}T^{-1} \\ V &= LT^{-1} \end{aligned} \tag{2.5}$$

choosing ρ, V and D as the repeating variables ($r = 3$, hence, 3 repeating variables required), the equation can be rewritten as:

$$\begin{aligned} \Pi_1 &= \frac{\Delta p}{\rho^{\alpha} V^{\beta} D^{\gamma}} \\ M^0 L^0 T^0 &= (ML^{-1}T^{-2})(ML^{-3})^{-\alpha}(LT^{-1})^{-\beta}(L^{-\gamma}) \end{aligned} \tag{2.6}$$

solving for α, β and γ, Π_1 can be rewritten as:

$$\Pi_1 = \frac{\Delta p D}{\rho V^2} \tag{2.7}$$

Repeating the last step for every variables in the original equation, the other variables can be grouped as:

$$\begin{aligned} \Pi_1 &= \phi(\Pi_2, \Pi_3) \\ \Pi_2 &= \frac{\rho V D}{\mu} \\ \Pi_3 &= \frac{L}{D} \\ \frac{\Delta p D}{\rho V^2} &= \phi\left(\frac{\rho V D}{\mu}, \frac{L}{D}\right) \end{aligned} \tag{2.8}$$

From this example, it is clear that by using this dimensional analysis framework, the number of required variables can be reduced by r. This reduction in independent variables translates to a lower number of experiments needed to characterize the investigated physical phenomenon.

2.2. Similitude Theory Implementation on Turbomachinery

After previously discussing the basics of dimensional analysis theory, it is then used to define the similitude equation for turbomachinery. For the incompressible flow limit case, the Bernoulli's equation is defined:

$$p_{out} - p_{in} = \rho g H \tag{2.9}$$

The pumping power can be defined similarly:

$$P = \dot{m} g H = \rho Q g H \tag{2.10}$$

Following this definition, the hydraulic efficiency can be written as:

$$\begin{aligned} \eta &= \frac{W_{pump}}{W_{shaft}} \\ &= \frac{\rho Q g H}{\tau N} \end{aligned} \tag{2.11}$$

where τ and N are the shaft input torque and rotational speed respectively. Thus, using the dimensional analysis, η can be rewritten as:

$$\eta = f(Q, gH, \rho, N, D, \mu) \tag{2.12}$$

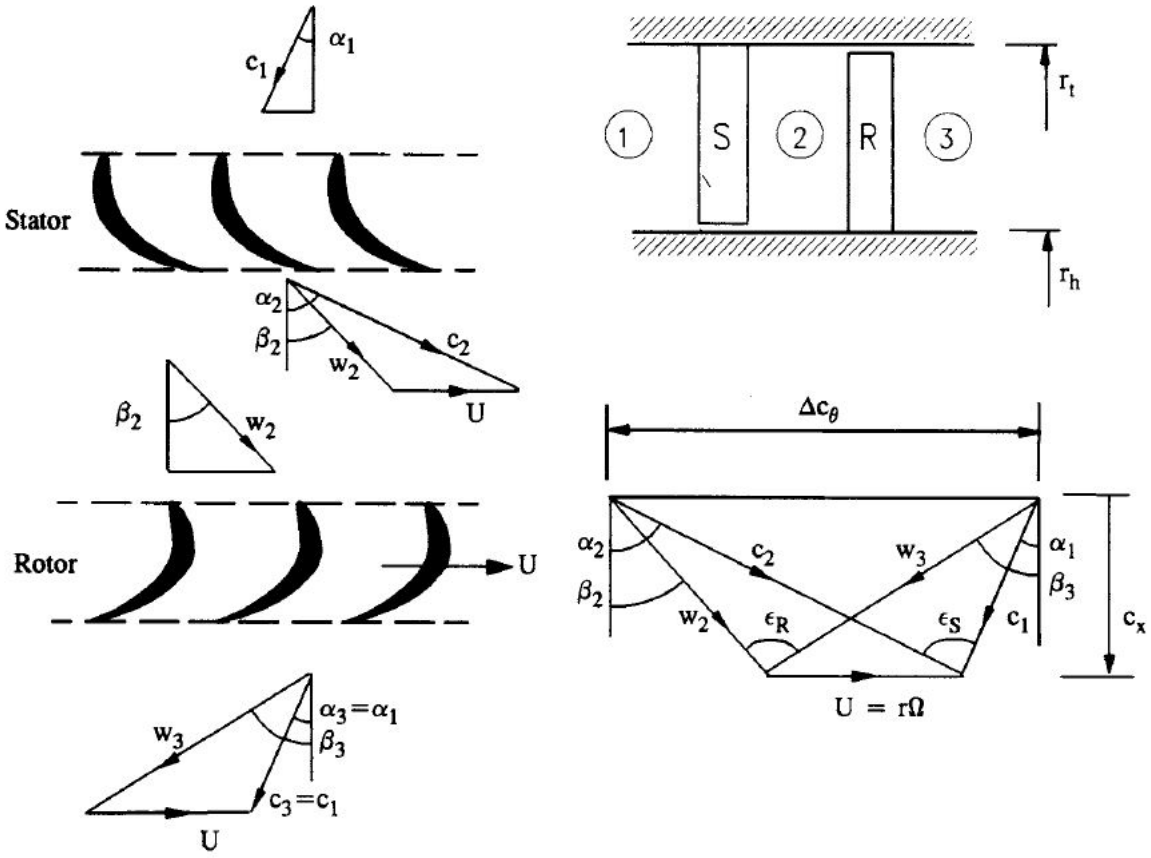

Figure 2.2: Axial turbine velocity triangles, $c = v$ = absolute velocity [13]

Although not present in the above correlation, μ is added in the equation to characterise the viscous effect of the working fluid. Using a non-dimensional form, equation 2.12 can be written as:

$$\begin{aligned} \eta &= f(\phi, \psi, Re) \\ \phi &= \frac{Q}{ND^3} \\ \psi &= \frac{gH}{N^2D^2} \\ Re &= \frac{\rho ND^2}{\mu} \end{aligned} \tag{2.13}$$

This relationship is the classical similarity equation for turbomachinery with incompressible flow. For turbomachinery with compressible flow, the classical similarity equation is mainly constructed by variables governing the velocity triangles and the losses. As an example, the generic classical similarity equation for a single stage of an axial turbine is shown in Figure 2.2 From the velocity triangle, it is clear that the shape of the velocity triangle is governed by three independent variables:

- Work coefficient/stage loading factor, $\psi = \frac{\Delta h_t}{U^2}$
- Flow coefficent, $\phi = \frac{v_m}{U}$
- Degree of reaction, χ

The computation of velocity triangle based on these three variables will be discussed in-depth on Subsection 5.2. The losses in a turbomachine, on the other hand, is governed by the flow Mach number, Reynolds number and the machine geometry. Putting the variables together, the efficiency of an axial turbine operating with perfect gas is formulated as:

$$\eta_{tt} = f(\phi, \psi, \chi, M, Re, \sigma) \tag{2.14}$$

Table 2.1: Non-dimensional parameters used in the classical similarity equation for axial turbine

Parameter	Formulation
Work/stage loading coefficient	$\psi = \frac{\Delta h_t}{U^2}$
Flow coefficient	$\phi = \frac{v_m}{U}$
Degree of reaction	$\chi = \frac{\Delta h_R}{\Delta h_{tt}}$
Reynolds number	$Re = \frac{\rho v l_\theta}{\mu}$
Mach number	$M = \frac{v}{a}$
Shape	σ, see Table

Table 2.2: Non-dimensional geometrical parameter for axial turbine

Parameter	Formulation
blade solidity	$\frac{c}{s}\Big\vert_{S,R}$
blade axial chord-pitch ratio	$\frac{c_{ax}}{s}\Big\vert_{S,R}$
blade camberline length-pitch ratio	$\frac{C}{s}\Big\vert_{S,R}$
tip gap-blade height ratio	$\frac{g}{H}\Big\vert_{S,R}$
midspan diameter ratio	$\frac{D_{inlet,m}}{D_{outlet,m}}\Big\vert_{S,R}$
aspect ratio	$AR_R = \frac{H_{R,inlet}+H_{R,outlet}}{2c_{ax,R}}$
	$AR_S = \frac{H_{S,inlet}+H_{S,outlet}}{2c_{ax,S}}$

The detailed formulation of each parameter can be seen in Table 2.1 The work and the flow coefficients control the amount of flow deflection in axial turbines. Based on the formulation, a higher ϕ implies a more axial flow (less deflection) and vice versa. On the other hand, a higher ψ means a higher blade loading, and hence, the flow deflection. χ, as the formulation describes, is a ratio between the rotor loading to the overall stage loading; a higher χ implies a higher loading in rotor compared to the stator. These three variables are further called duty coefficients. Furthermore, concerning losses, Reynolds number is the ratio between the flow inertial and viscous forces, and thus, can distinguish laminar, transitional and turbulent flow regimes. Mach number is used to distinguish the subsonic and supersonic flow regime and is also where flow compressibility can be taken into account in the analysis. The last parameter, σ, is a collection of relevant non-dimensional geometrical parameters. For axial turbines, the relevant shape parameters are listed in Table 2.2. The geometrical parameters grouped as σ is different for each type of machine, usually depends on the requirements of the implemented loss models. The parameters in Table 2.2 is based on the work of Giuffre' which implements physical loss models for axial turbine performance estimation [7].
A limit case of this framework was performed by Smith[14]. His analysis provides a useful tool in axial turbine preliminary design, Smith's chart (Figure 2.3). Recalling 2.14, the axial turbine stage efficiency is given as:

$$\eta_{tt} = f(\phi, \psi, \chi, M, Re, \sigma)$$

As mentioned earlier, Smith's analysis is a limiting case of the general similitude analysis. His hypotheses in constructing his analysis are:

- χ = 0.5 (symmetric rotor-stator blades)

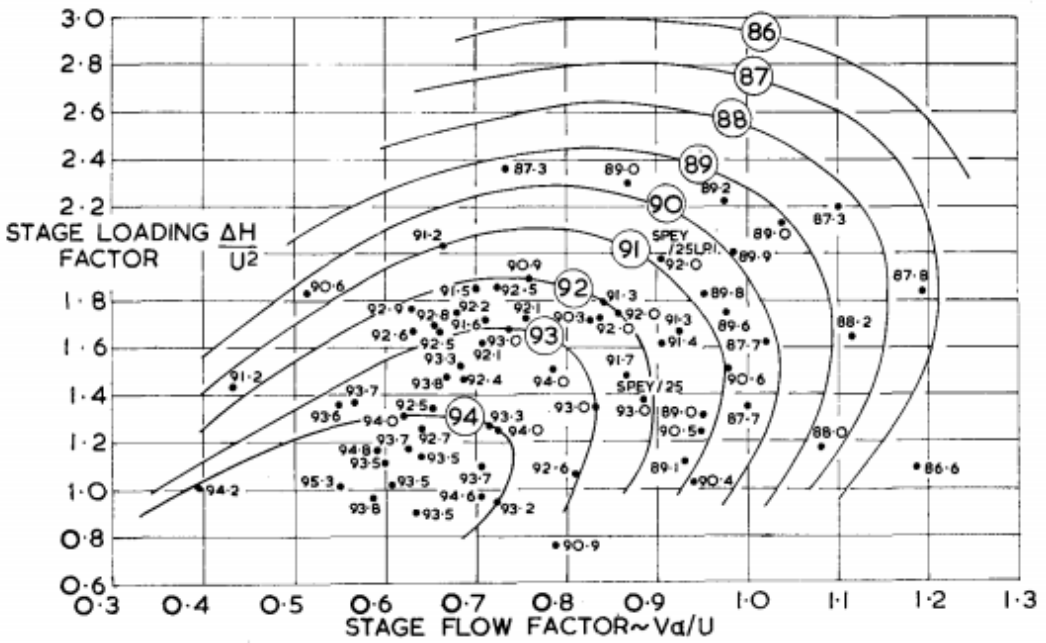

Figure 2.3: Smith's Chart [14]

- M = 0.6 - 1.0 (no shock loss)
- Working fluid = air
- No leakage losses
- Analysis at blade midspan
- Turbine uses repeated stage design
- Machine type = axial turbines

From these hypotheses, Smith reduced equation 2.14 into:

$$\eta_{tt} = f(\phi, \psi) \tag{2.15}$$

The generalized non-ideal similarity equation of a turbomachine, which takes into account generic working fluid and thermodynamic regime, can then be extended from the classical similarity equation in Equation 2.14. As will be explained in-depth in Chapter 3, the behaviour of gas is affected by the local thermodynamic state of the gas. Determining this state requires not only the pressure ratio of the system but also the thermodynamic state of the fluid at the inlet of the machine. To include the thermodynamic properties describing this state in the analysis, the value of their ratio to the critical point's value can be taken, i.e.

$$p_r = \frac{p_{t0}}{p_c} \text{ and } T_r = \frac{T_{t0}}{T_c} \tag{2.16}$$

Another simpler way to summarize these inlet thermodynamic parameters is to introduce the γ_{pv}, the isentropic pressure-volume exponent. The average of this parameter's value along the thermodynamic transformation in the flow can conveniently replace the two thermodynamic parameters (T_r and p_r). This exponent is elaborated in detail in Subsection 3.2. Moreover, once the duty variables (ϕ and ψ) is determined, the Mach number is then a function of the pressure ratio, as fixing all three parameters values means determining the turbomachines velocity triangle. Moreover, based on the works of Macchi [15], the pressure ratio can also take into account the fluid compressibility effect, as it is closely related to volumetric flow ratio. Furthermore, in practice, it is usual to know the boundary condition in term of the target pressure ratio in designing a compressor. Summarizing these additional considerations, the generalized non-ideal similarity equation for an axial turbine can be written as:

$$\eta_{tt} = f(\phi, \psi, \chi, \beta_{tt}, \gamma_{pv}, Re, \sigma) \tag{2.17}$$

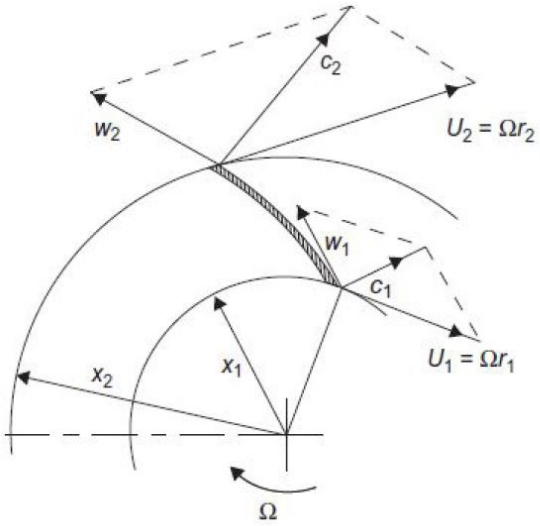

Figure 2.4: Centrifugal compressor impeller velocity triangle, $c = v$ = absolute velocities [4]

It can be noted that Equations 2.17 and 2.14 are quite similar; the parameters governing both equations could be grouped into duty coefficients (governing the velocity triangles), Reynolds number (viscous effect), parameters relating to flow compressibility (β_{tt} or Mach number) and geometrical parameters, wit the addition of local thermodynamic parameter in Equation 2.17 to take into account the flow non-ideality (implemented alongside the pressure ratio). In fact, Equation 2.17 could also be implemented for radial machines performance analysis, albeit with several changes during the implementation. For a centrifugal compressor with perfect gas working fluid, as seen in Figure 2.4, the total-to-total efficiency is affected by these 11 design variables[13]:

$$\eta_{tt} = f(v_{s2}, w_\infty, U_2, r_1, r_2, A_1, A_2, \Delta h_o, (\Delta p_{oR})_{loss}, \rho, \mu) \tag{2.18}$$

v_{s2} and U_2 are the meridional and blade peripheral speed at the rotor (impeller) exit respectively. Together with w_∞, they account for the effect of velocity triangles to the efficiency. r_1, r_2, A_1 and A_2 are the compressor annulus geometry (inlet and outlet radius and areas). The next two terms account for the head rise in the fluid and the head loss respectively. Lastly, μ and ρ are the fluid physical properties (viscosity and density). Using dimensional analysis, this equation can be rewritten into:

$$\eta_{tt} = f(\phi, \psi, M, Re, \sigma) \tag{2.19}$$

Where, again, σ represents the compressor's geometrical parameters. Using similar arguments as in the axial turbine case, the generalized non-ideal similarity equation for a centrifugal compressor could be formulated as:

$$\eta_{tt} = f(\phi, \psi, \beta_{tt}, \gamma_{pv}, Re, \sigma) \tag{2.20}$$

Equation 2.20 is very similar to Equation 2.17 but without the degree of reaction. This omission is understandable, as in Figure 2.4 only the impeller is taken into account. Furthermore, the parameter vector σ is also different in centrifugal compressors.
The choice of relevant parameters to be included in the collective σ is numerous. To make an efficient model, it is important to focus on the ones affecting the machine's efficiency saliently. Referring to an empirical model by Oh et al. [10], those parameters are:

- Hydraulic/flow/blade camberline length, l_θ
- Blade height, H
- Tip gap, g
- Blade thickness δ_{bl}
- Outlet radius r_2

- Inlet hub and tip/shroud radius $r_{1h,s}$
- Blade number Z

This set of geometrical parameter is enough to get a good estimate of the centrifugal compressor's performance in the preliminary design stage. Non-dimensionalizing those parameters will yield:

$$\sigma = \left[k, Z, \frac{D_{1s}}{D_2}, \frac{g}{H_2}, \frac{\delta_{bl} Z}{2\pi r_2}, \frac{l_\theta Z}{2\pi r_2} \right] \tag{2.21}$$

Where:

$$k = 1 - \left(\frac{D_{1h}}{D_{1s}} \right)^2 \tag{2.22}$$

An additional remark, the form of flow coefficient used in the analysis ($\phi_2 = \frac{V_{m2}}{U_2}$) is rarely used in practice in radial turbomachinery [16]. This form of flow coefficient tends to be used when an emphasis on the kinematic similarity of the flow at different rotational speeds is to be made. The reason for this decision is that two radial compressor stages with similar outlet diameter mean they will have a similar value of ϕ_2. However, due to the difference in internal flow areas (for example, due to the result of different outlet widths), the compressors may not have the same flow capacity [16]. To identify this difference in cases with similar velocity triangles, an additional non-dimensional parameter is needed. One choice is to replace the usual flow coefficient ϕ with swallowing capacity (ϕ_{t1}). This parameter relates the actual mass flow to the mass flow which would occur if the total flow were to pass through a virtual area A with the velocity of the reference blade speed and the density of the inlet total conditions [16]. The reference area is defined as $A = D_2^2$, hence:

$$\phi_{t1} = \frac{\dot{m}}{\rho_{t1} A U_2} = \frac{\dot{m}}{\rho_{t1} D_2^2 U_2} \tag{2.23}$$

This choice of flow coefficient form is often used when aerodynamicist would like to emphasise the relative flow capacity of different designs when referred to the same nominal impeller size and tip speed, as the parameter characterized swallowing capacity of different machines based on their tip speed and tip diameter. As a final remark, although there exist various ways to define the design parameters, such as flow coefficient, the usage choice comes back to the designer and their main design purpose. In essence, different parameter choice will not cause a great shift in the established model and predicted performance and design. Due to this reasons, in this work the flow coefficient form of ϕ_{t1} will be adopted, simply to enable easier comparison with existing performance map such as that of Figure 4.2 [11].
With all these additional parameters, Equation 2.20 can be rewritten into:

$$\eta_{tt} = f(\phi_{t1}, \psi, \beta_{tt}, \gamma_{pv}, Re, \sigma) \tag{2.24}$$

To summarize, it can be concluded that the similarity conditions of a turbomachine can be grouped into four categories:

- Kinematic similarity = same velocity triangles, i.e duty coefficients
- Dynamic similarity = same Reynolds and Mach number
- Geometric similarity = same geometrical dimensionless parameters
- Thermodynamic similarity = same thermodynamic behavior, characterized by the average value of γ_{pv} along the thermodynamic process.

3

Non-Ideal Compressible Fluid Dynamic

The present chapter aims to give a more rigorous description of NICFD, complemented with an example of its impact on the optimal design of the impeller of centrifugal compressors. In the first section, the concept of Non-Ideal Compressible Fluid Dynamics (NICFD) is introduced. The second section follows by specifying the influence of NICFD in the turbomachinery dimensional analysis.

3.1. Introduction to NICFD

To understand NICFD concept, first, the difference between the ideal and the non-ideal thermodynamic regime must be known. In the ideal regime, fluids follow the well-known ideal gas equation:

$$pv = RT \tag{3.1}$$

In this regime, it is assumed that there are no interaction forces between the gas molecules and that the volume occupied by the molecule itself is negligible relative to the container. As there is no interaction between the molecules, the thermodynamic properties depend on the molecules kinetic energy. The pressure in an ideal gas is determined by the rate of momentum transfer per unit area as the molecules collide with the container boundary, hence, the pressure depends on the molecules translational velocity alone. The temperature, is also proportional to the molecules translational velocity [17]. On the other hand, when real gas is considered, the intermolecular forces and interactions affect the gas properties. The attractive and repulsive forces between the molecules, for example, cause the deviation in the pressure value with respect to that calculated using the ideal gas law, causing the ideal gas law to be invalid. The degree of a fluid non-ideality can be identified by measuring the value of two parameters, namely the compressibility factor (Z) and the fundamental derivative of gasdynamics (Γ).

The compressibility factor (Z) is defined as:

$$Z = \frac{pv}{RT} = \frac{v}{v_{ideal}} \tag{3.2}$$

It captures the departure of volumetric behaviour of fluid from the ideal case [17]. Figure 3.1 shows the contour of the compressibility factor in the T-s diagram of Toluene. As seen in the figure, in the dense gas region (near the critical point), Z assumes value lower than 1. Conversely, approaching the thermodynamic region where Z is close to 1 (dilute gas region), the fluid exhibits behaviour resembling that of an ideal gas.

The fundamental derivative of gasdynamics (Γ) is defined as the change in the sound velocity with pressure or density at constant entropy [18]. It can be expressed as:

$$\Gamma = 1 - \frac{a}{v}\left(\frac{\partial a}{\partial v}\right)_s \quad \text{or} \quad \Gamma = 1 + \frac{a}{v}\left(\frac{\partial a}{\partial P}\right)_s \tag{3.3}$$

As suggested by its definition, Γ governs the relation between Mach number and flow properties variation. In isentropic flows, for example, the relationship between change in Mach number and a variation in flow

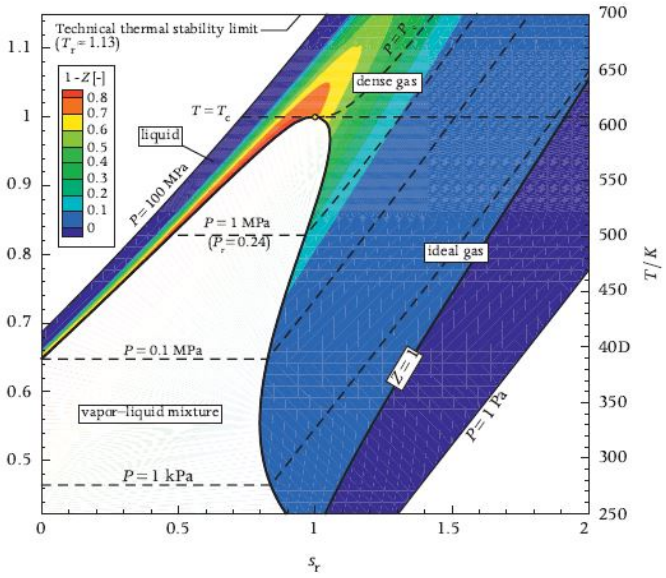

Figure 3.1: T–s state diagram for toluene with contours of compressibility factor, Z. [17]

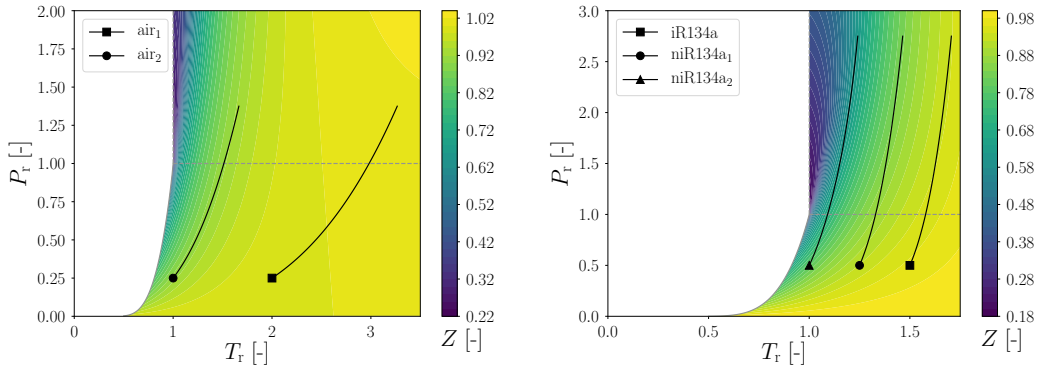

(a) (b)

Figure 3.2: Compressibility factor along the isentropic compression in (a) Air; (b) R134a - reduced inlet properties as in Table 3.1. The isentrophe and thermodynamic parameter value is calculated using a program currently being developed at the Power and Propulsion group at Delft University of Technology

velocity reads [18]:

$$\frac{dV}{V} = \frac{dM/M}{1+(\Gamma-1)M^2} \tag{3.4}$$

The flow regime where $\Gamma \geq 1$ is identified as classical ideal gasdynamics. In this regime, the Mach number increases monotonically with velocity. For an ideal gas, the fundamental derivative of gasdynamics can be written as:

$$\Gamma = \frac{\gamma+1}{2} \tag{3.5}$$

In cases where $0 < \Gamma < 1$, the flow exhibits real gasdynamic behaviour. The term $\frac{\partial a}{\partial P}$ has to be negative to yield a Γ within this values. Hence from Equation 3.3, it can be inferred that the speed of sound, and in turn the Mach number, decreases with increasing pressure, as opposed to what is observed in the ideal regime. Finally, the thermodynamic region where $\Gamma < 0$ is identified as the so-called BZT (Bethe-Zel'dovich-Thompson) region, which is located in the proximity of very complex fluid critical point and is characterized by non-classical gasdynamics behaviour [18].

To better understand the impact of fluid non-ideality on its thermodynamic properties, isentropic compression processes of air and R134a (1,1,1,2-tetrafluoroethane) in an ideal diffuser characterized by the same

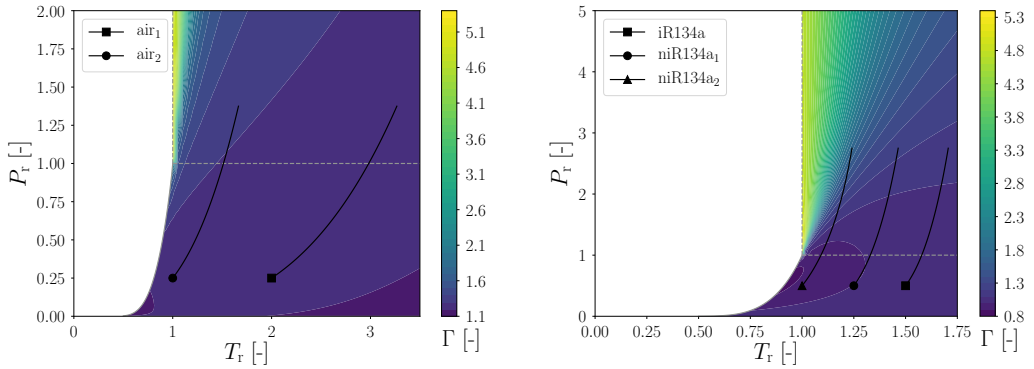

(a) (b)

Figure 3.3: Fundamental derivative of gasdynamics along the isentropic compression in (a) Air; (b) R134a - reduced inlet properties as in Table 3.1. The isentrophe and thermodynamic parameter value is calculated using a program currently being developed at the Power and Propulsion group at Delft University of Technology

Table 3.1: Reduced inlet conditions used for isentropic compression in Figures 3.2 and 3.3

Fluid	**Case name**	Inlet reduced properties	
		p_r	T_r
air	air_1	0.25	2.0
	air_2	0.25	1.0
R134a	iR134a	0.5	1.5
	niR134a_1	0.5	1.25
	niR134a_2	0.5	1.5

compression ratio ($\beta_{ts} = 5.5$) performed in the dilute and dense gas region is shown in the following Figures 3.3 and 3.2. The reduced inlet condition of the isentropic compression processes shown in Figures 3.2 and 3.3 is listed on Table 3.1 Along the isentropic compression processes, the Mach number and density are analyzed using the ideal gas equation for the ideal gas analysis and the multi-parameter equation of state compiled in a thermodynamic library for the real gas analysis. To compute the Mach number using the ideal gas approach, the isentropic total-static pressure relation can be used:

$$\frac{p}{p_t} = \left(1 + \frac{\gamma - 1}{2} M^2\right)^{\frac{-\gamma}{\gamma - 1}} \tag{3.6}$$

Modifying Equation 3.6 as a function of compression ratio, it can be rewritten into:

$$\frac{p_2}{p_1} = \beta = \frac{\left(1 + \frac{\gamma_1}{2} M_1^2\right)^{\frac{\gamma_1}{\gamma_1 - 1}}}{\left(1 + \frac{\gamma_2}{2} M_2^2\right)^{\frac{\gamma_2}{\gamma_2 - 1}}} \tag{3.7}$$

To provide an explicit expression of M_2, one assumption has to be implemented on Equation 3.7. It is assumed that the gas being analyzed is a perfect gas with constant c_p, c_v and γ. The equation can then be rewritten into:

$$M_2 = \sqrt{\frac{2}{\gamma - 1}\left(\frac{1 + \frac{\gamma}{2} M_1^2}{\beta^{\frac{\gamma - 1}{\gamma}}} - 1\right)} \tag{3.8}$$

On the other hand, for the real gas approach, using the conservation of total enthalpy, the outlet velocity can be written as:

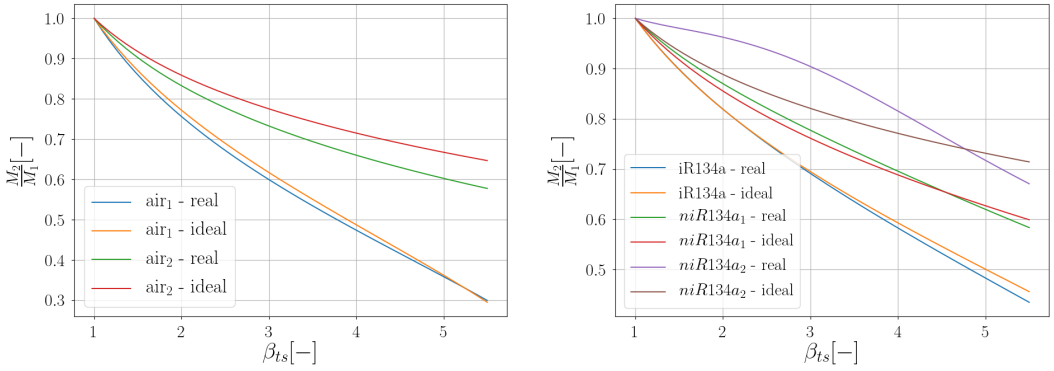

(a) (b)

Figure 3.4: Mach number trend of (a) air and (b) R134a along isentropic compression for isentropic compression in Figure 3.2, calculated with ideal gas law and real gas multi-parameter equation of state

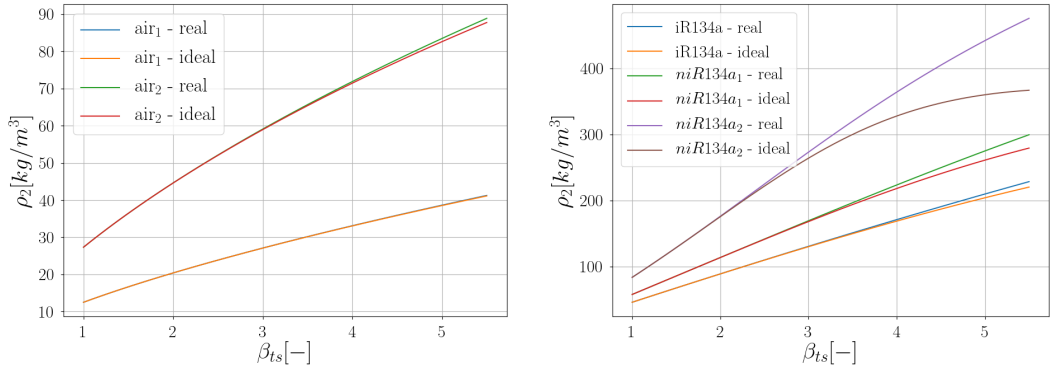

(a) (b)

Figure 3.5: Density trend of (a) air and (b) R134a along isentropic compression for isentropic compression in Figure 3.2, calculated with ideal gas law and real gas multi-parameter equation of state

$$
\begin{aligned}
V_2 &= \sqrt{V_1^2 + 2\left(h_1 - h_2\right)} \\
&\text{and} \\
M_2 &= \frac{v_2}{a_2} \\
&\text{where} \\
h_2, a_2 &= f\left(p_2, s_1, fluid\right) \\
h_1 &= f\left(p_1, T_1, fluid\right) \\
s_2 &= s_1
\end{aligned}
\tag{3.9}
$$

As in both Equations 3.8 and 3.9 M_2 is a function of inlet velocity, it is important to provide an arbitrary inlet velocity value. In a diffuser, the kinetic energy is transformed into pressure rise, hence, the arbitrary inlet velocity value is to make sure the term inside the square-root in both equations to be always positive. Another thermodynamic property which can be compared is the density. The ideal gas outlet-inlet density ratio can be computed by rearranging the ideal gas law:

$$
\frac{\rho_2}{\rho_1} = \beta^{\frac{1}{\gamma}} \tag{3.10}
$$

For the computation using real gas approach, the density can be directly computed using the multi-parameter EoS: $\rho_2 = f\left(p_2, s_1, fluid\right)$. All these equations are then used to compute the value of M_2 and ρ_2 with increasing value of static pressure ratio from 1 until the target pressure ratio (β_{ts}).

Table 3.2: Isentropic exponent to be used in real gas analysis [19]

Exponent	Governing relationship	Formula
γ_{Pv}	Pressure-volume	$\gamma_{Pv} = -\frac{v}{P}\frac{c_p}{c_v}\left(\frac{\partial P}{\partial v}\right)_T$
γ_{Tv}	Temperature-volume	$\gamma_{Tv} = 1 + \frac{v}{c_v}\left(\frac{\partial P}{\partial T}\right)_v$
γ_{PT}	Pressure-temperature	$\gamma_{PT} = \frac{1}{1-\frac{P}{c_p}\left(\frac{\partial v}{\partial T}\right)_P}$

The result of both approaches can be seen in Figures 3.2, 3.3, 3.4 and 3.5. Some key information from the graphs are:

- Air presents a larger dilute gas region, represented by Z close to 1, compared to R134a
- Near the critical point, R134a, which has a more complex molecular structure, presents a region where the value of Γ is within the range $0 < \Gamma < 1$
- Outlet Mach number decrease and outlet density increase monotonically with an increasing compression ratio
- In the dilute gas region, both fluids thermodynamic properties can be approximated well using ideal gas law
- The deviation of thermodynamic properties values predicted by the ideal gas law to the actual values becomes more significant in fluids with more complex molecular structure, when shifting towards the dense gas region.

The larger dilute gas region seen in fluids with simpler molecular structure allows reasonable agreement between thermodynamic properties values approximated using the ideal gas law and those computed using a real gas multi-parameter EoS. Fluid with a simple molecular structure contains fewer atoms per molecules, therefore reducing the effect of intermolecular forces on the thermodynamic properties values. From these comparisons, it is clear that the real gas behaviour is influenced by both molecular complexity and the local thermodynamic state of the fluid. The thermodynamic behaviour of the fluid along the compression is determined by the inlet total thermodynamic properties and the compression ratio.

3.2. Generalized Isentropic Exponents

Referring to the generalized non-ideal similarity equation for the centrifugal compressor in Equation 2.20, the fluid thermodynamic state at the compressor inlet is included in the equation as the pressure-volume isentropic exponent (γ_{pv}). Efforts to include flow non-ideality effect using this exponent have been thoroughly investigated previously by Nederstigt [19]. The approach was based on the work of Kouremenos [20] and Baltadjiev [21], which collects all the real gas effect as equivalent isentropic exponents. Using these isentropic exponents, the ideal gas relation can be reused for real gas, for example:

$$pV^{\gamma_{pv}} = constant \tag{3.11}$$

The isentropic exponents and their description is summarized in Table 3.2. From the derivations, it is clear that the exponents are thermodynamic state variables, i.e. they change along the whole thermodynamic plane. Referring back to the isentropic compression cases in Table 3.1, the contour and value of γ_{pv} along the compression is shown in Figures 3.6 and 3.7 respectively. From the figure, it can be seen that in the dilute gas region, the value of γ_{pv} is close to the value of the ideal gas heat capacity ratio (γ), while in the dense gas region it deviates. The average value of γ_{pv} is, therefore, a good indicator of the effect of NICFD in the process, as exhibited by its usage in the generalized non-ideal similarity equation for the centrifugal compressor (Equation 2.20). Another advantage in utilizing γ_{pv} in implementing NICFD effect in the compression process is the ability to formulate relationships between thermodynamic properties explicitly. Using the exponents definition in Table 3.2, explicit analytical formulations of thermodynamic properties can then

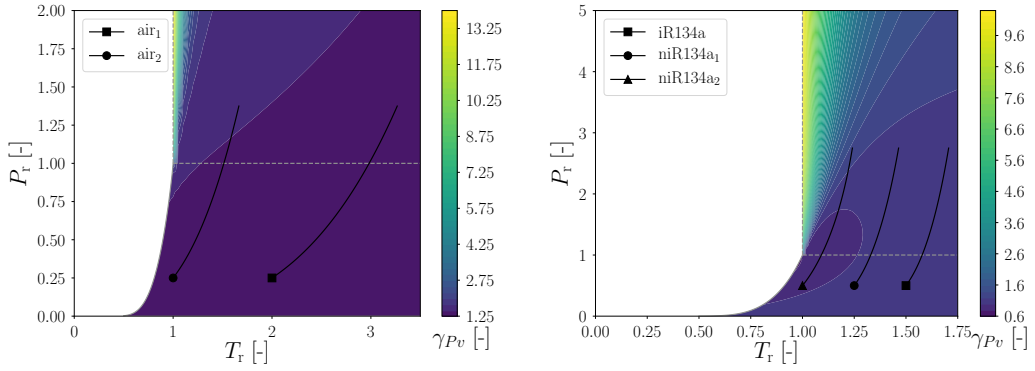

(a) (b)

Figure 3.6: γ_{pv} contour along isentropic compression in (a) Air; (b) R134a - reduced inlet properties as in Table 3.1. The isentrophe and thermodynamic parameter value is calculated using a program currently being developed at the Power and Propulsion group at Delft University of Technology

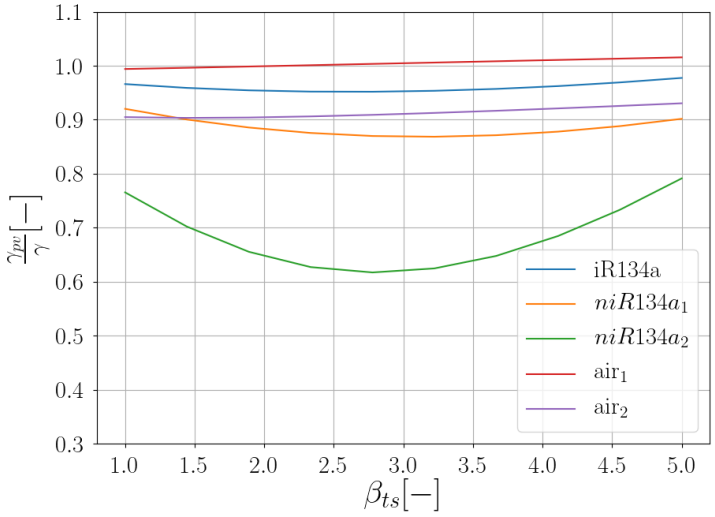

Figure 3.7: Ratio of γ_{pv} to $\gamma = \frac{c_p}{c_v}$ along the isentropic compression for cases in Table 3.1

Table 3.3: Isentropic exponent to be used in real gas analysis [19]

Descript'ion	**Formula**
Stagnation pressure ratio	$\frac{P_t}{P} = \left[1 + \frac{\gamma_{Pv}-1}{2} M^2\right]^{\frac{\gamma_{Pv}}{\gamma_{Pv}-1}}$
Stagnation temperature ratio	$\frac{T_t}{T} = \left[1 + \frac{\gamma_{Pv}-1}{2} M^2\right]^{\frac{\gamma_{Tv}-1}{\gamma_{Pv}-1}}$
Stagnation density ratio	$\frac{\rho_t}{\rho} = \left[1 + \frac{\gamma_{Pv}-1}{2} M^2\right]^{\frac{1}{\gamma_{Pv}-1}}$
Stagnation compressibility ratio	$\frac{Z_t}{Z} = \left[1 + \frac{\gamma_{Pv}-1}{2} M^2\right]^{\frac{\gamma_{Pv}-\gamma_{Tv}}{\gamma_{Pv}-1}}$
Stagnation speed of sound ratio	$\frac{a_t}{a} = \left[1 + \frac{\gamma_{Pv}-1}{2} M^2\right]^{0.5}$

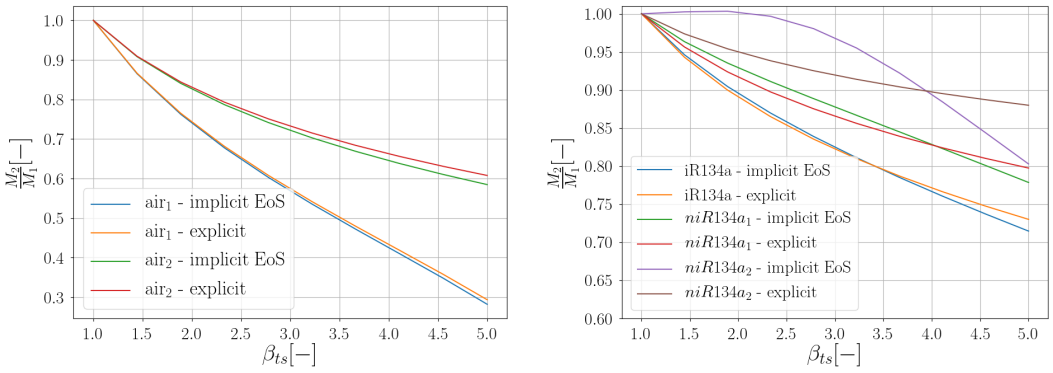

Figure 3.8: Mach number trend of (a) air and (b) R134a along isentropic compression for isentropic compression in Figure 3.2, calculated with explicit thermodynamic relations with constant γ_{pv} (label = explicit) and real gas multi-parameter equation of state (label = implicit EoS)

be further developed, for example the isentropic flow relations which take account of real gas effect, as seen in Table 3.3. Nevertheless, as the exponents are thermodynamic state variables, these explicit analytical formulations of thermodynamical properties are strictly valid when the values of the isentropic exponents are almost constant throughout the entire process. To obtain a better understanding of this limitation, the Mach number trend in Figure 3.4b is recalculated using the isentropic flow relations in Table 3.3. The pressure ratio between inlet and outlet state can be written as:

$$\frac{p_2}{p_1} = \beta = \frac{\left(1+\frac{\gamma_{pv,1}}{2}M_1^2\right)^{\frac{\gamma_{pv,1}}{\gamma_{pv,1}-1}}}{\left(1+\frac{\gamma_{pv,2}}{2}M_2^2\right)^{\frac{\gamma_{pv,2}}{\gamma_{pv,2}-1}}} \tag{3.12}$$

To obtain an explicit formulation of M_2 with respect to β and M_1, γ_{pv} must be assumed to be constant, i.e. $\gamma_{pv,1} = \gamma_{pv,2}$. With this assumption, M_2 can be formularized as:

$$M_2 = \sqrt{\frac{2}{\gamma_{pv}-1}\left(\frac{1+\frac{\gamma_{pv}}{2}M_1^2}{\beta^{\frac{\gamma_{pv}-1}{\gamma_{pv}}}}-1\right)} \tag{3.13}$$

The value of M_2 obtained from this method is plotted alongside the values computed using the multi-parameter equation of state in Figure 3.8. The values calculated using the constant γ_{pv} assumption deviate considerably in the dense gas region (case niR134a$_2$). This is expected as in Figure 3.7 there is a strong γ_{pv} gradient along the isentropic compression in this case. On the other hand, in cases without strong γ_{pv} gradient, such as in the case of total-static transformation, taking an average value of γ_{pv} is a good enough approximation; the explicit isentropic gasdynamic formulation in Table 3.3 is still valid.
This problem regarding the explicit formulation of thermodynamic properties is also relevant in preliminary centrifugal compressor design. Casey [11] found that for a given flow coefficient, there is a certain inlet angle leading to the minimum relative inlet Mach number. A lower value of the Mach number is desirable, as it decreases the inducer shock losses. Figure 3.9 shows the equivalent modified mass flow function (Φ') of a centrifugal compressor as a function of inlet relative flow Mach number (M_{w1}) and inlet relative flow angle (β_{1s}). The modified mass flow function is another form of flow coefficient and will be discussed more in Subsection 5.1. In the dilute gas region, the trend and values of the optimum inlet flow angle calculated using the explicit formulation of thermodynamic properties coincide with those calculated using a multi-parameter equation of state in thermodynamic libraries, as seen in Figure 3.9a. However, in the dense gas region, as seen in Figure 3.9b, the optimum angle locus calculated using the explicit formulation deviates greatly from that computed using an implicit equation of states. This deviation is largely due to the underlying assumption of the explicit formulation method: constant values of the isentropic exponents. Due to this reason, in developing the proposed model in the work, all thermodynamic properties are obtained employing an implicit equation of states formulation in thermodynamic libraries.

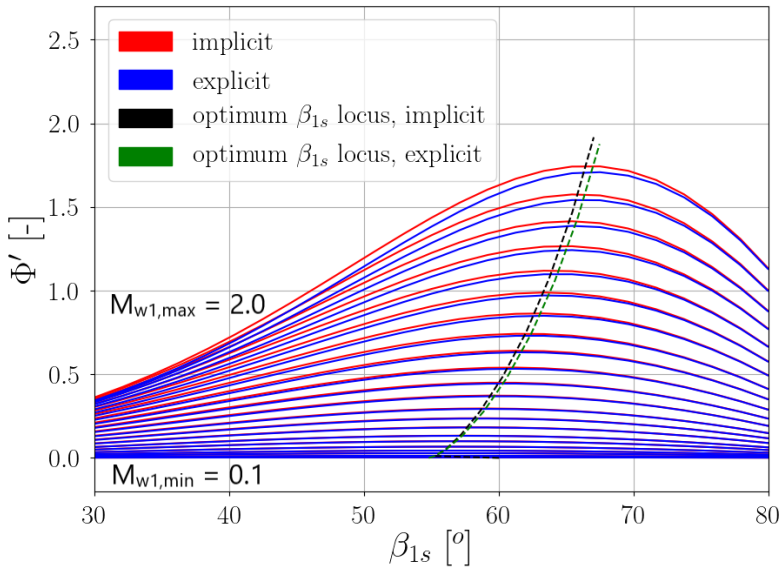

(a)

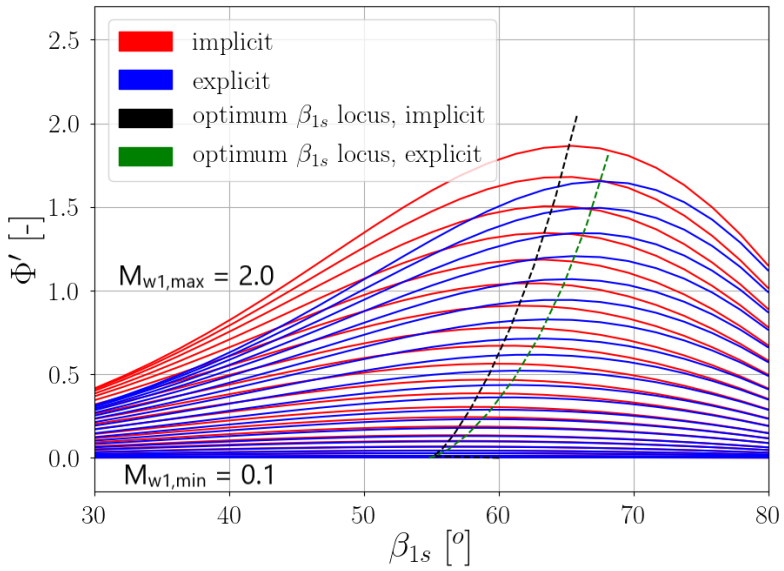

(b)

Figure 3.9: Modified mass flow function (Φ') as a function of relative inlet Mach (M_{w1}) and optimum inlet relative flow angle (β_{1s}) calculated with explicit thermodynamic relations with constant γ_{pv} (label = explicit) and real gas multi-parameter equation of state (label = implicit). Case used: (a) iR134a and (b) niR134a$_2$. M_{w1} contours from 0.1 to 2.0.

4

Loss Model

In this chapter, the loss model is introduced and described in details. The most commonly adopted semi-empirical loss correlations are introduced in the first section, alongside their assumptions and test-case results. This section also introduce the reason on the choice of developing a physics-based loss model, which is discussed in-depth in the second section, together with the underlying assumptions and the comparison with the semi-empirical counterpart.

4.1. Empirical Loss Model

In preliminary compressor design, mean-line (average) quantities of thermodynamic and fluid dynamic are used to provide an estimate of the compressor's performance. In centrifugal compressor design, the averaging takes place in the inlets and outlets of both the impeller and the diffuser. This averaging means all local flow phenomena which may happen due to losses are not accounted for in the mean-line quantities. Such a model, therefore, relies heavily on the implementation of additional loss models to accurately capture the entropy generated in the blade passage [4], [5]. In turn, the fidelity of said loss models greatly affects the accuracy of the whole preliminary design framework. This reason was the driving force behind previous development of compressor loss models as early as in the 1960s [16].
Herbert [22] devised reasonably comprehensive loss models for the IGV (Inlet Guide Vanes), impeller, vaneless space, and vaned diffuser. The caveat of this method is that tuning is necessary for each loss model to obtain agreements with a range of test cases. Another more detailed approach was developed by Jansen [23], Coppage [24], Johnston and Dean [25] and Aungier [8], among numerous others[10]. All of their methods are based on the internal-external loss generation classification. Within this classification, the internal loss mechanisms are [5]:

- Incidence: losses due to mismatch between the direction of relative velocity of fluid at inlet and the inlet blade angle at off-design conditions
- Skin friction: losses due to viscous friction inside the blade passage
- Diffusion and blade loading: losses due to boundary layer growth, separation and secondary flows
- Clearance: losses due to flow leakage from the pressure to the suction side of the impeller
- Shock wave: losses due to the formation of shock waves in impellers with supersonic inlet conditions

These internal losses were usually considered as total pressure loss ΔP_t. In conjunction with temperature change, the total pressure loss can be directly translated to total enthalpy drop (Δh_t). On the other hand, external losses consist of loss mechanisms which contribute to the increase of external work input without leading to a total pressure rise. The losses usually included in this category are [5]:

- Disk friction: total enthalpy rise due to fluid shear force between impeller's rear face and adjacent surface
- Recirculation: total enthalpy rise due to backflow from vaneless space to the impeller passage

Table 4.1: Optimum set of loss models for centrifugal compressors [10], [27]

Loss mechanism	**Loss model**
Incidence loss	$\Delta h_{t,inc} = w_1^2 \frac{\sin^2\lvert\beta_1-\beta_{1,opt}\rvert}{2}$
Blade loading loss	$\Delta h_{t,bld} = 0.05 D_f^2 U_2^2$
Skin friction loss	$\Delta h_{t,sf} = 2C_f \frac{l_b}{D_{hyd}} \bar{W}^2$ $\bar{W} = \frac{V_{1s}+V_2+W_{1s}+2W_{1h}+3W_2}{8}$
Clearance loss	$\Delta h_{t,cl} = 0.6 \frac{g}{H_2} V_{tg2} \left\{ \frac{4\pi}{H_2 Z} \left[\frac{r_{1s}^2 - r_{1h}^2}{(r_2 - r_{1s})\left(1+\frac{\rho_2}{\rho_1}\right)} \right] V_{tg2} V_{m1mid} \right\}^{0.5}$
Mixing loss	$\Delta h_{t,mix} = \frac{1}{1+\tan^2\alpha^2} \left(\frac{1-\epsilon_{wake}-b^*}{1-\epsilon_{wake}} \right)^2 \frac{V_2^2}{2}$ $b^* = \frac{H_{diffuserinlet}}{H_2}$
Shock loss	$\Delta h_{t,shock} = 0.1 \left(M_{w1}^2 - 1\right) \frac{w_1^2}{2}$
Disk friction loss	$\Delta h_{t,df} = f_{df} \frac{\bar{\rho} r_2^2 U_2^3}{4\dot{m}}$ $\bar{\rho} = \frac{\rho_1+\rho_2}{2}$ $f_{df} = \frac{2.67}{Re_{df}^{0.5}}, Re_{df} < 3x10^5$ or $f_{df} = \frac{0.0622}{Re_{df}^{0.2}}, Re_{df} \geq 3x10^5$ $Re_{df} = \frac{U_2 r_2}{\nu_2}$
Recirculation loss	$\Delta h_{t,rc} = 8x10^5 \sinh\left(2.5\alpha_2^3\right) D_f^2 U_2^2$

In addition to the previous loss sources, the trailing edge mixing loss is sometimes not included within the internal loss sources for impeller, but it is accounted for in the diffuser, as the mixing happens after leaving the impeller [25]. Oh et al. [10] performed an exhaustive comparison between existing empirical loss models for centrifugal compressor, and summarized the optimum set of loss models that present a reasonable agreement with experimental results of Eckardt impellers O, A and B [26], and KIMM impeller [10]. The summarized models can be seen in Table 4.1.

An alternative approach to loss modeling in centrifugal compressors is the so-called two zone model or jet and wake model, described, for example, by Schneider et al. [28]. The underlying concept is that in the shroud region towards impeller discharge the flow is often separated and can be theoretically split into a high momentum region, called jet, and a low momentum region, named wake [27], especially approaching the impeller discharge. A visualization of this phenomenon is presented in Figure 4.1. This approach reproduces the actual flow structure observed in most impeller geometries more closely, thus leading to more accurate loss estimation. Nevertheless, additional parameters such as wake blockage have to be introduced to account for the differences in momentum and the extension of each zone, thus increasing the overall model sensitivity to external input.

Another even simpler empirical approach has also been researched, correlating efficiency measurements on similar machines with global parameters such as specific speed, flow coefficient and clearance. Within this class, the most popular model is the one by Casey and Robinson [9]. The model is fitted for high flow capacity centrifugal compressors, taking into account modern impellers and optimized resorting to high-fidelity CFD. Due to its purely empirical nature, this type of loss model is very accurate in predicting the efficiency of new machines of similar size, designed following the same workflow. On the other hand, it's arguably not suitable

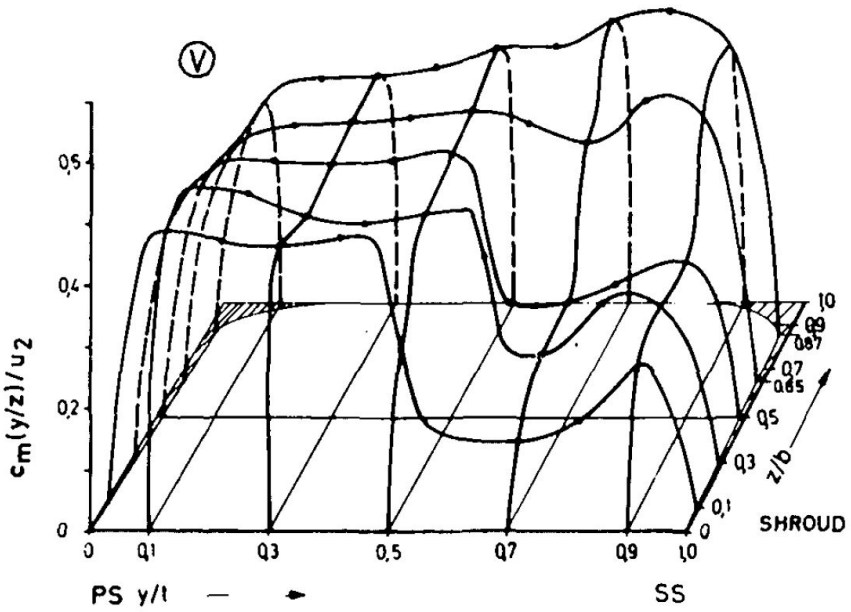

Figure 4.1: Experimental result of Eckardt O-impeller: local meridional velocity normalized by peripheral speed at impeller discharge. Flow jet-and-wake structure observed at the shroud (jet at pressure side; wake at suction side) [26]

to predict the performance of new compressors of different size and operating with different working fluids. The simple set of equations defining the model is listed in Equation 4.1, while the influence of two main design parameters, namely compression ratio and flow coefficient, on stage efficiency is presented in Figure 4.3.

$$\begin{aligned}
&\phi_{t1} < 0.08, \eta'_p = 0.86\left[1 - 27\left(0.08 - \phi_{t1}\right)^2 - 5000\left(0.08 - \phi_{t1}\right)^4\right] \\
&\phi_{t1} \geq 0.08, \eta'_p = 0.86\left[1 - 10\left(0.08 - \phi_{t1}\right)^2\right] \\
&M_{u2} \leq 0.8, \eta_p = \eta'_p \\
&M_{u2} > 0.8, \eta_p = \eta'_p - 0.05\phi_{t1}\left(M_{u2} - 0.8\right) - 3\phi_{t1}^2\left(M_{u2} - 0.8\right)^2
\end{aligned} \tag{4.1}$$

Within this model, the stage efficiency is correlated to the global parameters, namely work and flow coefficients (ψ and ϕ_{t1}), total-to-total pressure coefficient (β_{tt}), geometrical parameter (the shape parameter $k = 1 - \frac{r_{1h}}{r_{1s}}^2$, and the diameter ratio $\frac{D_{1s}}{D_2}$), tip Mach number (M_{u2}) and inlet relative Mach number(M_{w1}). In comparison to this highly empirical method, implementing the loss models lister on Table 4.1 also exhibits a similar trend, as seen in Figure 4.3.

As exhibited by models in the work of Oh et al., the losses were accounted as the decrease in enthalpy [10], which is based on the early works of Balje [29]. Referring to Figure 4.4, the enthalpy loss coefficient in a compressor blade is defined as:

$$\zeta = \frac{h_2 - h_{2s}}{h_{t1} - h_1} \tag{4.2}$$

This loss accounting method and coefficient is perfect for cascade tests. However, relative stagnation enthalpy can change as a result of changes in radius without any actual efficiency drop. Along a rotor blade span, for example, from the conservation of rothalpy,

$$Rothalpy = h + \frac{w^2}{2} - \frac{u^2}{2} = h_{t,relative} - \frac{u^2}{2} \tag{4.3}$$

an increase of radius increases the relative stagnation enthalpy. The consequence of this decision in the choice of loss accumulation variable is a deterioration in prediction accuracy as rotational Mach number (or pressure ratio) increases [8]. This problem highlights the need for a more general loss accounting parameter and models.

Looking back, the basic definition of isentropic efficiency is the ratio of actual work to isentropic work (for

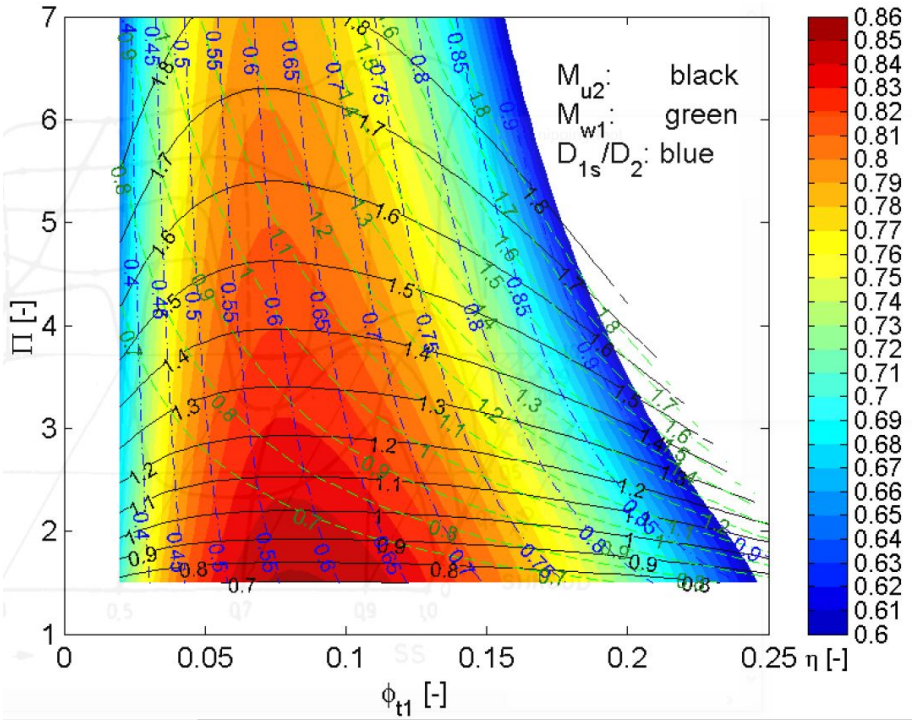

Figure 4.2: Centrifugal compressor efficiency as a function of total pressure ratio ($\Pi = \beta_{tt}$) and flow coefficient (ϕ_{t1}) [11]. Air as working fluid ($\gamma = 1.4$), and is considered as perfect gas. The work coefficient (ψ) is fixed at $\mu = 0.75$. The shape factor (k) is fixed at 0.9

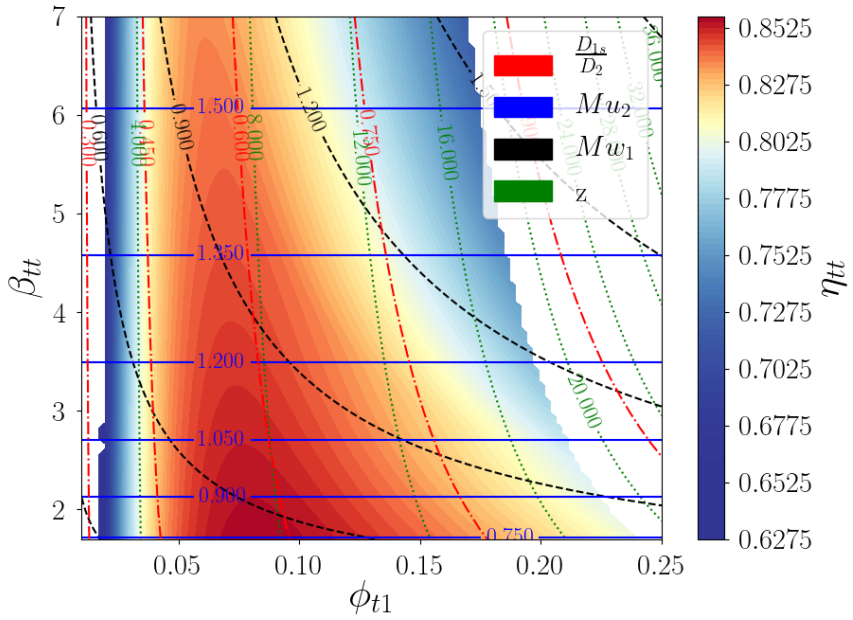

Figure 4.3: Centrifugal compressor efficiency as a function of total pressure ratio, losses model used as in Table 4.1. All other parameters similar to 4.2

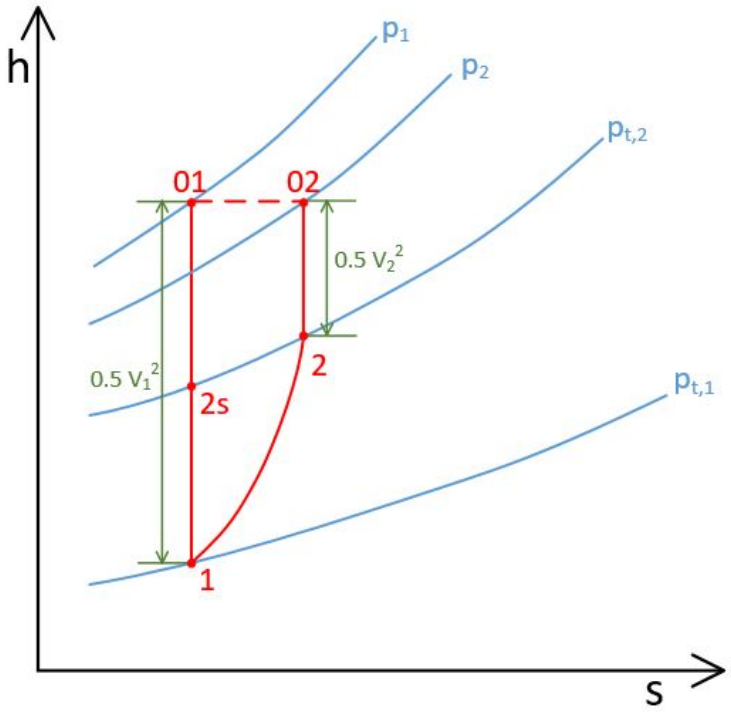

Figure 4.4: Enthalpy-entropy diagram for a compression process

turbine) and vice-versa (for the compressor). The factor differentiating the two works are irreversibility factors, which in turn is accounted as entropy generation. Entropy generation may also be caused by heat transfer to a system. However, In a turbomachine the process is largely adiabatic, so it can be assumed that the entropy generation translates directly to loss generation [30]. Other reasons to base loss models from entropy generation are:

- Entropy value, unlike enthalpy, does not depends on the reference system (rotating or stationary)
- In the limit case of adiabatic machines without heat transfer, entropy can only increase or be constant. Hence, summing the calculated entropy of each blade row yields an estimated efficiency of the whole machine.

These reasons, moreover, are not the main rationale on why novel loss models are required in developing new meanline design framework for centrifugal compressors. The main drawbacks of empirical loss models are namely:

- Good accuracy only when tuned on specific application (e.g. existing machines data from specific manufacturer); the mismatch when used to predict the performance of the new design may be significant. This is due to new features in the machine that were not included in the model when they were calibrated [30]. Within the scope of the present work, for example, using the semi-empirical loss models diminishes the effect of the working fluid on the machine performance.
- A good physical understanding of the flow, and particularly of the origins of loss, is more important than the availability of a good but oversimplified loss correlation [30].

4.2. Physics-Based Loss Model

The classification of loss mechanisms in centrifugal compressor into profile, endwall and leakage losses is adopted, as depicted in Figure 4.5. Although each of these loss mechanisms is rarely independent of each other, such classification is still widely adopted to enable further insight into the major physical phenomena resulting in the entropy generation. The three components are comparable in magnitude, each accounting for about 1/3 of the total loss [30]. The derivation of the conceptual models as well as their physical interpretation are discussed in depth in the following paragraphs.

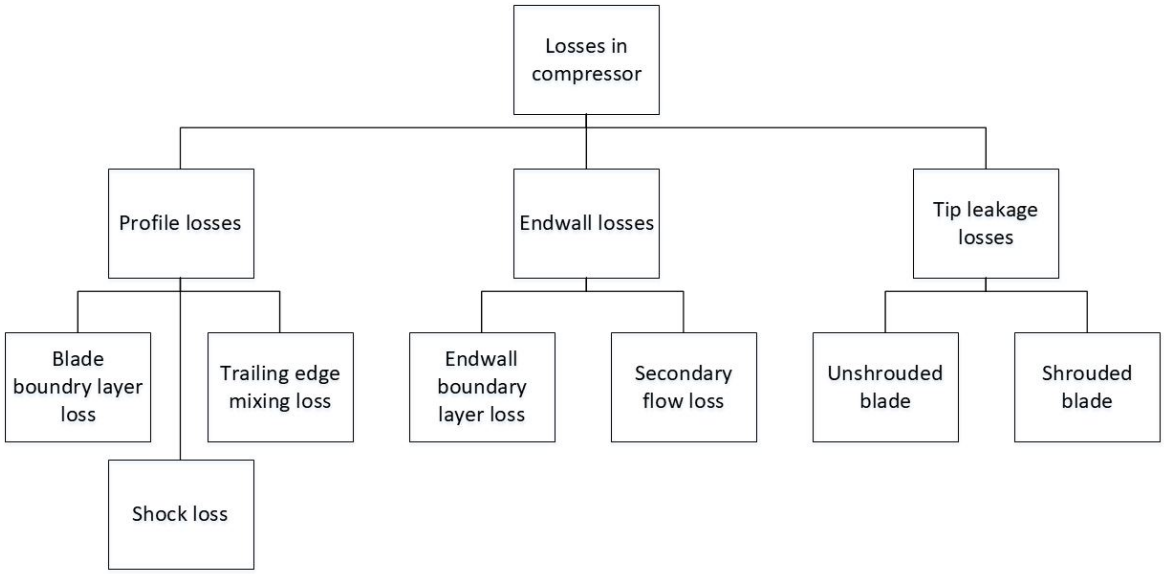

Figure 4.5: Loss mechanisms breakdown for centtrifugal compressor

4.2.1. Blade Boundary Layer Loss

The viscous dissipation occurring in the blade boundary layer is predicted resorting to the classic two-dimensional boundary layer theory. Referring to Figure 4.6, applying the second law of thermodynamics alongside the indicated thin stream tube, aligned with the x-direction:

$$T\frac{ds}{dx} = \frac{dh}{dx} - \frac{1}{\rho}\frac{dP}{dx} = \frac{dh_t}{dx} - V_x\frac{dV_x}{dx} - \frac{1}{\rho}\frac{dP}{dx} \tag{4.4}$$

Additionally, from a simple momentum balance in the x-direction,

$$F_x - \frac{1}{\rho}\frac{dP}{dx} = V_x\frac{dV_x}{dx} \tag{4.5}$$

Thus, by combining Equations 4.4 and 4.5, Equation 4.4 can be rewritten as,

$$T\frac{ds}{dx} = \frac{dh_t}{dx} - F_x \tag{4.6}$$

The resulting expression shows that in an adiabatic system, where h_t is constant, the creation of entropy is due to the friction force acting along the streamline opposite the flow direction. Next, the energy equation of a unit of mass moving through the streamtube from a Lagrangian point of view can be written as:

$$\frac{D}{Dt}\left(e + \frac{1}{2}V^2\right) = -P\frac{D}{Dt}\left(\frac{1}{\rho}\right) + V_x\left(F_x - \frac{1}{\rho}\frac{\partial P}{\partial x}\right) + \frac{1}{\rho}\left(\tau_{yx}\frac{\partial V_x}{\partial y} + \tau_{yz}\frac{\partial V_z}{\partial y}\right) - \frac{1}{\rho}\frac{\partial q}{\partial y} \tag{4.7}$$

Assuming steady flow, where $\frac{D}{Dt} = V_x\frac{\partial}{\partial x}$, Equation 4.7 can be rewritten as,

$$V_x\frac{\partial h_t}{\partial x} = F_xV_x + \frac{1}{\rho}\left(\tau_{yx}\frac{\partial V_x}{\partial y} + \tau_{yz}\frac{\partial V_z}{\partial y}\right) - \frac{1}{\rho}\frac{\partial q}{\partial y} \tag{4.8}$$

Combining Equations 4.6 and 4.8 to eliminate h_t:

$$V_xT\frac{\partial s}{\partial x} = \frac{1}{\rho}\left(\tau_{yx}\frac{\partial V_x}{\partial y} + \tau_{yz}\frac{\partial V_z}{\partial y}\right) - \frac{1}{\rho}\frac{\partial q}{\partial y} \tag{4.9}$$

Considering unit depth in the z-direction, and applying conservation of mass ρV_xA, where $A = dy$:

$$\frac{\partial}{\partial x}\left(\rho V_xs\right)dy = \frac{1}{T}\left(\tau_{yx}dV_x + \tau_{yz}dVz\right) - dq \tag{4.10}$$

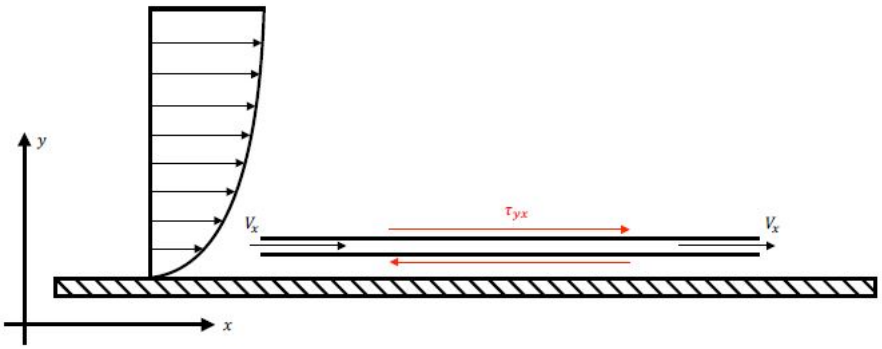

Figure 4.6: Stream tube near a boundary layer

Integrating through the boundary layer thickness δ gives:

$$\int_0^{\delta} \left[\frac{\partial}{\partial x} \left(\rho V_x s \right) dy \right] = \int_0^{\delta} \left[\frac{1}{T} \left(\tau_{yx} dV_x + \tau_{yz} dVz \right) - dq \right] \tag{4.11}$$

For a two-dimensional boundary layer, τ_{yz} is zero (no skew in the z-direction), and considering adiabatic condition ($q = 0$) at both wall surface and boundary layer edge, Equation 4.11 can be simplified to:

$$\int_0^{\delta} \frac{\partial}{\partial x} \left[\rho V_x \left(s - s_{\delta} \right) \right] dy = \int_0^{\delta} \frac{1}{T} \tau dV \tag{4.12}$$

which gives the rate of total entropy creation per unit surface area due to boundary layer dissipation. Following this derivation, equation 4.12 is generally valid for any working fluid and for any boundary layer state.
As suggested by Denton [30], it is more convenient to rearrange Equation 4.12 and express the entropy generation within the boundary layer as function of the dimensionless dissipation coefficient C_d, defined as:

$$C_d = \frac{T_e \dot{S}_a}{\rho_e V_e^3} \tag{4.13}$$

The key features of C_d are:

- For turbulent boundary layers the dissipation coefficient is weakly dependent on the boundary layer parameters as compared to the skin friction coefficient
- Dissipation coefficient is affected by the external pressure gradient. In particular, a diffusing boundary layer, i.e. the one observed in a compressor row, is associated with higher values of Cd.
- In centrifugal compressors, the value of C_d is larger than is usual in two-dimensional boundary layers because of the highly three-dimensional flow.
- For many turbomachinery applications where Re_{θ} is in the order of 1000, C_d can be taken as 0.002 (Figure 4.7).

Returning to Equation 4.12, rearranging with Equation 4.13, and integrating towards the x-direction yields:

$$\dot{S} = \int_0^{x} \frac{\rho_e V_e^3 C_d}{T_e} dx \tag{4.14}$$

This equation is used to compute the entropy generated in the boundary layer up to location x, hence, at the trailing edge, the corresponding entropy production refers to the whole entropy generation on one blade surface.
The unknowns from Equation 4.14 can be grouped into two categories, C_d and the flow quantities at the boundary layer edge (ρ_e, V_e and T_e). However, the value of C_d is generally unknown at preliminary design phase. Due to the lack of data for the value of C_d for turbomachineries operating with non-ideal flows, in the remainder of this work a conservative approach (based on Figure 4.7) by fixing C_d = 0.002 is adopted.

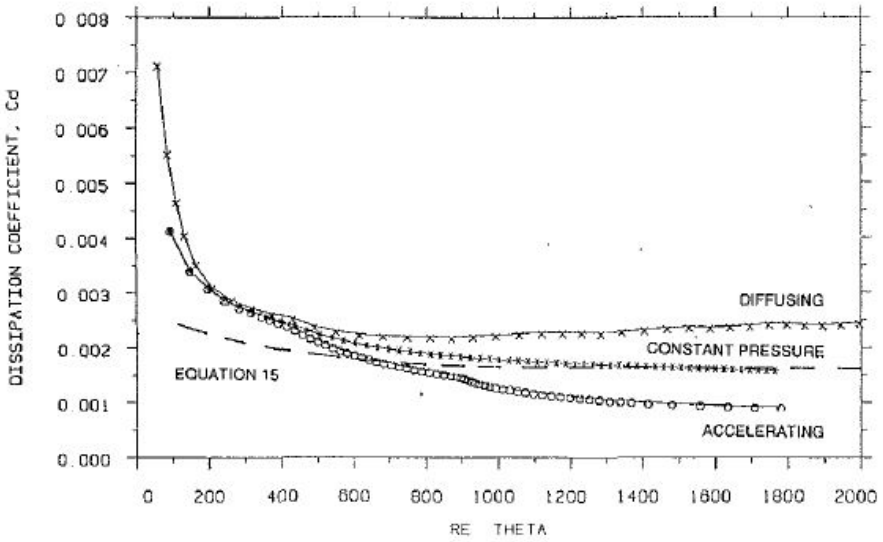

Figure 4.7: Dissipation constant values for turbulent flow [30]

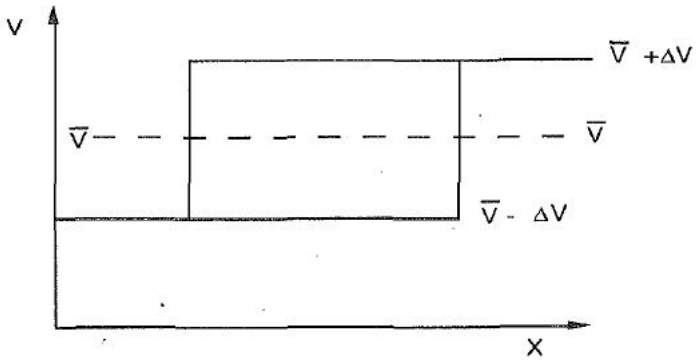

Figure 4.8: Rectangular blade surface velocity distribution [30]

On the other hand, an additional model is also needed to estimate the value of the flow quantities variation at the boundary layer edge along the blade pressure and suction surfaces. For axial turbine stages, the simplest model to be adopted is to assume rectangular distribution of the relative velocity at the boundary layer edge along the blade pressure and suction surfaces, as seen in Figure 4.8. This is performed in the work of Denton [30], and the framework is explained in depth in the work of Giuffre' [7]. Referring to the Figure 4.9, the two unknowns for the model are ΔV and $\bar{V}$ - the former corresponds to the difference between the average relative velocity and the surface relative velocity, while the latter is the average relative velocity. In case of an axial blade row, the circulation theorem can be solved for ΔV by assuming zero blade thickness, as shown in Figure 4.9, control volume 1:

$$\Gamma_1 = \oint \vec{V} ds = \left(V_{ss} - V_{ps}\right) c_s = 2\Delta V c_s \tag{4.15}$$

On the other hand, the circulation for control volume 2 can be written as:

$$\Gamma_2 = \oint \vec{V} ds = \Delta V_t ds \tag{4.16}$$

where V_t is the tangential component of the velocity. Because circulation does not depend on the choice of control volume ($\Gamma_1 = \Gamma_2$), equating Equations 4.15 and 4.16 leads to:

$$\Delta V = \frac{2\Delta V_t ds}{c_s} \tag{4.17}$$

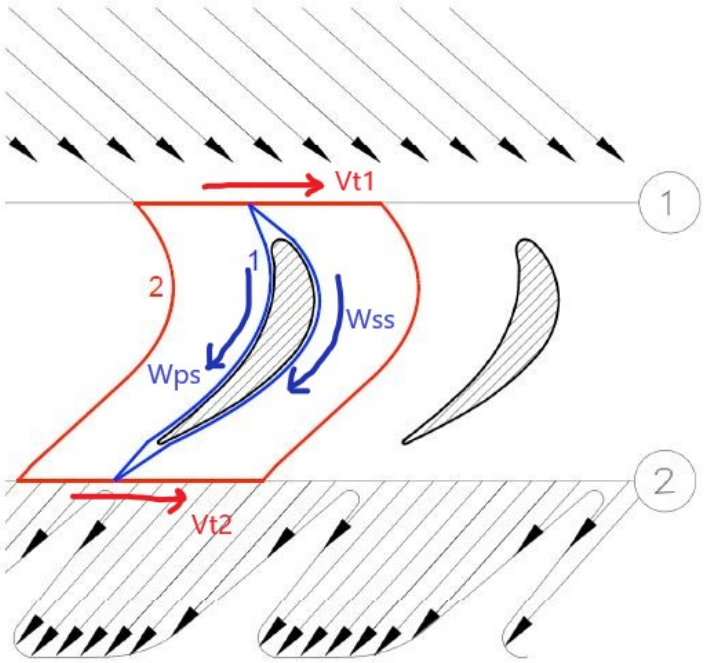

Figure 4.9: Control volume used to define the circulation theorem [7]

The second unknown, $\bar{V}$ can be easily calculated using tangential momentum balance around the blade (1st control volume), assuming steady flow and neglecting viscous effect:

$$\bar{\rho}\bar{V_m}s\Delta V_t = \left(p_{ps} - p_{ss}\right)c_{ax} \tag{4.18}$$

where s is the blade pitch. Because the suction and pressure side pressure distributions are a function of ΔV, an iterative loop is needed to solve the two equations (Equations 4.17 and 4.18) simultaneously. The iterative routine proposed by Giuffre' [7] reads:

1. Assume a first guess $\bar{V}$ value, i.e. $\bar{V} = \frac{V_{inlet}+V_{outlet}}{2}$
2. Compute V_{ps} and V_{ss}
3. Using total relative enthalpy definition, compute the static pressure and suction side enthalpy distribution
4. Compute the local static pressure using the equation of state. This is the step where flow non-ideality and molecular complexity are accounted for
5. Compute the residual of the tangential momentum balance (calculate the error between RHS and LHS terms of Equation 4.18)
6. Change $\bar{V}$ value and iterate until convergence

This simplified approach is valid for axial turbomachinery, since constant peripheral speed on each blade-to-blade section cause the last term in the definition of rothalpy:

$$Rothalpy = h_1 + \frac{w_1^2}{2} - \frac{u_1^2}{2} = h_1 + \frac{w_2^2}{2} - \frac{u_2^2}{2} \tag{4.19}$$

to drop and leading to the conservation of total relative enthalpy, $h_{t,rel} = h_1 + \frac{w_1^2}{2}$. Moreover, the assumption of a simplified rectangular velocity distribution is not valid for centrifugal compressors. Based on the works by Van den Braembussche [27], as a consequence of the increasing inter-blade distance (blade passage width) with radius and the attenuation of the Coriolis force due to backward curvature, the suction to pressure surface loading (relative velocity difference) increases from the inlet section until close to the trailing

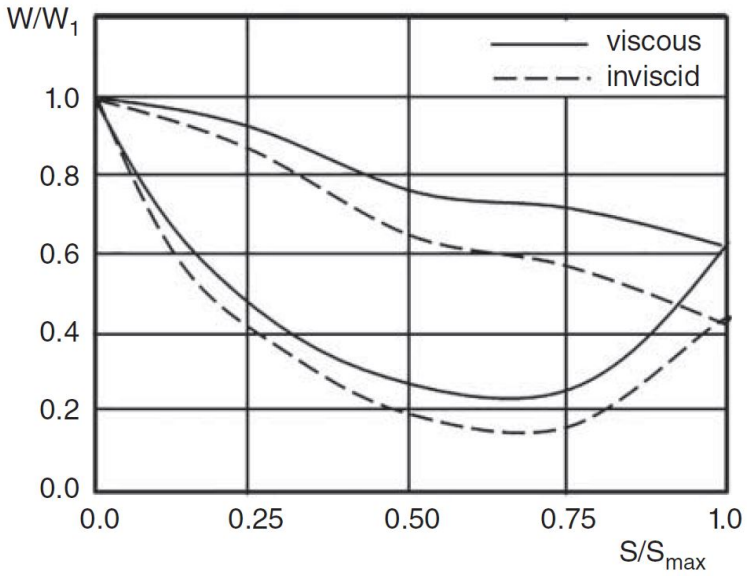

Figure 4.10: Blade surface velocity distribution at midspan of a centrifugal compressor impeller [27]

edge, where it then has to adhere to Kutta condition and becomes zero [27], as seen in Figure 4.10. As a result, a more realistic surface velocity distribution for a centrifugal compressor blade midspan is shown in Figure 4.10.

Various previous works by Wu [31], NASA [32], Van den Braembussche [27] and others have extensively described the method to estimate the blade surface velocity distribution for a centrifugal compressor. They all based their approach on the quasi 3D model for unseparated flows, more famously known as the S1 S2 model, which split the 3D flow into two 2D flow, one in the meridional and one in the blade-to-blade plane (see Figure 4.11) [32]. This framework requires spatial discretization of the blade passage in both the meridional and blade-to-blade direction. The meridional plane discretization and analysis give the average velocity distribution $\bar{V}$ and the blade-to-blade plane iteration yields the surface velocity distributions. The flowchart of this algorithm is reported in Figure 4.12.

In the present work a simplified version of the S1 S2 algorithm is implemented, by skipping the discretization along the spanwise direction and focusing only on the blade-to-blade calculation at midspan. The equation of motion for fluid in the relative frame reads [27]:

$$\bar{w} \times (\nabla \times \bar{w}) + 2\bar{\Omega} \times \bar{w} = \frac{\nabla P}{\rho} - \Omega^2 \bar{R} + \frac{\nabla w^2}{2} - \bar{f_{fr}} + \nabla g z \tag{4.20}$$

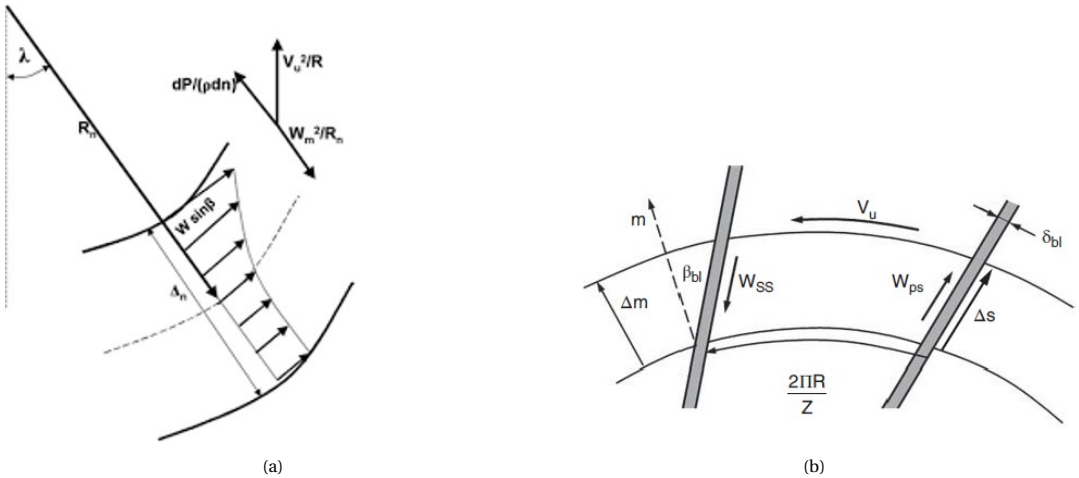

(a) (b)

Figure 4.11: Flow in (a) meridional and (b) blade-to-blade plane in centrifugal compressor [27]

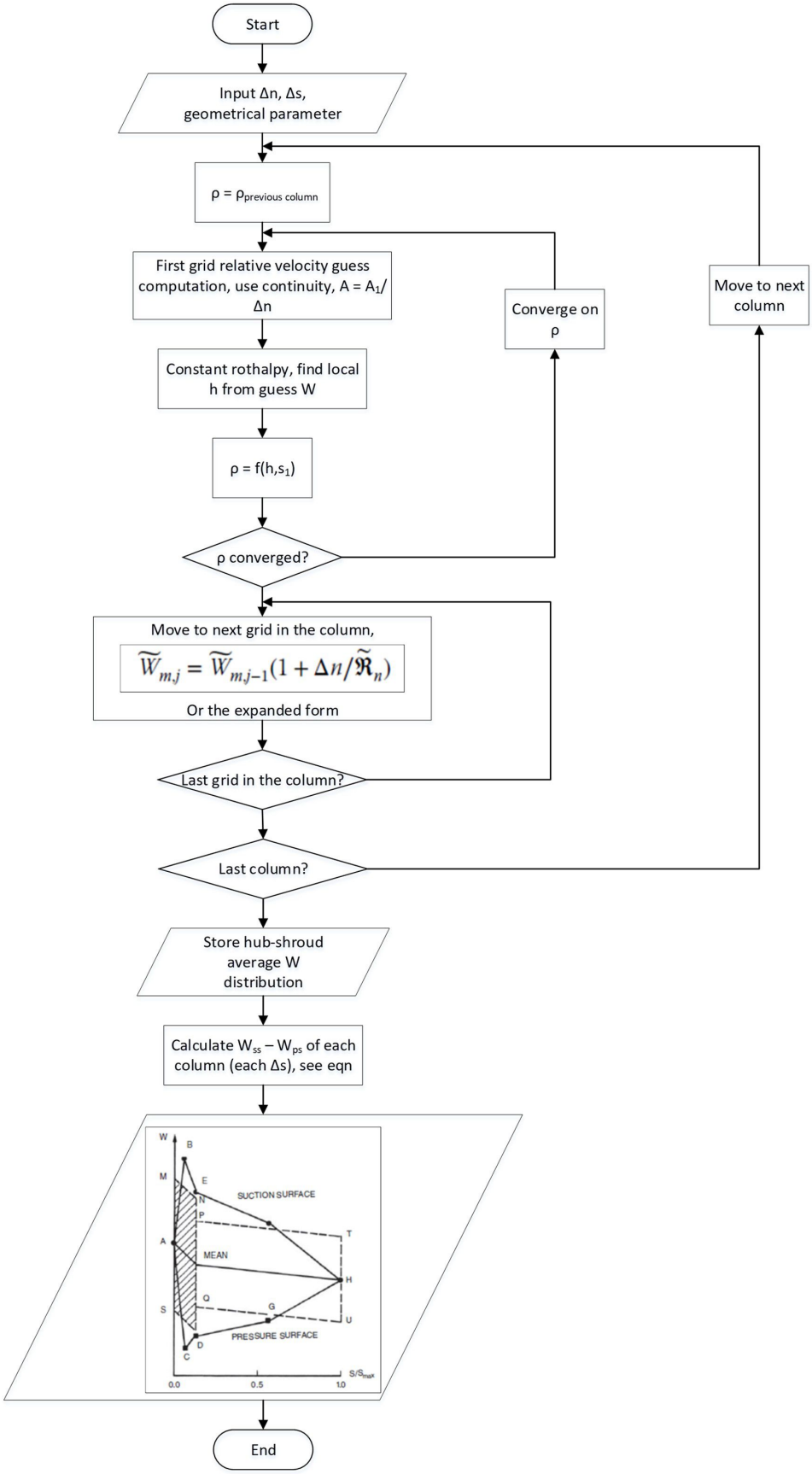

Figure 4.12: Flowchart of S1 S2 method to calculate velocity distribution

This equation of motion is similar to that in non-rotating systems, which is the momentum equation with steady flow assumption ($\frac{\partial V}{\partial t} = 0$), albeit with additional acceleration terms due to:

- Centrifugal force $\Omega^2 \bar{R}$
- Coriolis force $2\bar{\Omega} \times \bar{w}$

The energy equation for relative flow is then obtained by integrating the scalar product of the equation of motion with an infinitesimal displacement along a streamline. The integral of the Coriolis acceleration is always zero as the force is perpendicular to the displacement. Combining the definition of rothalpy (Equation 4.19) and the second law of thermodynamics (Equation 4.4), the resulting equation of motion reduces to:

$$\bar{w} \times \left(\nabla \times \bar{w} + 2\bar{\Omega}\right) = 0 \tag{4.21}$$

which has two solution: a trivial solution, $\bar{V} = 0$ and $\bar{V}$ parallel to $\nabla \times \bar{V} + 2\Omega$ or

$$\nabla \times \bar{w} = -2\bar{\Omega} \tag{4.22}$$

This equation have to be satisfied in every points of the flow field (the surface integral must be zero). According to Stoke's theorem:

$$\iint \left(\nabla \times \bar{w} + 2\bar{\Omega}\right) d\bar{s} = \oint \bar{w} \dot{d}\bar{s} + \iint 2\bar{\Omega} d\bar{s} = 0 \tag{4.23}$$

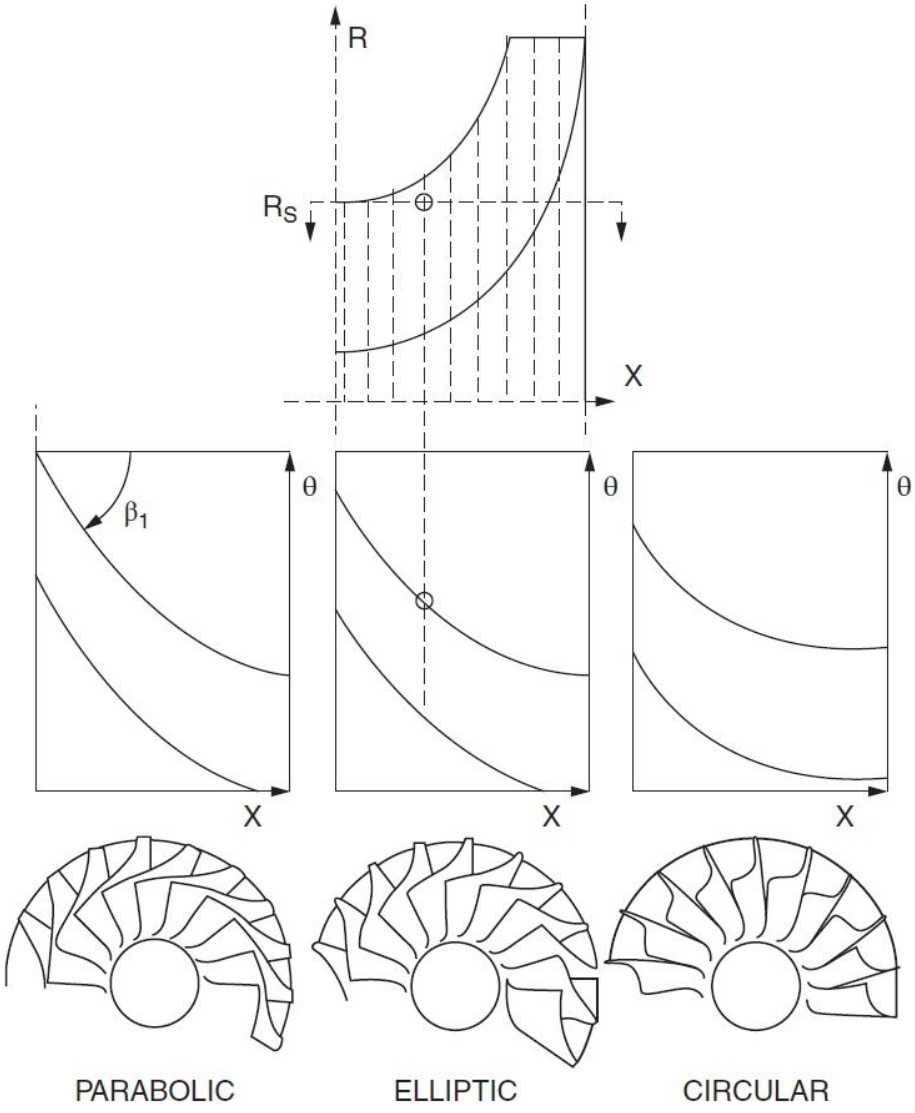

Figure 4.13: Definition of parabolic, elliptic, and circular inducer blades [33]

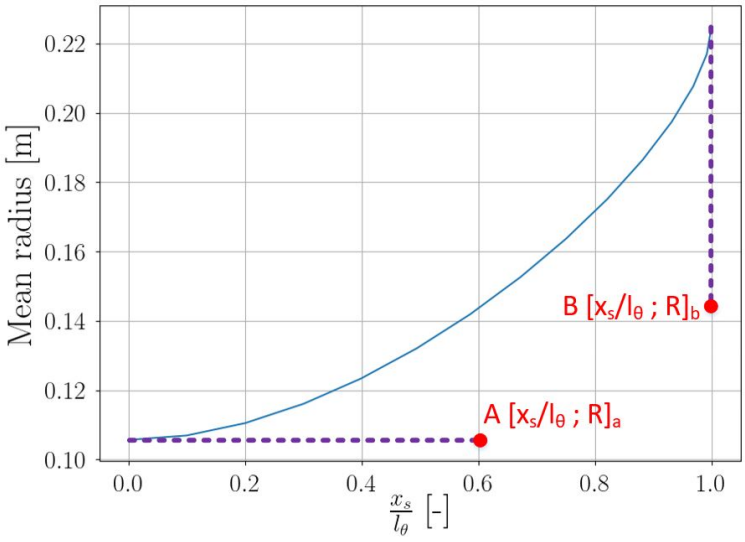

Figure 4.14: Bezier curve for radius distribution in Equation 4.24

Expanding, the difference between pressure and suction surface velocity can be explicitly written as:

$$w_{ss} - w_{ps} = \left(\frac{2\pi}{Z} - \frac{\delta_{bl}}{R\cos\beta}\right)\frac{d}{ds}\left(\Omega^2 R - w_m R\tan\beta_{fl}\right) \tag{4.24}$$

The last term in the equation proves the attenuation of the Coriolis force due to backward curvature.

In order to solve the previous equation, however, two geometrical parameters should be known, namely the blade angle (β) and radius (R) distribution. For what regards the former, Van den Braembussche [27] suggested three types of impeller blade shapes: parabolic, elliptic and circular, as seen on Figure 4.13. Once the blade metal angle distribution is fixed, the meridional flow velocity can be expressed as:

$$w_m = w\cos\beta \tag{4.25}$$

On the other hand, the impeller radius distribution along the main streamline can be expressed as a 3rd order Bezier curve, as shown in Figure 4.14.

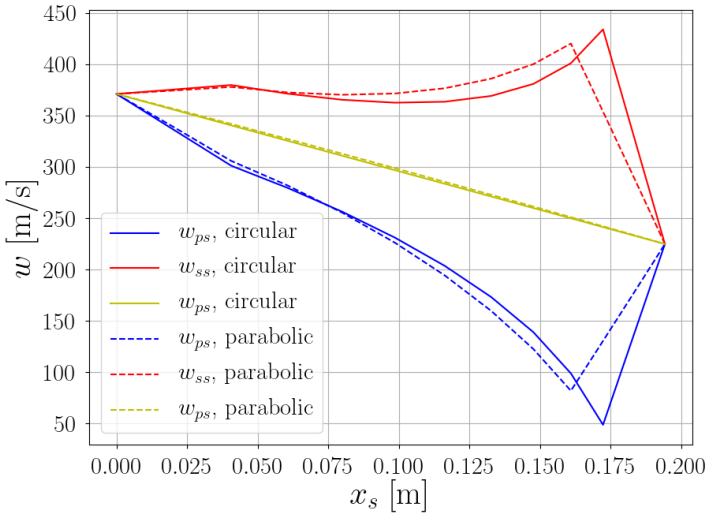

Figure 4.15: Velocity distribution in a radial impeller with parabolic and elliptic blades, using simplified S1 S2 method. fluid = air, ψ = 0.75, k = 0.9, ϕ_{t1} = 0.15, β_{tt} = 2

Once the surface velocity and mean radius distributions are known, $\Delta w_{ss,ps}$ can be calculated by solving Equation 4.24. The flow near the trailing edge is influenced by slip, which in turn influences the blade loading around the trailing edge. To estimate the location where the blade loading starts to decrease, the correlation developed by Stanitz and Prian [32] could be used. This correlation estimates the radial position R^* where the flow starts to deviate from the blade because of slip:

$$ln\frac{R^*}{R_2} = 0.71\frac{2\pi\cos\beta_{2,blade}}{Z} \tag{4.26}$$

To satisfy the Kutta condition, a linear relative velocity distribution along the blade surface is fixed, starting from the deviation point until the blade trailing edge. The resulting relative velocity distribution can be seen in Figure 4.15.
The tangential momentum balance is then analyzed. Based on the control volume shown on Figure 4.16, the tangential momentum balance can be written as:

$$\frac{\dot{m}}{Z}\left(R_2 v_{tg2} - R_1 v_{tg1}\right) = \int_0^{l_\theta}\left(p_{ps} - p_{ss}\right) HRds \tag{4.27}$$

In the same fashion of the method proposed for axial turbines, Equations 4.24 - 4.27 should be solved iteratively by changing the position of the two Bezier control points (Figure 4.14 points a and b). The complete iterative routine (flowchart is shown in Figure 4.17) reads:

1. Determine distribution of w_{mean}. The value of w_1 and w_2 is obtained from the meanline framework. It is assumed the mean relative velocity value varies linearly between the the value of w_1 and w_2.
2. Assume a β distribution (circular, parabolic or elliptical), calculate $\bar{w}_m$
3. Assume Bezier 3rd order curve for radius distribution. Guess initial location of control points (a) and (b) ($\frac{x_s}{l_\theta}\Big|_a$ and R_b, see Figure 4.14)
4. Calculate derivatives of $\tan\beta$ and radius with respect to x_s
5. Calculate Δw from Equation 4.24
6. Calculate w_{ss} and w_{ps} distribution by solving:

$$w_{mean} = \frac{w_{ss} + w_{ps}}{2} \tag{4.28}$$

7. Adjust w_{ss} and w_{ps} distribution near the trailing edge to satisfy Kutta condition (Equation 4.26)

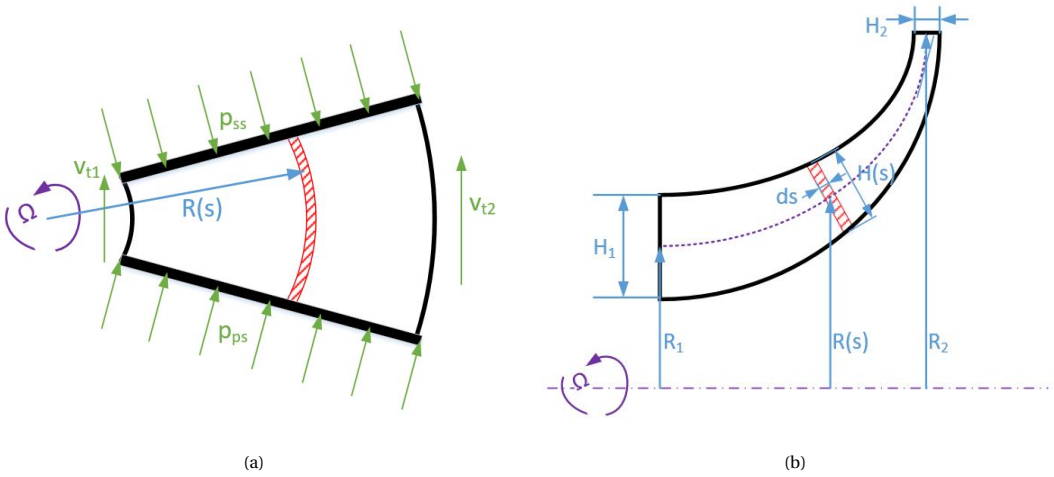

(a) (b)

Figure 4.16: Control volume for tangential momentum balance in Equation 4.18; (a) blade-to-blade view, (b) meridional view

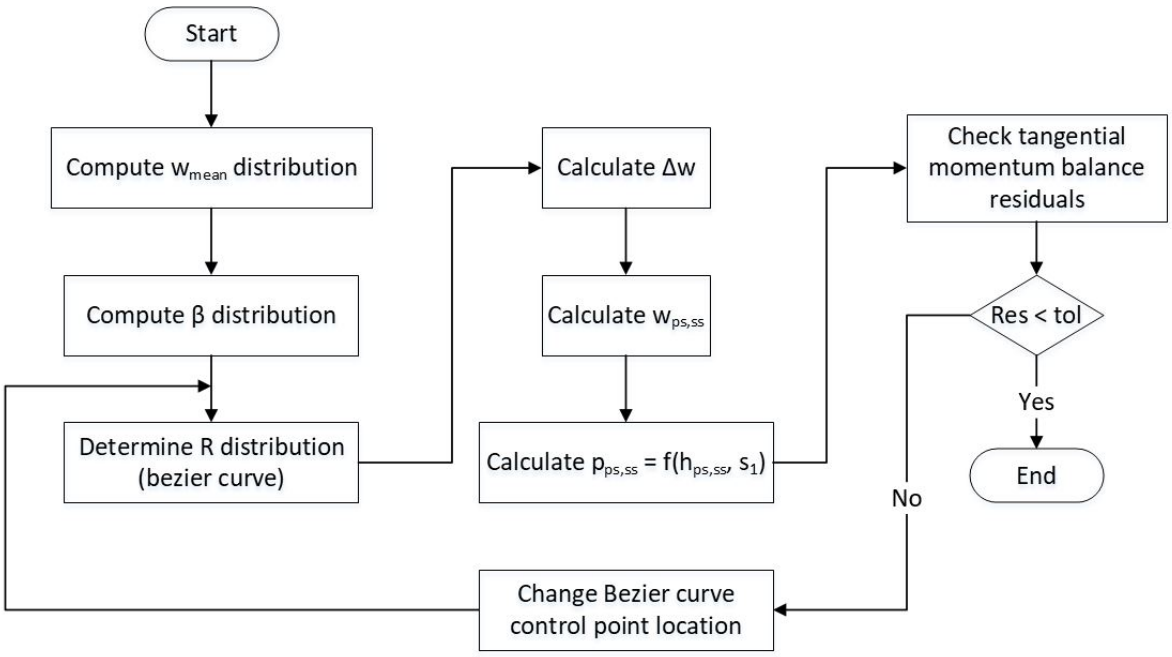

Figure 4.17: Flowchart of simplified S1 S2 method to calculate velocity distribution

8. Find p_{ss} and p_{ps} distribution from rothalpy definition (Equation 4.19 and thermodynamic equation of state ($p_{ss,ps} = f(h_{ss,ps}, s_1)$)

9. Calculate blade height distribution (H):

$$H = \frac{\dot{m}}{\left(\rho_{ps} + \rho_{ss}\right) w_m \pi R_{mean}} \tag{4.29}$$

10. Calculate the error between RHS and LHS terms of the tangential momentum balance (Equation 4.27)

11. Modify guess Bezier parameters and optimize until momentum balance error reach below threshold (<1%)

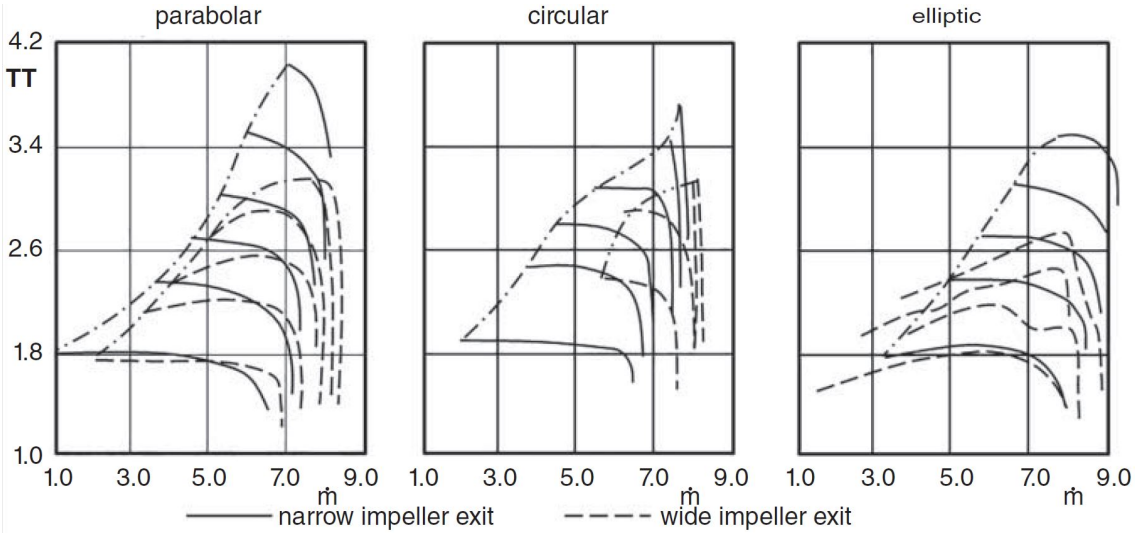

Figure 4.18: Influence of compressor geometry on operating range [33]

Table 4.2: Efficiency and entropy generation comparison for Figure4.15

Parameter	Parabolic	Circular
η_{tt}	98.53%	98.49%
Δs	2.981 J/(kg K)	3.074 J/(kg K)

For what regards the choice of the blade metal angle distribution or, in other words, the shape of the impeller blade in the blade-to-blade plane, relevant considerations can be cited from the work the work of Kramer et al. [33] (Figure 4.18) and Bhinder and Ingham [34]:

- Cases with parabolic blade shape attain the highest efficiency and pressure ratio.
- Cases with elliptical blade shape causes the largest choking mass flow.
- The circular blade has a larger throat section but the choking mass flow is smaller than with the parabolic blade due to its larger curvature.
- The large curvature of circular blades caused a higher suction to pressure side velocity gradient.
- Impeller with circular blades have the highest performance in cases with low Mach number, whereas those with parabolic blades are more efficient in case of higher Mach number

Parabolic blade seems to be the most suitable choice for impeller blades of high speed centrifugal compressors with large inlet Mach number. Nevertheless, when comparing the results obtained with the previous method for both circular and parabolic impeller blades, it is found that the influence of blade shape on boundary layer loss is negligible (see Figure 4.15 and Table 4.2).In turn, either choices are suitable for the analysis described in the following chapters.
Although more complex than the rectangular velocity distribution method, the elimination of spatial discretization in the spanwise direction yields a 1D method instead of a 2D method, which greatly reduces computational effort. Yet, the proposed method can still capture the main characteristics of the impeller surface relative velocity distribution.

4.2.2. Tip Leakage Loss

Clearance gap always exists between the stationary and rotating parts of turbomachines. Pressure differences within the gap generate flows that can be classified as:

- Leakage flows over rotor tip and stator root in unshrouded blades
- Leakage flow over tip seals of shrouded blades
- Windage flow over impeller disk; pressure difference in the gap between the rear face of the impeller and the impeller casing causes the flow in the main passage to leak towards the gap

In centrifugal compressors, the presence of leakage flows reduces the effective mass flow through the main passage and the pressure rise (Aungier [8]). Additionally, the mixing of the leakage flow with the main flow during re-entry leads to entropy generation [30]. The major component of leakage flow is the flow occuring over the shrouded/unshrouded blade tip, due to the presence of strong pressure gradient. However, as the geometry of shrouded and unshrouded impellers is different, the entropy generation mechanisms are also slightly different. Both shrouded and unshrouded impellers are widely used in industry, but shrouded impellers suffer from high-stress requirements and problems of machining and precision casting (Harada [35]), and thus, are less suitable for high-speed applications. In turn, the discussion in this work is limited only to unshrouded impellers. The mechanism of tip leakage flow formation, development and re-entry into the main flow passage is shown in Figure 4.19. The main driving force for the leakage flow is the pressure difference between the pressure and suction side of the blade. The flow entering the tip gap from the pressure side separates from the blade tip and contracts to a jet. The flow up to the throat of the jet is almost isentropic and is non-sensitive to the chordwise velocity component [30]. Due to the relatively thin compressor blades, the leakage jet is unlikely to reattach to the blade tip within the gap. The absence of jet flow reattachment in the tip gap means that there is also no pressure recovery in the tip gap, which lower the discharge coefficient in comparison to that of a turbine [36].

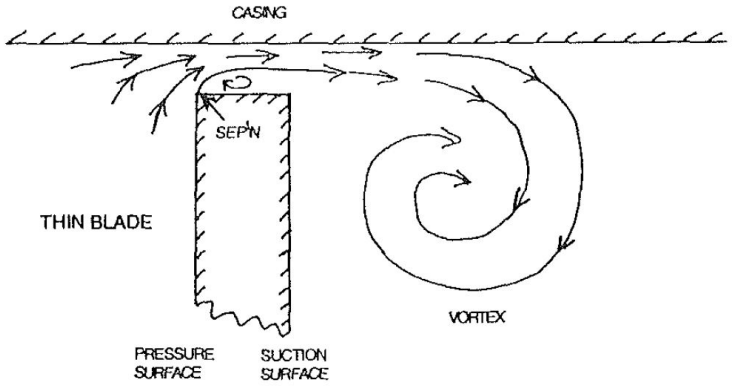

Figure 4.19: Flow over tip gap for unshrouded blade [30]

As mentioned earlier, the mixing of the leakage flow with the main flow during re-entry leads to entropy generation. Assuming of immediate mixing at the interface of leakage flow and main stream for perfect gas case[36], the entropy generation can be written as [37]:

$$\Delta s = C_p \frac{\dot{m_{gap}}}{\dot{m_{main}}} \left[\left(1 + \frac{\gamma+1}{2} M^2_{main} \right) \frac{T_{t,gap} - T_{t,main}}{T_{t,main}} + (\gamma - 1) M^2_{main} \left(1 - \frac{V_{streamwise,gap}}{V_{main}} \right) \right] \tag{4.30}$$

Assuming the tip gap flow having a similar stagnation temperature to the main flow, the first term in the parentheses drops, leaving with just the velocity terms. This fact shows that the mixing process only depends on the leakage flow rate and the difference in the streamwise velocity of the mainstream (suction side) flow and the leakage flow. Equation 4.30 is then reduced to:

$$\Delta s = C_p \frac{d\dot{m}}{\dot{m_{main}}} \left[(\gamma - 1) M^2_{main} \left(1 - \frac{V_p}{V_s} \right) \right] \tag{4.31}$$

For the remaining parameter, we consider the flow illustrated in Figure 4.20. The leakage flow passes over the blade tip with constant chordwise/streamwise velocity component, equal to the pressure side relative velocity w_{ps}. The flow then reaches the suction side, where it mixes immediately with the surrounding flow which has a velocity w_{ss}. Implementing total-static thermodynamic isentropic relation, Equation 4.31 reads:

$$\Delta s = C_p \frac{d\dot{m}}{\dot{m_{main}}} \left[2 \left(\frac{T_t}{T} - 1 \right) \left(1 - \frac{V_p}{V_s} \right) \right] \tag{4.32}$$

In an adiabatic process:

$$C_p (T_t - T) = h_t - h = \frac{v^2}{2} \tag{4.33}$$

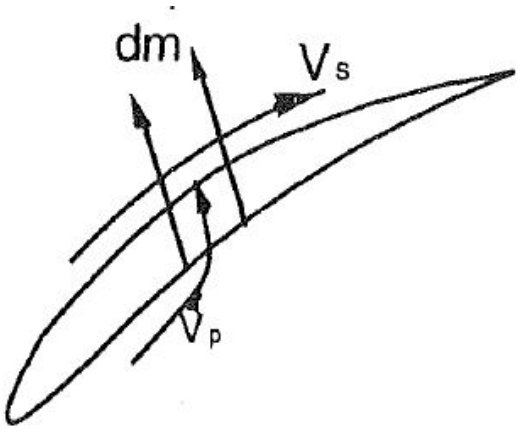

Figure 4.20: Tip leakage viewed as a jet in a crossflow [30]

The terms in Equation 4.31 can then be rewritten:

$$T\Delta s = w_{ss}^2 \left(1 - \frac{w_{ps}}{w_{ss}}\right) \frac{d\dot{m}}{\dot{m}_{main}} \tag{4.34}$$

Compared to Equation 4.31, Equation 4.34 is more generally valid, as it contains no perfect gas assumption. On the other hand, the infinitesimal leakage mass flow rate $d\dot{m}$, which can be calculated by assuming two-dimensional flow and applying the momentum equation in the direction perpendicular to the blade chord. The simplest way to do this step is to assume incompressible flow, which reduces the momentum equation into the well-known discharge equation:

$$d\bar{m} = C_c g \sqrt{2\Delta P \rho} dz \tag{4.35}$$

where g, C_c and dz refer to tip clearance, discharge coefficient and the infinitesimal chord length. This assumption may seem counter-intuitive in a general loss model. Nevertheless, the leakage flow is relatively small compared to the main flow. In turn, the compressibility effect within the leakage flow will not significantly affect the main flow, justifying the use of incompressible flow assumption in the leakage flow. Combining Equations 4.34 and 4.35, the entropy generation reads:

$$T\Delta s = \frac{1}{\dot{m}_{main}} w_{ss}^2 \left(1 - \frac{w_{ps}}{w_{ss}}\right) C_c g \sqrt{2\left(p_{ps} - p_{ss}\right)\rho_{ss}} dz \tag{4.36}$$

The unknowns from Equation 4.36 can be grouped into two categories, C_c and the flow quantities at the suction and pressure surface(w_{ps}, w_{ss}, p_{ps}, p_{ss} and ρ_{ss}). After obtaining the blade surface velocity distribution using the method explained in Subsection 4.2.1, the flow quantities can be obtained. The value of C_c, however, is usually not known in the preliminary design step.
The actual value of the discharge coefficient can be calculated theoretically assuming two-dimensional flow, as performed in the model of Moore and Tilton [38]. Nevertheless, the relative motion between the blade and the casing also play a role in the pressure gradient in the clearance gap. For turbines, Morphis and Bindon [39] and Yaras and Sjolander [40] found that the relative motion increases the pressure on the suction side of the clearance gap, while the flow pattern is not affected. The increased suction side pressure means the leakage flow, and hence, the loss generated due to tip leakage is diminished. Indeed, the discharge coefficient was approximately halved by this effect at full tip speed [40]. On the other hand, in compressors, the effect of this relative motion is the opposite; it increases the leakage flow, which corresponds to higher values of C_c compared to that of stationary rows [30]. Based on this facts, and due to the lack of data regarding the value of C_c for compressors, the value of C_c is fixed at 0.8. This conservative approach is based on the work of Storer on axial compressors [36]. After fixing an appropriate value for the constant C_c, the entropy generation due to tip leakage is then obtained by integrating the Equation 4.36 along the blade chord:

$$T\Delta s = \frac{C_c g}{\dot{m}_{main}} \int_0^{l_\theta} W_{ss}^2 \left(1 - \frac{W_{ps}}{W_{ss}}\right) \sqrt{2\rho_{ss}\left(p_{ps} - p_{ss}\right)} ds \tag{4.37}$$

5

Meanline Design of Centrifugal Compressor

In this chapter, the technical approach to construct a preliminary design framework for a centrifugal compressor is explained. The concept of meanline design is introduced, then the algorithm developed in this work is described in details.
The usual practice to perform the preliminary design of turbomachinery stages is to resort to a lumped parameters approach, named meanline framework. The fundamental assumptions underlying this method are:

- evaluate the flow quantities at midspan of the blade, at the inlet and outlet of each blade row
- refer to the pitch-wise average values of the flow quantities
- account for three-dimensional effect and loss generation by means of loss models.

An overview of the workflow of the preliminary method developed in this work is shown in the flowchart in Figure 5.1. Recalling Equation 2.24,

$$\eta_{tt} = f(\phi_{t1}, \psi, \beta_{tt}, \gamma_{pv}, Re, \sigma)$$

the efficiency of a centrifugal compressor stage can be expressed in terms of six parameters. The input parameters required to determine the impeller efficiency are:

- Work coefficient and swallowing capacity, ψ and ϕ_{t1}
- Compression ratio, β_{tt}
- Reduced inlet thermodynamic properties, p_r and T_r. Together with β_{tt} and the working fluid, they univocally determine the thermodynamic state throughout the compression process, and thus, the average value assumed by γ_{Pv}.
- Working fluid
- A set of geometrical parameter, $\sigma = \left[k, \frac{g}{H_2}, \delta_{bl} \text{ and } r_2\right]$. The remaining parameters from Equation 2.21: number of blades (Z), flow length (l_θ), diameter ratio ($\frac{D_{1s}}{D_2}$) and outlet blade height (H_2) are computed by the internal routines. The estimation of l_θ is discussed in Subsection 5.5
- Inlet absolute flow angle α_1
- Unlike what is stated in Equation 2.24, global and local impeller Reynolds number is omitted from the input. The value of Re affects the loss model computation, i.e. for C_d value determination. However, in this work, fully turbulent flow in the blade passage are assumed, thus eliminating any dependence on the exact value of Re.

Focusing on the flowchart at Figure 5.1, the steps to determine impeller efficiency can be summarized as:

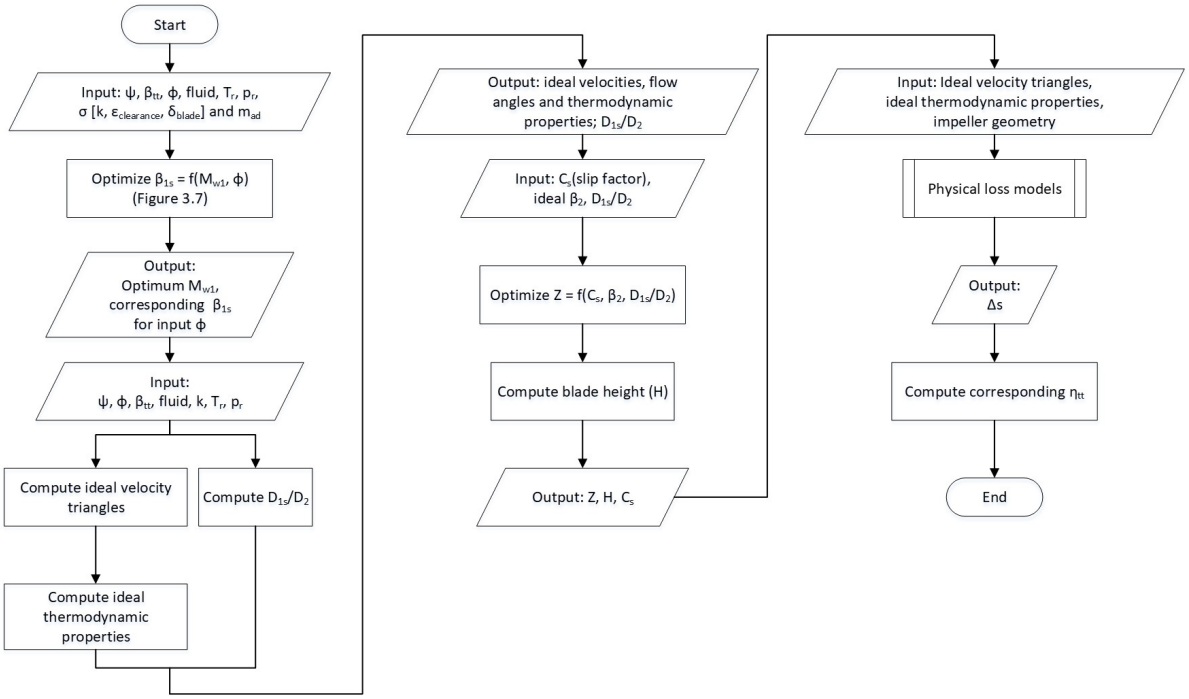

Figure 5.1: Flowchart of the mean-line design routine

1. Calculate the inlet optimum flow angle β_{1s}, optimizing the inlet relative Mach number M_{w1} and the swallowing capacity ϕ_{t1} and the corresponding diameter ratio, see Section 5.1

2. Compute the ideal velocity triangles at midspan, see Section 5.2

3. Compute the ideal thermodynamic properties at midspan, see Section 5.3

4. Estimate the blade number, see Section 5.4

5. Calculate the mass flow rate and blade height using continuity:

$$H_{1,2} = \frac{\dot{m}}{2\rho_{1,2}\, v_{m1,2}\pi r_{m1,2}}$$

where, (5.1)

$$\dot{m} = \rho_1\, v_{m1}\pi k\left(\frac{D_{1s}}{D_2}\right)^2 r_2^2$$

6. Apply the loss model discussed in Chapter 3, with the novel boundary layer and tip leakage loss replacing the empirical blade loading loss and empirical clearance loss, respectively.

7. Compute the actual thermodynamic properties and the corresponding velocity triangles at midspan

8. Compute the total-to-total efficiency of the impeller:

$$\eta_{tt} = \frac{h_{t2s} - h_{t1}}{h_{t2} - h_{t1}} \tag{5.2}$$

To reproduce the equivalent Smith's chart, the values of ϕ_{t1} and ψ is then varied. For the Casey's chart, on the other hand, the analysis is done at a range of ϕ_{t1} and β_{tt}. The computed efficiency of each combination corresponds to the impeller design. A more detailed explanation of the algorithm is provided in the following subsections.

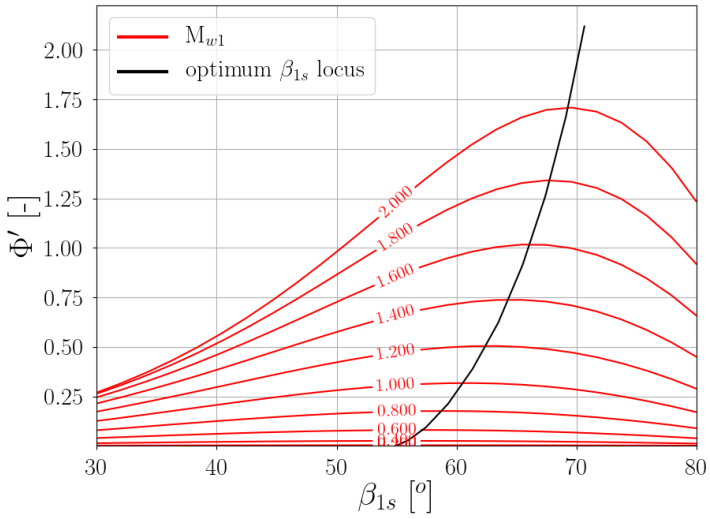

Figure 5.2: Modified mass flow function (Φ') as a function of relative inlet Mach (M_{w1}) and inlet flow angle (β_1). The locus of optimum flow angle (β_{1s}) is shown as the black line. Working fluid = air.

5.1. Optimum Flow Angle Calculation

In a centrifugal compressor, the maximum Mach number is located in the inlet shroud. The high Mach number means that shock loss is generated strongly in the vicinity of this area. To achieve maximum efficiency, shock losses in the inlet must be reduced, which means the value of M_{w1} must be reduced. Casey [11] investigated this effect and found out that for a given inlet mass flow function there is a certain inlet angle leading to the minimum relative inlet Mach number, as shown in Figure 5.2.

The modified mass flow function (Φ') from Figure 5.2 is another form of flow coefficient. It is defined as the ratio of the mass flow rate to a reference mass flow passing through an area of D_2^2 with a velocity equal to the total sonic inlet velocity and with a density equal to the total inlet density, which reads:

$$\Phi = \frac{\dot{m}}{\rho_{t1} D_2^2 a_{t1}} = \phi_{t1} M_{u2} \quad \text{where} \quad M_{u2} = \frac{u_2}{a_{t1}} \tag{5.3}$$

This form of flow coefficient is used when engineers want to emphasize the flow compressibility effect and its variation with speed and inlet conditions [16]. To establish a link with the optimum relative inlet angle, the massflow function is rewritten in terms of M_{w1} and β_{1s}:

$$\Phi = \frac{\rho_1 v_{m1} A_1}{\rho_{t1} D_2^2 a_{t1}} \quad \text{with} \quad A_1 = \pi \left(r_{1s}^2 - r_{1h}^2\right) = \pi k r_{1s}^2 \tag{5.4}$$

Referring to the inlet velocity triangle in Figure 5.3, the basic relation of the velocities is:

$$v_{m1} = w_1 \cos\beta_{1s} and u_1 = w_1 \left(\cos\beta_{1s} \tan\alpha_1 + \sin\beta_1\right) \tag{5.5}$$

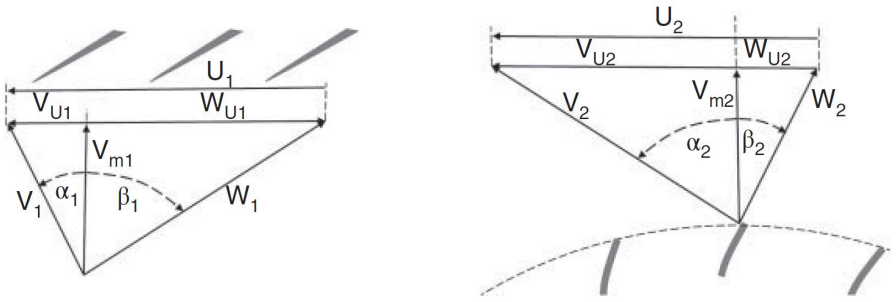

Figure 5.3: Centrifugal pump impeller and velocity triangles [4], $c = v$ = absolute velocities

substituting Equation 5.5 to Equation 5.4 yields:

$$\Phi = k\frac{\pi}{4}\frac{\rho_1}{\rho_{t1}}\frac{w_1}{a_{t1}}\left(\frac{D_{1s}}{D_2}\right)^2\cos\beta_{1s}$$

or

$$\Phi = k\frac{\pi}{4}\frac{\rho_1}{\rho_{t1}}\frac{w_1}{a_{t1}}\left(\frac{u_{1s}}{u_2}\right)^2\cos\beta_{1s} \tag{5.6}$$

hence,

$$\Phi = k\frac{\pi}{4}\frac{\rho_1}{\rho_{t1}}\frac{a_1^3}{a_{t1}^3}\frac{w_1^3}{a_1^3}\frac{a_{t1}^2}{u_2^2}\cos\beta_{1s}\left(\cos\beta_{1s}\tan\alpha_1+\sin\beta_1\right)^2$$

Using the definition of inlet relative Mach number, $M_{w1} = \frac{w_1}{a_1}$ and M_{u2} definition in Equation 5.3, the previous equation can be rewritten to yield:

$$\Phi = k\frac{\pi}{4}\frac{\rho_1}{\rho_{t1}}\frac{a_1^3}{a_{t1}^3}M_{w1}^3M_{u2}^2\cos\beta_{1s}\left(\cos\beta_{1s}\tan\alpha_1+\sin\beta_1\right)^2$$

or (5.7)

$$\Phi' = \Phi\frac{4M_{u2}^2}{k\pi} = M_{w1}^3\frac{\rho_1}{\rho_{t1}}\frac{a_1^3}{a_{t1}^3}\cos\beta_{1s}\left(\cos\beta_{1s}\tan\alpha_1+\sin\beta_1\right)^2$$

Referring back to Casey's work [11] in Figure 5.2, the optimal inlet angle corresponds to the maximum of Φ' at a given inlet relative Mach, shown as the black locus line. To compute this locus line, Equation 5.7 must first be analyzed. Nevertheless, to use this equation, the inlet velocity triangle is needed. The inlet velocity triangle is in turn determined by the choice of β_{1s}, as shown in Equation 5.5. Therefore, to solve this set of equations, an iterative loop is used. The optimum relative inlet angle can then be obtained by taking the $\frac{d\Phi'}{d\beta_{1s}} = 0$. The calculation flow of inlet relative optimum angle, β_{1s}, can be seen in the flowchart in Figure 5.4, and is summarized as:

1. Take an arbitrary value of β_{1s}
2. Take a guess value of a_1
3. Calculate w_1 and v_1 using the arbitrary β_{1s} value
4. Calculate h_1 using total-static enthalpy relation:

$$h_1 = h_{t1} - \frac{v_1^2}{2} \tag{5.8}$$

5. Compute the value of a_1 using implicit thermodynamic equation of state
6. Converge on a_1 value, then compute the modified mass flow function (Φ') value using Equation 5.7
7. Iterate on β_{1s} and repeat steps 2-6 to yield a maximized value of Φ' and the corresponding value of optimum β_{1s}

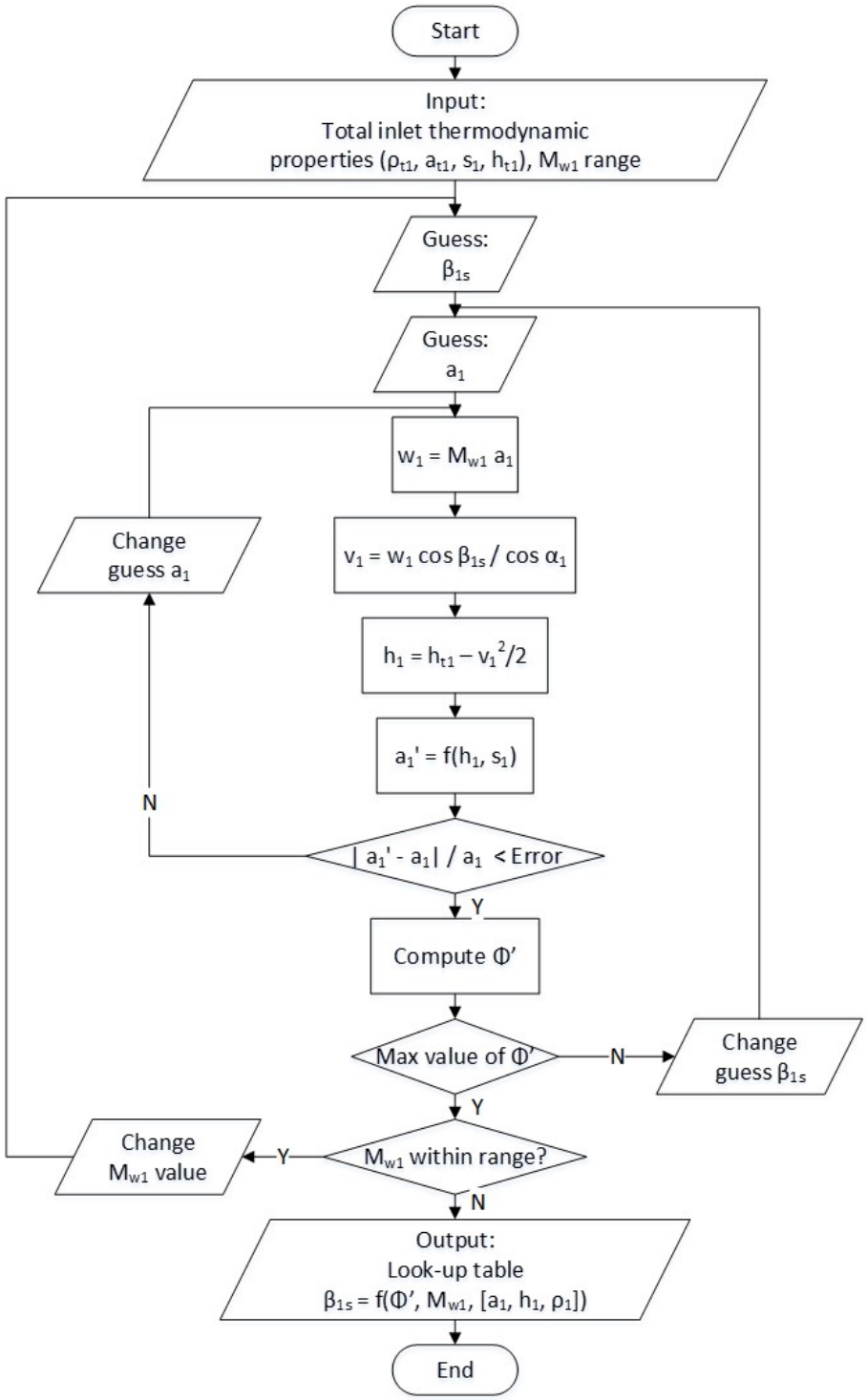

Figure 5.4: Flowchart of optimum inlet relative flow angle calculation internal routine

8. Repeat the whole procedure for a range of M_{w1} values

The values of the optimum relative inlet angle and the corresponding relative inlet Mach number and the modified mass flow function is stored in an internal lookup table. In the meanline routine, the values of β_{1s}, M_{w1} and other corresponding values can be retrieved from this table.

5.2. Velocity Triangle Computation

The duty coefficients ϕ_{t1} and ψ, as introduced in Section 2.2, govern the shape of the impeller inlet and outlet velocity triangles. The work coefficient (ψ) is defined as:

$$\psi = \frac{h_{t2s} - h_{t1}}{u_2^2} \tag{5.9}$$

where the value of total isentropic outlet enthalpy (h_{t2s}) can be obtained from the compression ratio,

$$\beta_{tt} = \frac{p_{t2}}{p_{t1}} \tag{5.10}$$

using the implicit thermodynamic equation of state,

$$h_{t2s} = f\left(p_{t2}, s1, fluid\right) \tag{5.11}$$

from Equation 5.9 - 5.11, the value of impeller outlet peripheral speed (u_s) can be calculated. Using the obtained value of u_2, based on Equation 5.7, the modified mass flow function (Φ') can be calculated using:

$$\Phi' = \Phi \frac{4M_{u2}^2}{k\pi} = \phi_{t1} \frac{4\left(\frac{u_2}{a_{t1}}\right)^3}{k\pi} \tag{5.12}$$

The corresponding value of inlet optimum relative angle (β_{1s}), inlet relative Mach number (M_{w1}) and static inlet thermodynamic properties (a_1, h_1 and ρ_1) can then be obtained as discussed in Section 5.1.
The remaining components of the velocity triangle can be calculated using the identity of the velocity triangles:

$$\begin{aligned} v_1 &= w_1 \frac{\cos\beta_{1s}}{\cos\alpha_1} \\ u_1 &= v_1 \sin\alpha_1 - w_1 \sin\beta_{1s} \\ v_{m1} &= v_1 \cos\alpha_1 \\ v_{tg1} &= v_1 \sin\alpha_1 \\ w_{tg1} &= w_1 \sin\beta_{1s} \end{aligned} \tag{5.13}$$

The outlet isentropic triangle can then be computed first using the definition of work coefficient in Equation 5.9, which when combined with Euler equation for compressors reads:

$$\begin{aligned} \Delta h_t &= u_2 v_{tg2} - u_1 v_{tg1} \\ hence, & \\ \psi &= \frac{u_2 v_{tg2} - u_1 v_{tg1}}{u_2^2} \end{aligned} \tag{5.14}$$

The rest of the ideal outlet velocity triangle can be obtained using the identity based on Figure 5.3:

$$\begin{aligned} w_{tg2} &= v_{tg2} - u_2 \\ v_2 &= \sqrt{v_{tg2}^2 + v_{m2}^2} \\ w_2 &= \sqrt{w_{tg2}^2 + v_{m2}^2} \\ \alpha_2 &= \arctan\frac{v_{tg2}}{v_{m2}} \\ \beta_2 &= \arctan\frac{w_{tg2}}{v_{m2}} \end{aligned} \tag{5.15}$$

From Equations 5.13 and 5.15, two major assumptions is required to close the problem:

- Inlet absolute angle (α_1), assumed as ($\alpha_1 = 0$)
- Meridional outlet velocity (v_{m2} or w_{m2}), assumed as $v_{m2} = v_{m1}$

5.3. Thermodynamic Properties Calculation

Assuming isentropic flow, the thermodynamic properties of the flow are determined by the working fluid, reduced inlet thermodynamic properties and velocity triangles:

- Inlet:

$$\begin{aligned} h_{t1}, a_{t1}, \rho_{t1} &= f\left(p_{t1}, T_{t1}, fluid\right) \\ s_1 &= f\left(p_{t1}, T_{t1}, fluid\right) \\ h_1 &= h_{t1} - \frac{v_1^2}{2} \\ static\ quantities_1 &= f\left(h_1, s_1, fluid\right) \\ Roth_1 &= h_1 + \frac{w_1^2}{2} - \frac{u_1^2}{2} \end{aligned} \tag{5.16}$$

- Outlet:

$$\begin{aligned} s_2 &= s_1 \\ h_{t2s}, \rho_{t1} &= f\left(p_{t2}, s_2, fluid\right) \\ Roth_2 &= Roth_1 \\ h_2 &= Roth_2 - \frac{w_2^2}{2} + \frac{u_2^2}{2} \\ static\ quantities_{2s} &= f\left(h_2, s_1, fluid\right) \end{aligned} \tag{5.17}$$

Using the two equations above, the real thermodynamic properties can also be computed, by exchanging the ideal velocity triangle quantities with their real counterparts, as well as implementing the entropy generation calculated from the loss model.

5.4. Blade Number Estimation

The impact of blade count in radial machines is not yet well understood. The choice of blade number in centrifugal compressor design is mostly dictated by manufacturing constraint, rather than fluid dynamic consideration. Nevertheless, mathematically speaking, the blade number is also an important geometric parameter in the input set. The value of blade number determines the blade channel width, which is the input needed in the loss models. This parameter is, however, strongly related to another important parameter in turbomachinery design, slip factor C_s. Due to the inherent rotational flow at the outlet and also due to the limited number of blades, the outlet flow is not perfectly guided by the blade at the impeller exit. The slip factor/slip coefficient, C_s, is the percent increase in tangential relative outlet velocity with respect to exit tangential velocity, w_{tg2}, as seen in Figure 5.5:

$$C_s = 1 - \frac{\Delta w_{tg2}}{u_2} \tag{5.18}$$

From Figure 5.5, it can be inferred that the more blades are used in an impeller, the less the slip velocity is. Indeed, Wiesner [41] derived an empirical correlation relating the two parameters by fitting a number of experimental data acquired from standard centrifugal compressor stages operating with air. Although this choice of the empirical model goes against the goal of the current work in developing a physical model, the effect of a large error (20%) in the choice of slip coefficient only yields a small (5%) drop in work [16], hence, the empirical approach for this matter is considered to be enough. Wiesner's empirical model is written as:

$$C_s = 1 - \frac{\sqrt{\cos\beta_{2,bl}}}{Z^{0.7}} \tag{5.19}$$

which is applicable up to a blade solidity limit sol_{lim} of:

$$sol_{lim} = \frac{D_{1s}}{D_2} \approx \frac{1}{e^{\frac{8.6\cos\beta_{2,bl}}{N}}} \tag{5.20}$$

Equations 5.19 and 5.20 can be visualized in Figure 5.6. Using this solidity limit, the blade number can then be computed. The steps to compute the blade number is summarized as:

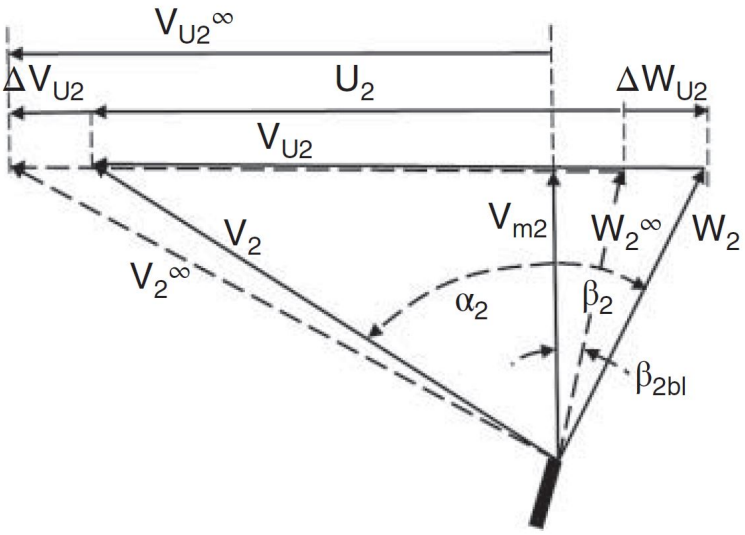

Figure 5.5: Impeller exit velocity triangles with and without slip [27], the subscript ∞ indicates outlet flow without slip

1. Take β_2 as a guess $\beta_{2,bl}$
2. Compute the limit number of blade using Equation 5.20
3. Use Equation 5.19 to calculate the slip factor
4. Compute the slipped value of w_{tg2}:

$$w_{tg2,slipped} = w_{t2} - (1 - C_s)\, u_2 \tag{5.21}$$

5. Compute the slipped relative outlet flow angle, $\beta_{2,slip} = \arctan \frac{w_{tg2,slipped}}{v_{m2}}$
6. Repeat steps 2-5 to converge the value of $\beta_{2,bl}$ towards $\beta_{2,slip}$
7. After convergence, compute the blade number (N), using Equation 5.20 and a scaling parameter n.

$$n\frac{D_{1s}}{D_2} = \frac{1}{e^{\frac{8.6\cos\beta_{2,bl}}{N}}} \tag{5.22}$$

in this work, n is assumed to be 0.8. This diameter ratio scaling parameter is to ensure the validity of Equation 5.19 (stay on the left side of the limiting line in Figure 5.6).

5.5. Flow Length Estimation

Flow length (l_θ) is another important geometric parameter in the input set. The choice of l_θ impact the loss generation as it directly affects the blade velocity distribution (as discussed in Subsection 4.2.1). However, in the preliminary approach, such parameter's value is seldom known, as it is related to the blade camberline length, which is analyzed in the 3-dimensional blade design step. Nevertheless, an approximated value is enough to close the problem. To approximate the value of l_θ, the volume diagonal of the blade is first analyzed, as seen in Figure 5.7. The tangential projection of the flow length is assumed to be similar to the outlet blade pitch:

$$\frac{2\pi r_2}{Z} \tag{5.23}$$

On the other hand, the flow length radial projection is the difference between the inlet and outlet radius ($r_2 - r_1$), while the axial projection reads:

$$C_{ax} - \frac{H_2}{2} \tag{5.24}$$

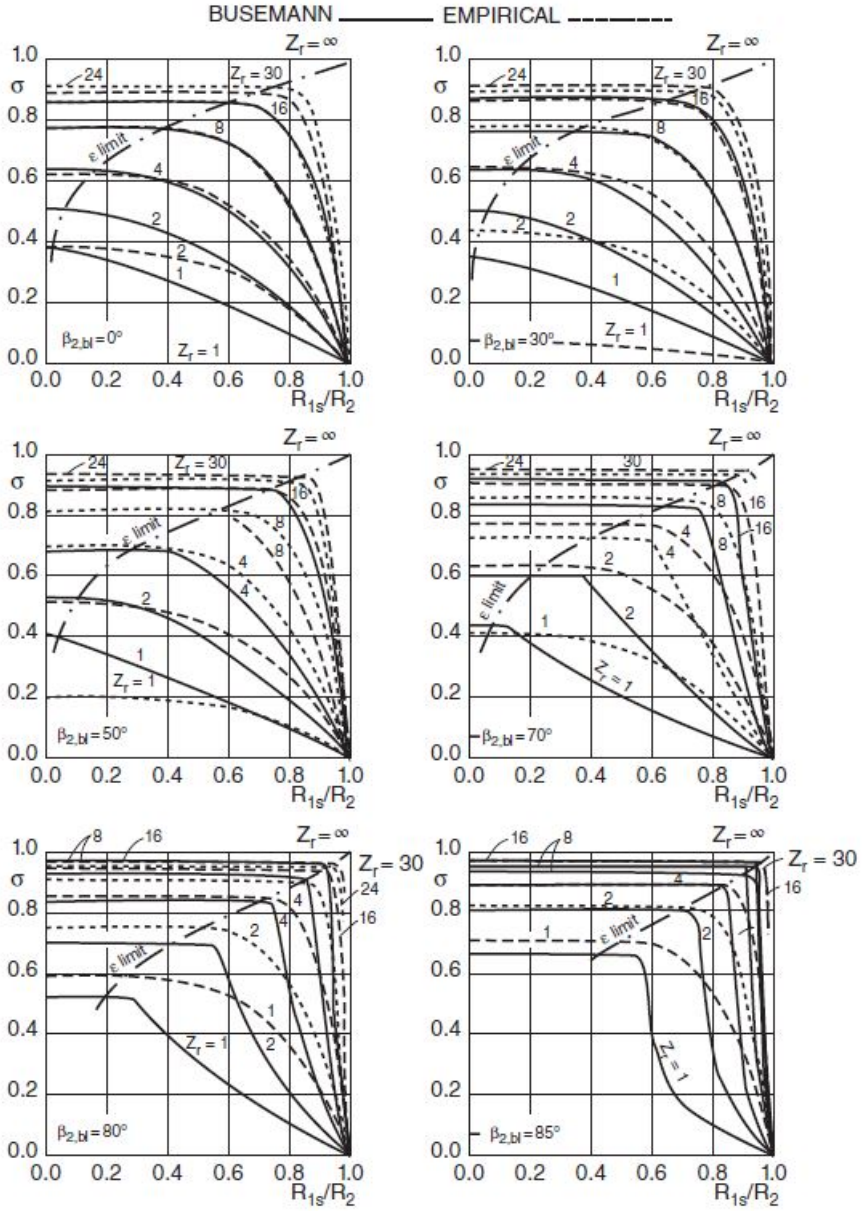

Figure 5.6: Variation of the slip factor according to Busemann and Wiesner [41], the diagonal dash-dotted line (line ϵ_{limit}) represents the solidity limit in Equation 5.20

The volume diagonal is then calculated as the vector resultant of the three projection, which reads:

$$volume\,diagonal = l_{\theta,min} = \sqrt{\left(C_{ax} - \frac{H_2}{2}\right)^2 + (r_2 - r_1)^2 + \left(\frac{2\pi r_2}{Z}\right)^2} \tag{5.25}$$

This volume diagonal is the minimum value of l_θ, as the impeller flow length logically cannot be shorter than the minimum distance between two farthest points in the impeller (the volume diagonal). On the other hand, the flow length also cannot be larger than the largest distance between said two points, which is the sum of the flow length projection in the axial, tangential and radial direction, which can be written as:

$$projection\,sum = l_{\theta,max} = C_{ax} - \frac{H_2}{2} + \frac{2\pi r_2}{Z} + r_2 - r_1 \tag{5.26}$$

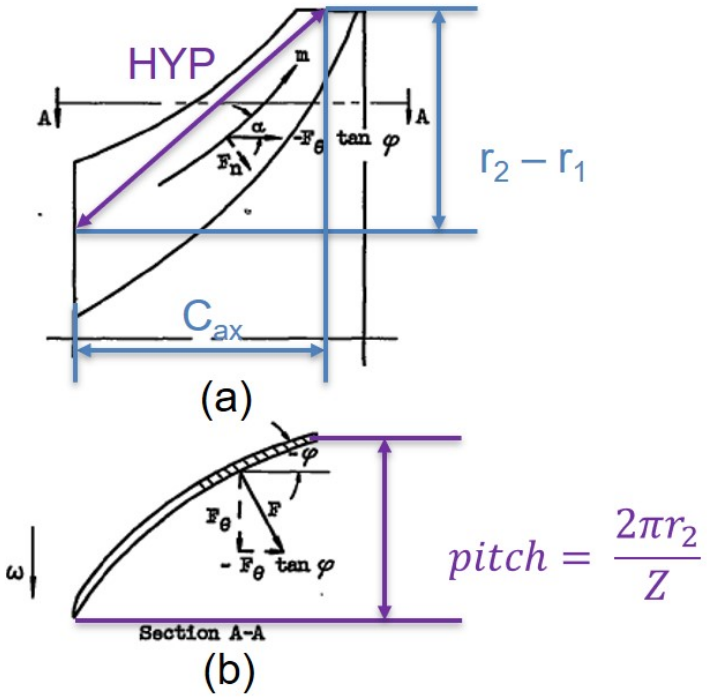

Figure 5.7: Approximation of flow length

The approximate flow length can then be calculated by implementing a multiplication factor for the volume diagonal:

$$l_\theta = C\sqrt{\left(C_{ax} - \frac{H_2}{2}\right)^2 + (r_2 - r_1)^2 + \left(\frac{2\pi r_2}{Z}\right)^2} \tag{5.27}$$

The range of the multiplication factor, C, is 1 <C< $max/min\ ratio$, where the $max/min\ ratio$ is calculated as:

$$max/min\ ratio = \frac{\sqrt{\left(C_{ax} - \frac{H_2}{2}\right)^2 + (r_2 - r_1)^2 + \left(\frac{2\pi r_2}{Z}\right)^2}}{C_{ax} - \frac{H_2}{2} + \frac{2\pi r_2}{Z} + r_2 - r_1} \tag{5.28}$$

For preliminary design, a conservative value is taken to be $C = 1.2$. To close the model, the value of axial length (C_{ax}) must be known. In the works of Al-Zubaidy [42], impeller axial length is taken to be around 0.5-0.6 times the tip radius (r_2). $C_{ax} = 0.5r_2$ is adopted in this work.

6

CFD Validation

This chapter shows the validation of the developed physics-based loss models by means of result comparison with a higher-order numerical method, namely CFD. The first section briefly introduces the CFD software used for validation purposes. The differences between the input parameters of the CFD program and the physics-based loss model is discussed. Then, the test case impeller geometry is described, highlighting the parameter settings used in the CFD program. Finally, the strategies adopted for the validation is described, together with the discussion of the results.

6.1. Multall CFD Solver

To validate the results computed by the novel physics-based loss model result, the Multall program suite [43] is used. Multall is a CFD-based design program developed specifically for turbomachinery applications. The program itself is a collection of 3 programs:

- Meangen, a one-dimensional meanline program
- Stagen, a three-dimensional turbomachinery stage geometry generator
- Multall, a structured, explicit CFD-solver

The main reasons driving the choice of Multall suite to perform the CFD validation, in place of other commercial and open-source CFD codes are:

- developed and tested specifically for turbomachinery application. This specific usage of the program makes it a valuable reference for turbomachinery design framework validation.
- automated meshing. The automatically generated grid is often of unsatisfactory quality for radial turbomachinery. Nevertheless, it represents a good starting point for manual mesh refinement
- low computational cost of the CFD solver.

The three routines are briefly discussed in the following paragraphs.

6.1.1. Meangen

Meangen is a meanline preliminary design program. It is used to produce the input file for Stagen. The important input parameters relevant for centrifugal compressor design are:

- gas properties: heat capacity ratio (γ) and gas constant (R)
- inlet thermodynamic properties: T_{t1} and p_{t1}
- duty coefficients at inlet: ϕ_1 and ψ_1
- rotational speed (Ω)
- mass flow rate ($\dot{m}$)

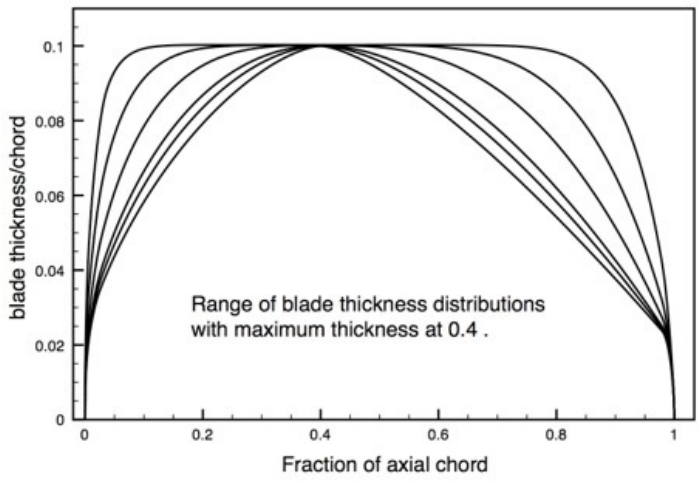

(a)

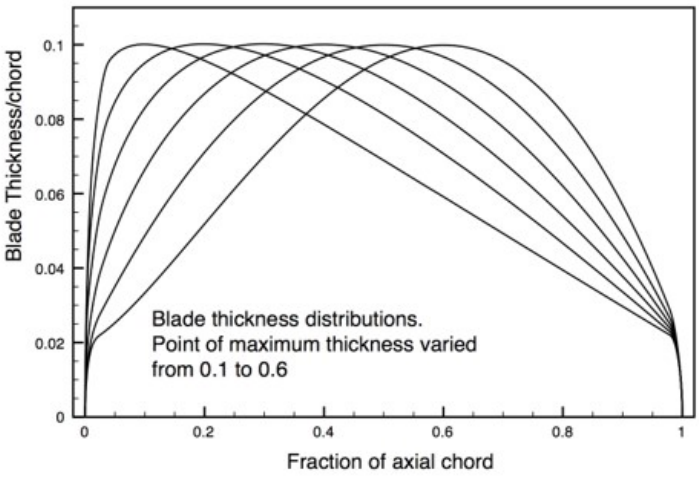

(b)

Figure 6.1: Blade thickness distributions obtained from Stagen (a) for maximum thickness at 0.4 C_{ax}, (b) with C_{ax} varied between 0.1 - 0.6 [43]

- stage inlet and outlet absolute flow angles ($\beta_{1,4}$)
- stream surface coordinate points, as seen in Figure 6.2
- stream surface local meridional velocity ratios, as seen in Figure 6.2
- maximum blade thickness and location of maximum blade thickness for each blade row

For validation purposes in the current work, the geometry of the chosen test case is available in literatures. In turn, the preliminary design step is skipped, and the stage 3-D geometry is directly reproduced with Stagen. The test case geometry is discussed in Subsection 6.2.1, and the input geometry for the Stagen is shown in Appendix B.

6.1.2. Stagen

Stagen is a three-dimensional turbomachinery stage generator. Within this program, the blades are first generated in two dimensions on a plane surface (cartesian) and are then projected onto flow coordinates, i.e. meridional, blade-to-blade and radial planes. In the transformation from the cartesian coordinate to this flow-based coordinate, the x-coordinate in the two-dimensional plane becomes the meridional distance. For example, a flat plat is transformed into a logarithmic spiral. The default strategy to define the two-dimensional blade profile in Stagen is to specify a centre line slope and a mathematically generated thickness

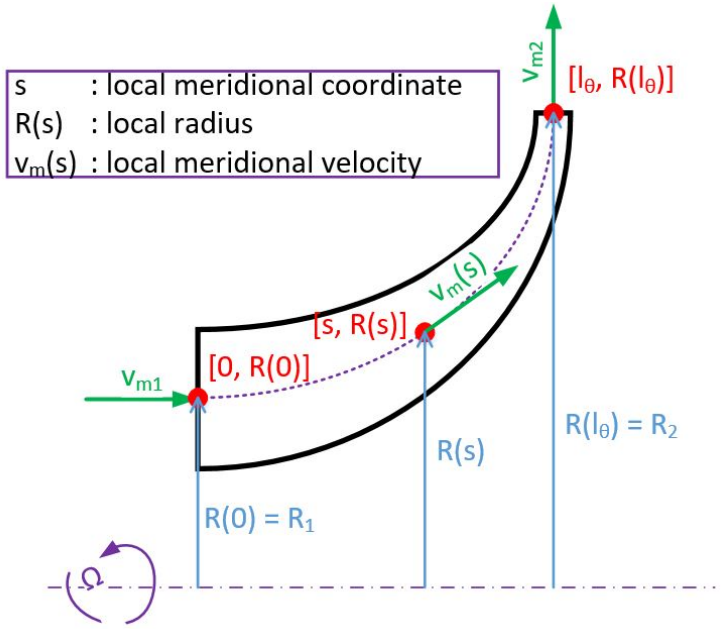

Figure 6.2: Stream surface coordinate points and local velocity, as required for Meangen input.

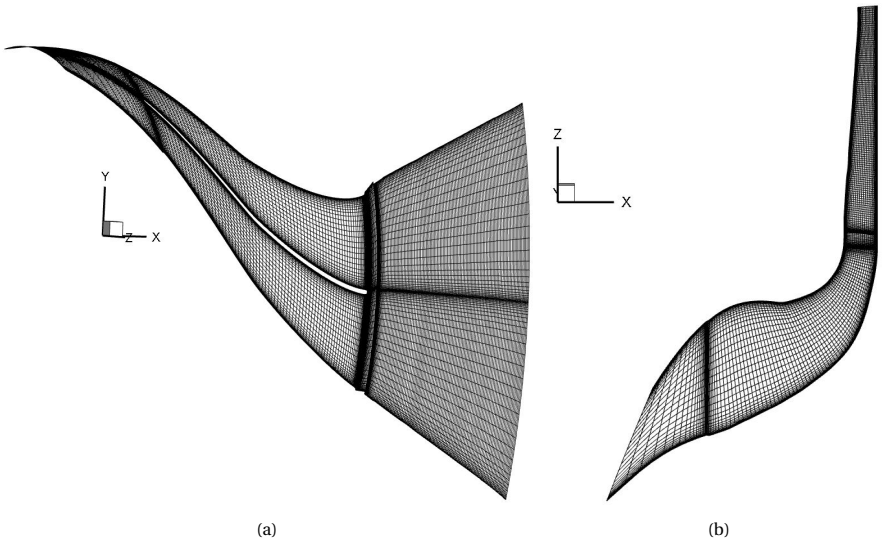

(a) (b)

Figure 6.3: H-grid, approx. 200k cells: (a) blade-to-blade plane, (b) meridional plane

.

distribution, as seen in Figure 6.1.
The initial grid point settings are created in Stagen by inputting the number of the requested grid in front of the leading edge, on the blade surface and after the trailing edge, and the local relative grid spacing in the meridional direction and its location (in percent of the axial chord). Additionally, for the spanwise and pitch-wise direction, the user has to specify the number of requested grid points, their grid expansion ratio and maximum grid spacing ratio. Using the specified settings, the grid is then generated in Multall using an H-grid scheme, as seen in Figure 6.3.
The use of a simple H-grid is usually discouraged in current CFD practice, especially when analyzing complex geometries in CFD analysis. As seen in Figure 6.4a, the use of an H-grid to discretize region near the leading edge causes a highly skewed volume cells in the proximity of a wall. However, the use of cell corner storage in the CFD solver enables an accurate flow field reproduction [43] despite the highly distorted grid, as seen in Figure 6.4b. In Figure 6.4b, the stagnation point is correctly captured.

6.1.3. Multall

Multall is the CFD solver of the program suite. The code is written specifically for turbomachinery applications, using a cylindrical coordinate (x, r, θ) system, and is based on an explicit time-marching finite volume method. The default time-marching algorithm is the "scree" scheme, which is stable and very robust for CFL numbers up to about 0.5. Nevertheless, this scheme is only first-order accurate in time. In seeking a steady-state solution, however, this lack of accuracy does not pose as a limitation [43]. The algorithm can be expressed as:

$$\Delta F = \left(2\frac{\partial F}{\partial t}\Big|_n - \frac{\partial F}{\partial t}\Big|_{n-1}\right)\Delta t \tag{6.1}$$

where F stands for any of the primary variables ($F = \rho, \rho E, \rho v_x, \rho v_r or \rho r v_\theta$). The time-marching scheme is complemented with a fully second-order accurate spatial discretization scheme, which requires very little artificial viscosity to stabilize and works well also at low Mach number (down to around 0.15).
In addition, under-relaxation is also implemented to increase the robustness of the solving algorithm. The idea is to limit the rates of change of the primary variables at grid points where the calculated rates of change are largest [43]. For all cells, the fluxes are first summed and then divided by the local time step to yield the rate of change, Δ_{calc}. These values are then averaged to yield Δ_{ave}. The actual rate of change of the primary for the next time step is then computed as:

$$\begin{aligned} \Delta_{used} &= \frac{\Delta_{calc}}{1+D} \\ \text{where,} & \\ D &= \frac{|\Delta_{calc}|}{Damping\,\Delta_{ave}} \end{aligned} \tag{6.2}$$

Damping is an input variable in Multall routine which is used to control the amount of under-relaxation. Cells with a comparable/greater value of denominator for the variable D have a reduced rate of change, therefore acting as a local stabilizing factor. Typical values of DAMP are 10 – 25, but lower values may be used for complex cases [43].
Another integral part of the CFD solver is the turbulence model. In Multall, viscous terms are included via body forces and source terms. The viscous terms are update every 5 time steps to reduce the computational cost. The wall shear stresses are obtained from wall functions. The wall shear stress is predicted from the local Reynolds number from the second grid point to the wall, and the fitted into a standard logarithmic distribution for turbulent boundary layers. This approximation gives a very good fit to the shear stress obtained from the standard log law over the range of Yplus from 10 to 1000 (within 1% [43]).
There are three choices of viscous models in Multall. The default one is a simple mixing length model, where

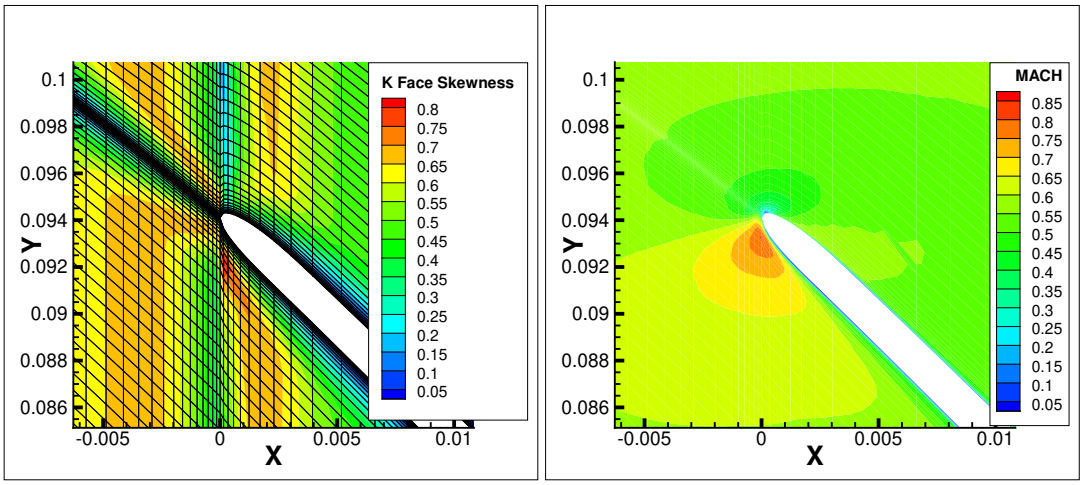

(a) (b)

Figure 6.4: (a) K-face distortion (skewness) around an impeller blade leading edge, face skewness computed by Tecplot ®. (b) Mach contour around an impeller blade leading edge, analyzed using the grid in Figure 6.4a. Eckardt-O Impeller. p_{t4} = 185851.3 Pa, 14000 RPM

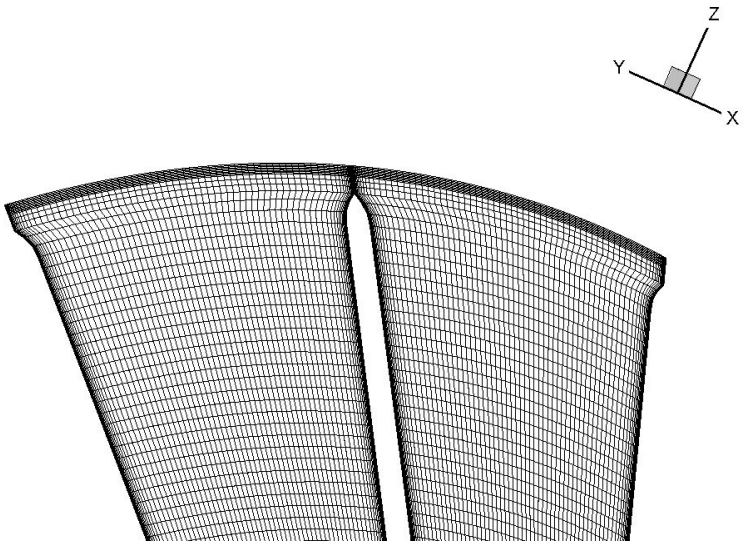

Figure 6.5: Example pinched tip model and tip gap grid distribution in Multall

the mixing length is taken to vary linearly with distance from a wall up to a specified limit (a fraction of local blade pitch, usually 0.03). Lower values give lower turbulent viscosity at the edge of the boundary layer and vice versa. The second choice is a modified version of the mixing length model. In this model, the mixing length limit is computed as the distance of the mid-span and mid-pitch point to the nearest wall. Using this model requires an additional input of scaling factor for each blade row at the inlet, leading and trailing edge, and outlet. The third and most complex choice is the Spalart-Almaras turbulence model. Using this model causes an increase in approximately 20% more CPU time compared to when using this simple mixing length model. The CFD analyses in the current work are performed using the simple mixing loss model due to its robustness and reduced computational cost.
Another important feature of Multall is the mixing plane model. To achieve a steady-state flow solution of turbomachinery stages constituted by multiple blade rows in relative motion, the model has to allow instantaneous mixing between blade rows, reproducing the entropy values that would be measured. The pitch-wise averaged flux values of the primary variables (mass, momentum and energy) must be conserved, without imposing pitch-wise uniform conditions. To achieve that, the circumferential variation of fluxes at the mixing plane is obtained by extrapolation from the upstream and downstream planes. The level of fluxes is also adjusted to satisfy the conservation equations [44].
Lastly, as discussed earlier, the automatic grid produced by Stagen usually produces an unsatisfactory grid for radial turbomachinery cases. In Multall, it is possible to overwrite the automatic grid by specifying the new relative grid spacing and grid points. The tip gap can also be defined in the input file. The local tip is formed using a pinched-tip model (see Figure 6.5); the blade is thinner towards the tip and periodicity is applied across the tip gap where the blade thickness is set to zero. The gap width is specified as local span at leading and trailing edges. Additionally, the number of the grid in the gap is specified as an input parameter, and the spanwise grid distribution is automatically adjusted by these inputs. A typical value of the number of grid points specified in the tip gap is between 3-5.
As a last remark, a recent development performed at the Power and Propulsion group of Delft University of Technology implements the choice to model a vaneless diffuser for the centrifugal compressor design. The idea of this model is to omit all wall effects on the flow in the diffuser while maintaining the flow periodicity caused by the impeller relative motion.

6.2. Test Case Setting

In this section, the test case impeller used for the CFD validation is described. First, the geometry of the impeller is described, alongside the required inputs for the physics-based loss models and Multall. Then the grid size used in the analysis is chosen based on the grid sensitivity analysis.

Table 6.1: Geometric parameters of Eckardt-O impeller

Parameter	Value
Tip radius (r_2)	0.2 m
Inlet shroud radius (r_{1s})	0.14 m
Inlet hub radius (r_{1h})	0.045 m
Outlet width (H_2)	0.026 m
Flow length (l_θ)	0.136 m
Axial length (C_{ax})	0.13 m
Number of blades (Z)	20
Maximum blade thickness (δ_{bl})	0.0033 m

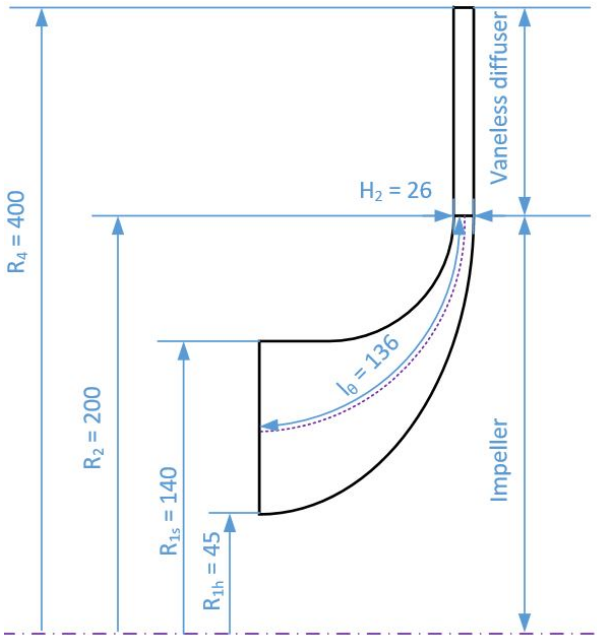

Figure 6.6: Meridional cross-section of the Eckardt-O impeller, dimension in mm [26]

6.2.1. Impeller Geometry and CFD Setting

The test impeller is the Eckardt-O impeller. The driving reason behind this choice of test impeller are:

- Eckardt-O impeller utilizes a vaneless diffuser. with vaneless diffuser, the influence of diffuser on the impeller flow field can be reduced
- experimental data is readily available in literature as a lot of experiments have been performed for this impeller
- the impeller is designed to reproduce the flow field of high-speed centrifugal compressors [26]

The geometric parameters of this impeller are summarized in Table 6.1 and Figure 6.6 [26], [10]. Based on Equation 2.24, the value of shape factor (k) can be calculated as: $k = 1 - \left(\frac{D_{1h}}{D_{1s}}\right)^2 = 0.8967$. Additionally, the tip gap is specified as 3% of H_2 = 0.00078 m. Aside from the geometric parameters, additional settings must be specified in Multall, as listed in Table 6.2. The CFL number and damping value are chosen to increase the stability of the solution algorithm. The choice of the viscous model is a conservative one. The number of grid points used to reproduce the tip gap is larger than the standard value since a detailed resolution of the tip gap flow is desirable for the following analysis. The value is chosen as a trade-off between spatial accuracy and grid quality. Furthermore, as the Eckardt-O impeller uses a vaneless diffuser, the vaneless diffuser flag in Multall is activated. Lastly, the choice of grid size is discussed in depth in the grid convergence analysis subsection.

6.2.2. Grid Convergence Analysis

In performing a CFD analysis, a low number of cells is preferable, as it directly translates to low computational power requirement. However, a coarse grid may cause error due to unsatisfactory spatial discretization. Therefore, the lowest number of cells that leads to a grid-independent result must be chosen. In other words, the number of cells for the analysis is chosen such that if the grid is further refined, similar result will be obtained. This determination of number of cells is named the grid convergence analysis.
The analysis is performed by simulating one test case of the test impeller with input parameter as described in Table 6.3. The coarsest grid is constituted by 37 elements in I direction, 241 in J direction and 37 in K direction. The number of grid points is increased by 9 in I direction, 60 in J direction and 9 in K direction in each simulation, until reaching the finest grid, i.e. 84 x 541 x 84 (I x J x K).. In other words, six simulations are performed, using grid sizes (i x j x k):

- 37 x 241 x 37 = 329929 grids
- 47 x 301 x 47 = 664909 grids
- 56 x 361 x 56 = 1132096 grids
- 65 x 421 x 65 = 1778725 grids
- 74 x 481 x 74 = 2633956 grids
- 84 x 541 x 84 = 3817296 grids

The values of total-to-total efficiency and mass flow rate computed with each grid are displayed in Figure 6.7. The convergence analysis shows about a 1% difference in calculated mass flow rate and about 0.6% difference in efficiency between the last two simulations with the two highest grid density (between i x j x k = 74 x 481 x 74 and 84 x 541 x 84). This small variation is considered acceptable for the present work, and hence, a grid size of (i x j x k) = 74 x 481 x 74 is chosen. This choice represents a reasonable trade-off between accuracy and computational cost, since with the densest grid the simulation took about twice as long as with the chosen gird size.

6.3. Validation Strategy

The choice of settings for Multall shown in Tables 6.1 and 6.2 are used to analyse the off-design test cases of the Eckardt-O impeller. The collection of test operating points is listed in Table 6.4 and shown on the compressor map in Figure 6.8.

To validate the two novel physics-based loss models (boundary layer loss and tip leakage loss mechanism), the efficiency drop caused by each loss mechanism is compared between the model and the one calculated by CFD simulation for each operating point. It is widely known, however, that the loss mechanisms are seldom

Table 6.2: Additional CFD settings for Multall

Parameter	Value
Inlet total temperature (T_{t1})	288 K
Inlet total pressure (p_{t1})	101330 Pa
Inlet tangential velocity (v_{tg1})	0 m/s
Inlet meridional velocity (v_{tg1})	90 m/s
Gas constant (R)	287.5 J/kg K
Heat capacity ratio (γ)	1.4
CFL number	0.25
Damping	15
Continuity error limit	1%
Convergence level	0.3%
Viscous model	Simple mixing length
Tip gap grid number (spanwise)	7
Trailing edge grid number (j-dir)	3
Grid size (i x j x k)	74 x 481 x 74
Vaneless diffuser flag	True

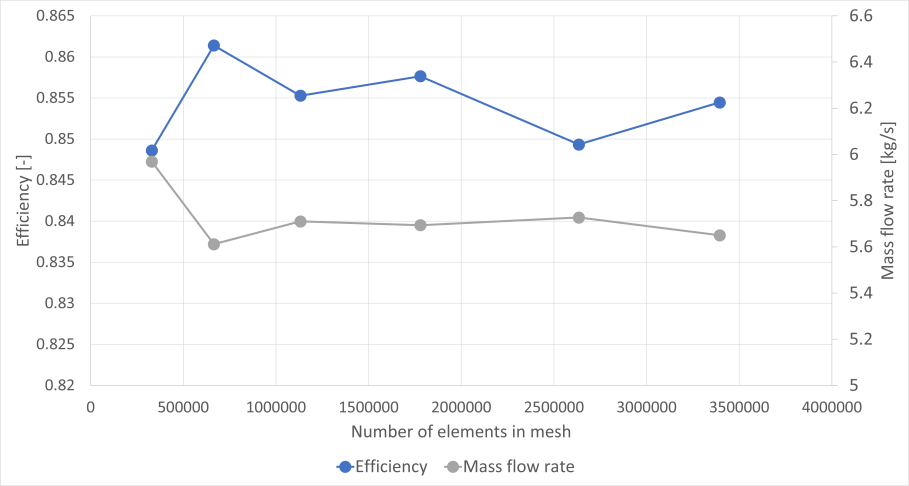

Figure 6.7: Mass flow rate and efficiency with respect to number of grid points

Table 6.3: Grid convergence analysis test case

Parameter	Value
Compressor static outlet pressure (p_{t4})	185851.3 Pa
Impeller rotational speed	14000 rpm

independent of each other [30], [5], [27]. Nevertheless, by choosing carefully the blade section to be analyzed, the effect of the chosen focus loss generation mechanism can still be isolated and the effect of other mechanisms can be minimized.
In analyzing the blade boundary layer loss, to assume that only the blade boundary layer loss affects the entropy generated from leading edge to trailing edge, the possible effects from other loss generation mechanisms has to be minimized. Care should be taken when choosing the local span in which the thermodynamic properties is going to be analysed. Taking a local span too close to the hub endwall means also including the

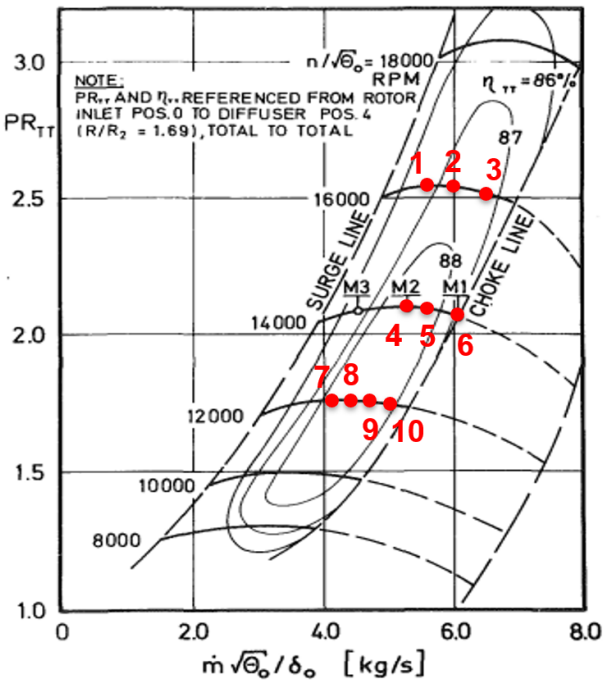

Figure 6.8: Compressor map of Eckardt-O impeller [26] with the test operating points used in the CFD simulation

Table 6.4: Test operating points as seen in Figure 6.8

Case	Mass flow	Pressure ratio (total-to-total)	Input CFD parameter	
			Rotational speed	Outlet static pressure
1	5.78 kg/s	2.450	16000 rpm	222420 Pa
2	5.99 kg/s	2.426	16000 rpm	219635 Pa
3	6.65 kg/s	2.412	16000 rpm	216852 Pa
4	5.52 kg/s	2.024	14000 rpm	185796 Pa
5	5.79 kg/s	2.016	14000 rpm	183943 Pa
6	6.02 kg/s	2.010	14000 rpm	182944 Pa
7	4.35 kg/s	1.711	12000 rpm	159960 Pa
8	4.56 kg/s	1.706	12000 rpm	158962 Pa
9	4.83 kg/s	1.705	12000 rpm	158469 Pa
10	4.99 kg/s	1.701	12000 rpm	157970 Pa

hub endwall boundary effect (as exhibited by the low Mach number along the whole blade channel in Figure 6.10a), and secondary loss (as seen in the vortices near the hub endwall illustrated in Figure 6.9). On the other hand, the chance of flow separation is increased towards the blade tip. From the impeller velocity triangle in Figure 5.3, the following relation of the velocity components at impeller inlet and outlet is written as:

$$\begin{aligned} w_1^2 &= v_1^2 + u_1^2 - 2u_1 v_{t,1} \\ &\text{and} \\ w_2^2 &= v_2^2 + u_2^2 - 2u_2 v_{t,2} \end{aligned} \tag{6.3}$$

The Euler equation for turbomachinery reads:

$$\Delta h_t = u_2 v_{t2} - u_1 v_{t1} \tag{6.4}$$

Combining Equation 6.3 and 6.4 yields

$$\Delta h_t = \frac{1}{2}\left(v_2^2 - v_1^2 + w_1^2 - w_2^2 + u_2^2 - u_1^2\right) \tag{6.5}$$

In centrifugal compressor, the term $u_2^2 - u_1^2$ is higher at the impeller shroud compared with that at the impeller. Hence, the $w_1 \rightarrow w_2$ diffusion has to be greater in the impeller shroud to keep the Δh_t constant at both hub and shroud. This higher diffusion at impeller shroud causes an increased separation chance. Moreover,

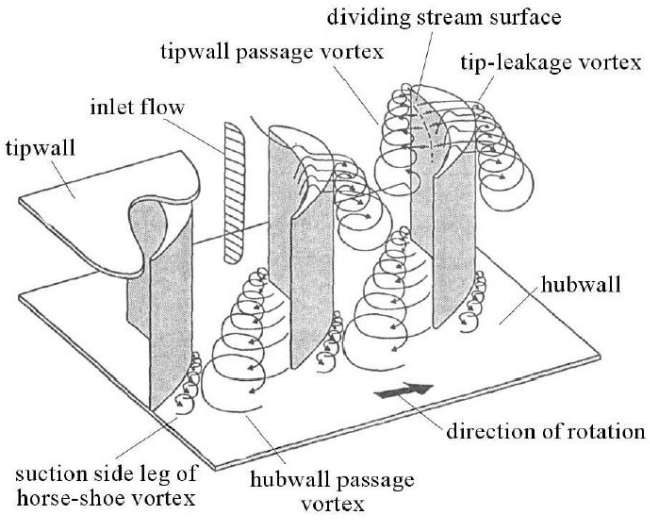

Figure 6.9: Vortices at the tip endwall in presence of clearance [45]

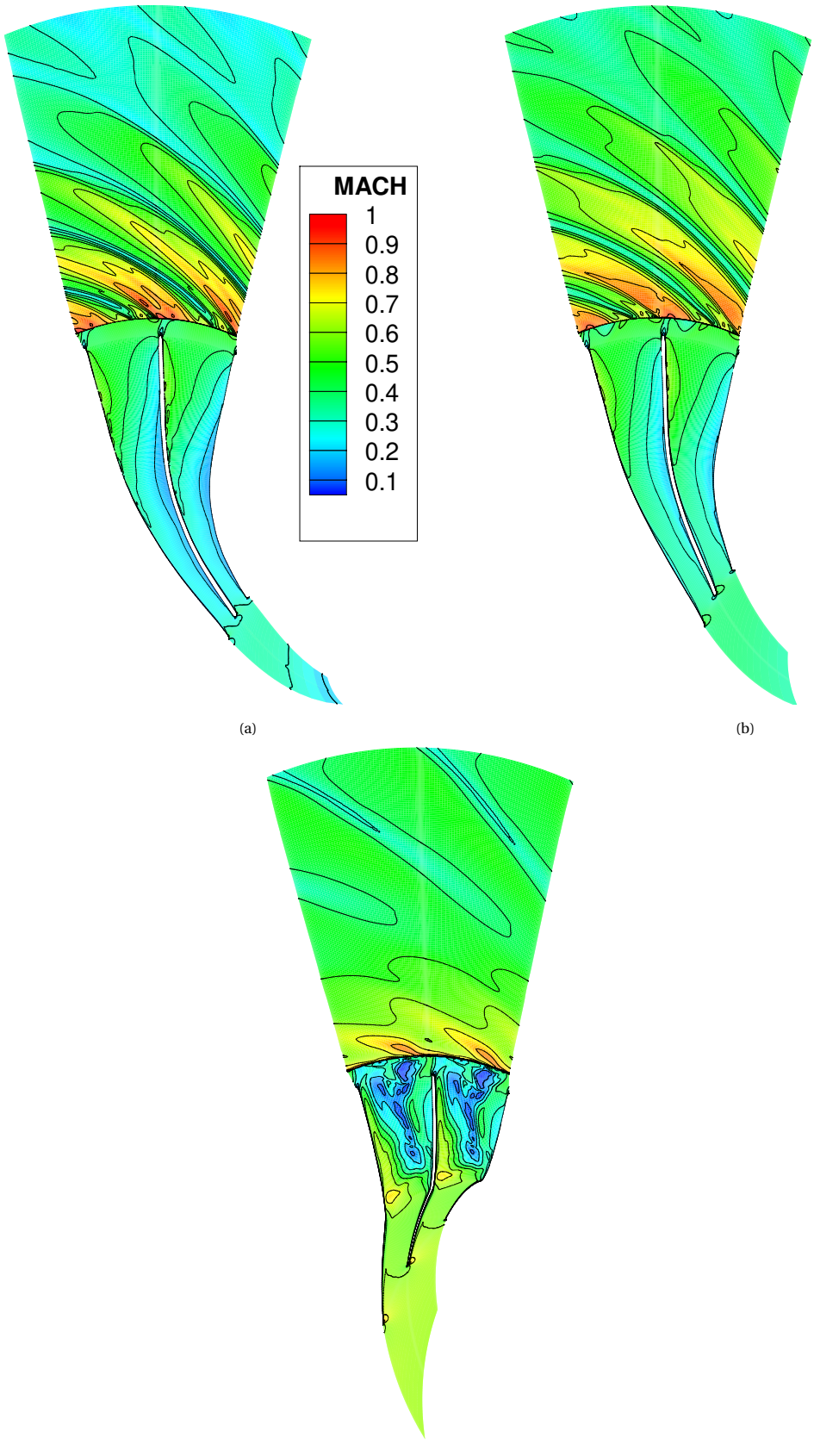

Figure 6.10: Relative Mach number in the blade-to-blade plane at: (a) 5% span, (b) 20% span and (c) 92% span, operating point 4 from Table 6.4

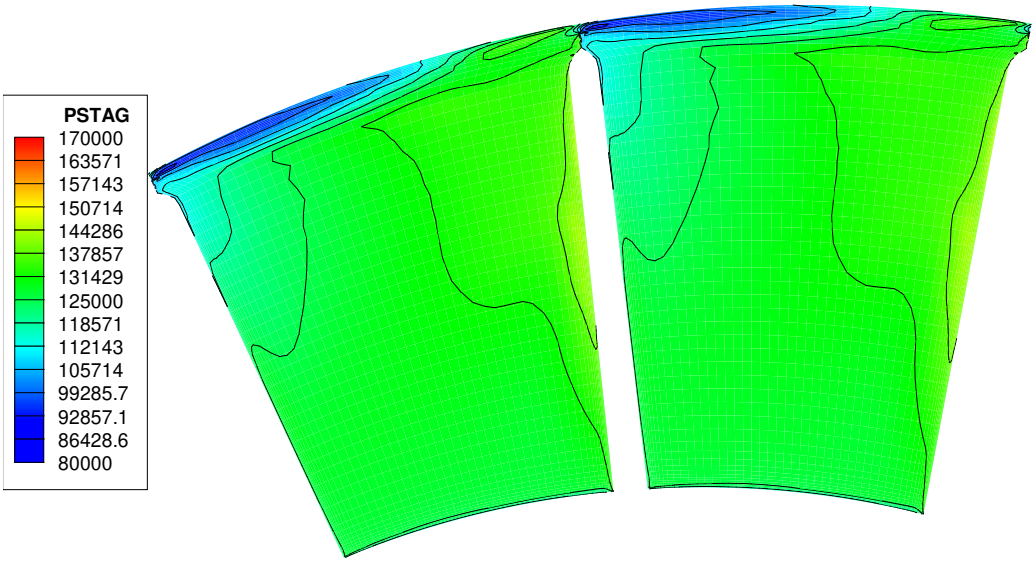

(a)

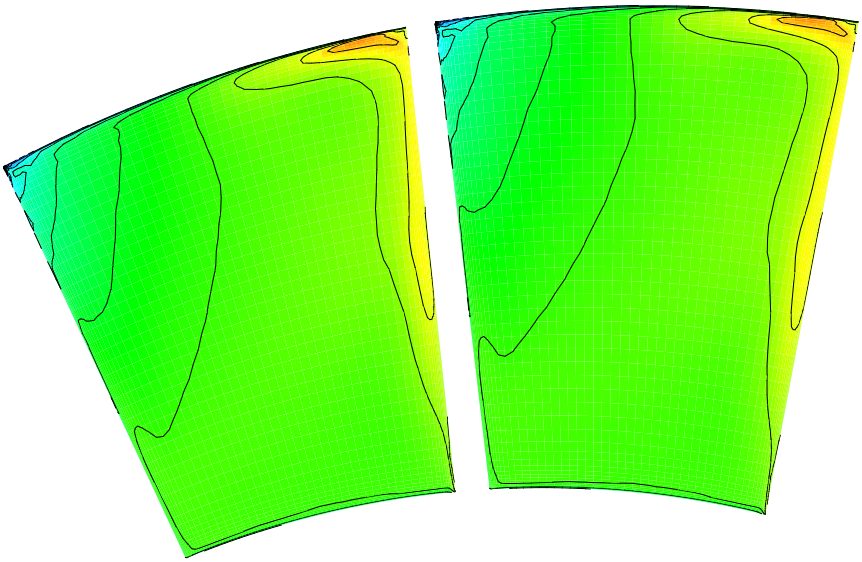

(b)

Figure 6.11: Flow relative Mach number in the meridional plane at 83% blade meridional length (a) with and (b) without tip gap. Operating point: 4 from Table 6.4

the effect of tip leakage loss is stronger near the blade impeller tip. Since the leakage and main flow have different velocities in both magnitude and direction, they create a vortex sheet at their interface which then rolls up into a concentrated vortex as the leakage flow moves downstream along the suction surface-tip endwall corner, as seen in Figure 6.9 [45]. Based on these reasons, for the operating points analyzed in the current work, the local spanwise position for blade boundary layer loss is taken to be about 20 - 25% of the total span (Figure 6.10b).

On the other hand, isolating the tip leakage loss from the CFD simulation is more convoluted than isolating the boundary layer loss. As discussed in Subsection 4.2.2, the entropy generation from the tip leakage loss is mainly due to the mixing of the leakage flow back to the main flow. Unlike in the blade boundary layer loss, there is no clear geometric limit on where to assess the entropy in the blade to isolate the tip leakage loss. Looking at the bigger picture, a simple solution to this problem is to remove the tip gap completely and to compare its impeller efficiency to that of the same impeller with tip gap present, as seen in Figure 6.11. By adopting this method, it is assumed that the presence of tip gap does not affect the other loss mechanism. The efficiency drop induced by the tip leakage is then the efficiency difference between the impeller with the tip gap and the one without the tip gap. The properties (T_t and p_t) are taken from the mass-averaged value

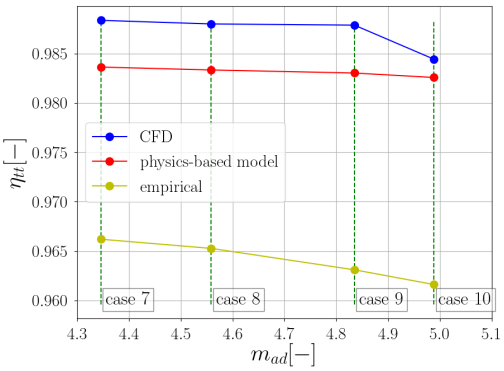

(a) 12 krpm cases, operating points 7, 8, 9 and 10

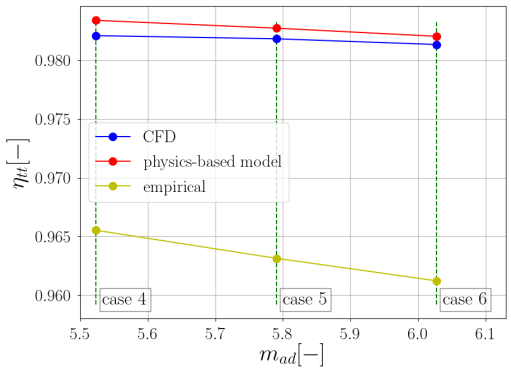

(b) 14 krpm cases, operating points 4, 5 and 6

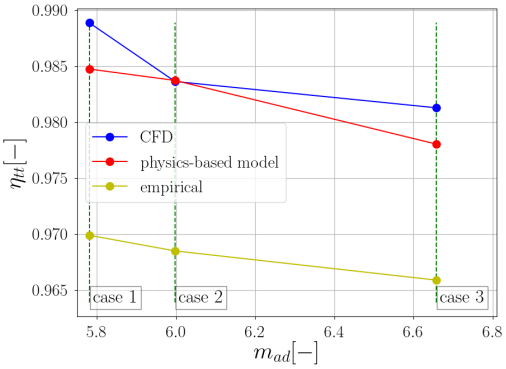

(c) 16 krpm cases, operating points 1, 2 and 3

Figure 6.12: Comparison of efficiency drop induced by blade boundary layer: CFD vs. physics-based loss model vs. empirical correlation, for operating points in Table 6.4

of the whole span, as the tip leakage flow is affecting the flow in the whole blade passage.
To focus the validation only on the result of novel physics-based blade boundary layer and tip leakage loss, the isentropic meanline analysis routine is not used to obtain the velocity triangles and thermodynamic properties. These values are obtained instead from spanwise mass-averaged properties from the CFD simulation. This way, the comparison performed between CFD simulation and the model shows purely the accuracy of the loss model developed in the current work. Additionally, as the baseline, the losses obtained using the empirical losses shown in Table 4.1 are also plotted. The prediction of the empirical skin friction loss model is compared to the one of the novel physics-based blade boundary layer loss, while the empirical clearance model is compared to the tip leakage loss.

6.4. Results Discussion

After the discussion of the CFD settings and model validation strategy, the last section presents the comparison between the results obtained by the CFD simulation, model and empirical correlation. The results are plotted for each rotational speed. The boundary layer loss comparison is shown in Figure 6.12. From Figure 6.12 the key takeaways can be summarized as follows:

- a good trend agreement is reached between boundary layer loss computed with CFD and the physics-based blade boundary layer loss model and the empirical skin friction model
- the absolute values recorded by the empirical skin friction loss model differs from that obtained by the CFD simulations about 3%
- the absolute values recorded by the physical boundary loss model differs from that obtained by the CFD simulations under 1%. This fact means a very good agreement between CFD and the physical loss model has been reached

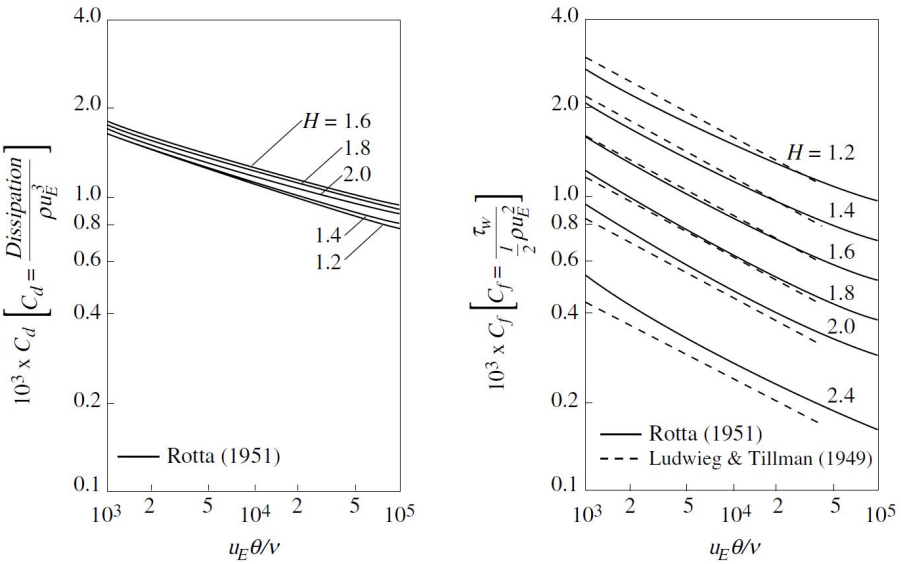

Figure 6.13: Effect of turbulent boundary layer shape factor to C_d and C_f [46]

The comparison between the trend exhibited by the CFD simulation, the physics-based blade boundary layer loss model and the empirical loss models underlines the superiority of the physics-based model. Moreover, the physics-based model is also quite accurate in predicting the blade boundary layer loss.
The physics-based blade boundary layer loss model utilizes the blade boundary layer dissipation coefficient (C_d). As discussed in Subsection 4.2.1 and the findings from [30], the diffusion coefficient, C_d, is only marginally affected by blade boundary layer shape. On the other hand, as shown in the works of Schlichting [46], the Moody friction coefficient (C_f) is highly affected by the turbulent boundary layer shape factor (Figure 6.13).
The empirical model for skin friction loss in Table 4.1 uses the classical Moody skin friction coefficient (C_f), which is based on the fully developed flow in a straight pipe. A fully developed flow far from separation is identical to a thin boundary layer with high shape factor, whereas a higher turbulent boundary layer shape factor (in Figure 6.14 shown as H) corresponds to turbulent boundary layer approaching separation (thick boundary layer) [46]. The thin boundary layer which corresponds to the fully developed flow assumption used in the empirical skin friction correlation causes a high C_f value to be predicted. This overprediction of C_f is the main cause of skin friction loss generation overestimation.
The tip leakage loss comparison is shown in Figure 6.14. The key findings can be listed as follows:

- the trend of efficiency drop obtained by CFD simulation is captured well by both the physics-based and the empirical loss models
- for cases with 14000 and 16000 rpm, the absolute deviation between CFD simulation results and physical tip leakage model is within 1%
- there is a significant discrepancy between the predictions of the physics-based and the empirical loss models as compared to CFD results for the 12000 rpm cases

The problem discussed in the last point may be caused by the choice of C_c (tip gap sudden expansion coefficient). In the current work, the value of C_c is fixed at $C_c = 0.8$. As discussed in Subsection 4.2.2 and in the works of Moore and Tilton [38], a change in rotational speed may change the blade loading and the pressure on the suction side, which is the driving force of the tip leakage flow. Coupling the developed novel physics-based tip leakage loss model with a tip gap discharge coefficient model, such as the model developed by Moore [38], may provide a more accurate tip leakage loss model and remedy this problem, giving an advantage over the empirical clearance loss.

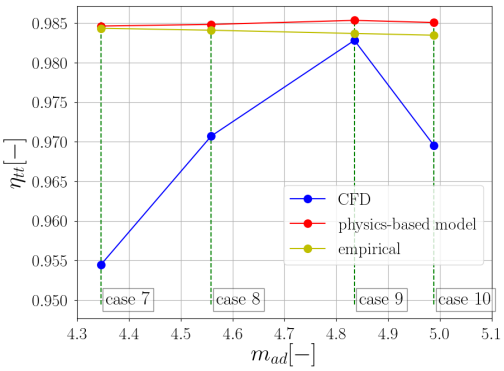

(a) 12 krpm cases, operating points 7, 8, 9 and 10

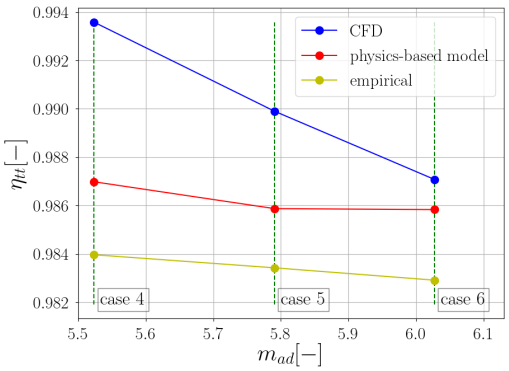

(b) 14 krpm cases, operating points 4, 5 and 6

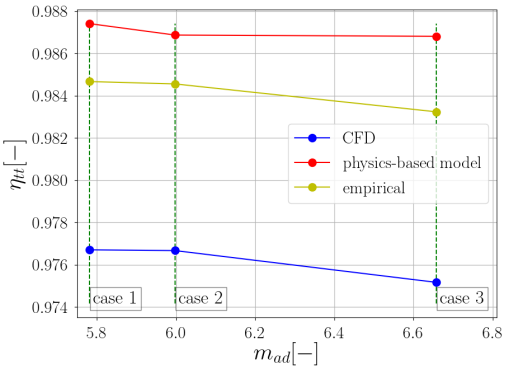

(c) 16 krpm cases, operating points 1, 2 and 3

Figure 6.14: Comparison of efficiency drop induced by tip leakage: CFD vs. physics-based loss model vs. empirical correlation, for operating points in Table 6.4

7

Results for Conventional Centrifugal Compressor

This chapter discusses the results obtained with the developed meanline framework coupled with the physics-based loss model for centrifugal compressors operating with air. First, the test case input and program settings are discussed. Then the computed efficiency trend is compared to the one empirically derived by Casey [11]. Finally, the contribution of each physics-based loss model on the overall compressor performance are analyzed separately. In this analysis, the result predicted by the physics-based loss models and the empirical loss models is also compared over the whole design space.

The benchmarking is mainly performed against the compressor performance map based on Casey's work on centrifugal compressor [11].

7.1. Model Settings and Assumptions

Before being used to assess the performance of non-conventional centrifugal compressors, the result computed by the meanline design program is compared to reference data. The benchmarking process consists of reproducing the compressor design map proposed by Casey, as seen in Figure 4.2, with the proposed preliminary design program. The input parameters used in this benchmarking are listed in Table 7.1.

Some additional assumptions and model setting are listed in Table 7.2. The choice of blade thickness (δ_{bl}) value is based on the work of Oh [10]. Furthermore, the impeller outlet-diffuser inlet width ratio is fixed to one. With this conservative choice, it is implied that the wake mixing loss is only due to wake mixing, instead of due to the sudden expansion at the impeller outlet.

Additional assumptions used in this study are:

- the flow inside the blade passage is assumed to be fully turbulent, eliminating the dependence of η_{tt} to Re
- C_d and C_c are assumed to be constant, with a value of 0.002 and 0.8, respectively
- Z, l_θ and $\frac{D_{1s}}{D_2}$ values are computed by the program's internal routine
- the impeller blades are assumed to be unshrouded for the calculation of the tip leakage loss

Table 7.1: Input parameters used in the original work of Casey [11]

Parameter description	Selected value
Working fluid	Air
Work coefficient (ψ)	0.75
Inlet shape factor (k)	0.9
Outlet radius (r_2)	0.225 m
Inlet absolute angle (α_1)	0^o
Tip gap (g)	0.03

Table 7.2: Additional settings used to reproduce the original Casey's chart

Parameter description	Selected value
Thermodynamic library	RefProp
Blade thickness (δ_{bl})	3 mm
Difusser inlet - impeller outlet width ratio (b^*)	1
Loss model(s)	Physical: boundary layer, tip leakage. Empirical: blade loading, shock trailing edge mixing, recirculation, disk friction
Inlet fluid thermodynamic properties (T_r and p_r)	($T_r = 5$ and $p_r = 0.4$)

- impeller has a parabolic blade shape

7.2. Model Validation

The variation of the compressor stage efficiency over the design space bounded by compression ratio values ranging from 2 to 7, and by flow coefficient ranging from 0.01 to 0.25 is shown in Figure 7.1. The compressor efficiency computed by Casey and the meanline model coupled with the physics-based loss models and empirical loss models are compared in the figure. The key findings from this comparison can be summarized as follows:

- the trend computed by the meanline model coupled with both the physics-based loss models and the empirical loss models is captured correctly. The efficiency maxima occurs around $\phi_{t1} = 0.1$, and shifts

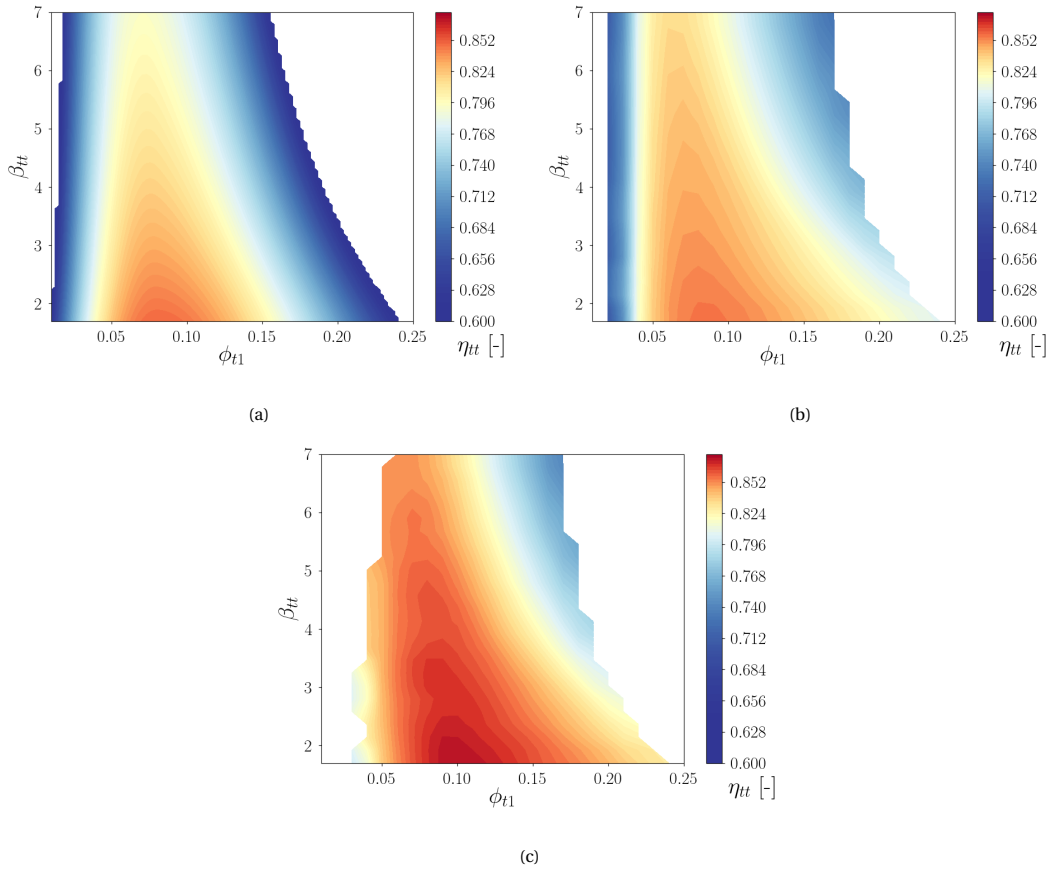

Figure 7.1: Compressor stage efficiencyin the β_{tt}-ϕ_{t1} plane computed with (a) Casey's model (the digitalized version of Figure 4.2), (b) meanline model coupled with the empirical loss models in Table 4.1 and (c) meanline model coupled with the novel physics-based loss models: boundary layer and tip leakage loss replacing empirical skin friction and clearance loss respectively. Impeller geometry and design point as listed in Tables 7.1 and 7.2.

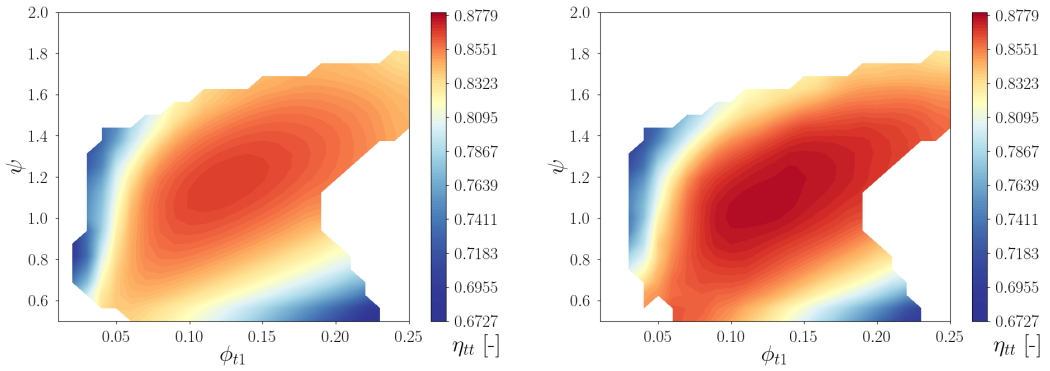

(a) (b)

Figure 7.2: Compressor stage efficiency in the ψ-ϕ_{t1} plane computed with (a) meanline model coupled with the empirical loss models in Table 4.1 and (b) meanline model coupled with the novel physics-based loss models: boundary layer and tip leakage loss replacing empirical skin friction and clearance loss respectively. Impeller geometry and design point as listed in Tables 7.1 and 7.2.

towards lower values of ϕ_{t1} with increasing compression ratio.

- the meanline model, especially coupled with the novel physics-based loss models, predicts larger stage efficiency. This difference is expected as in Casey's method losses inside diffuser is also taken into account. The model developed in the current work only accounts for loss generation mechanisms within the impeller

In design practice, however, the target compression ratio is usually known. The design optimization is, in turn, performed in the ψ-ϕ_{t1} plane. Due to this reason, The results computed with the two different loss models (physics-based and empirical) are also compared in the ψ-ϕ_{t1} plane, as seen in 7.2. For graphical purposes, the comparison is performed at constant compression ratio (β_{tt}) = 2.5. The findings from this comparison are:

- the duty coefficient pair corresponding to the maximum efficiency is around ψ = 1.2 and ϕ_{t1} = 0.12. These values are in agreement with the values mentioned in the optimum efficiency contour for centrifugal compressors based on industrial data of ESDU, as seen in Figure 7.3 [47]
- the stage efficiency computed using the novel physics-based loss models is slightly higher compared to

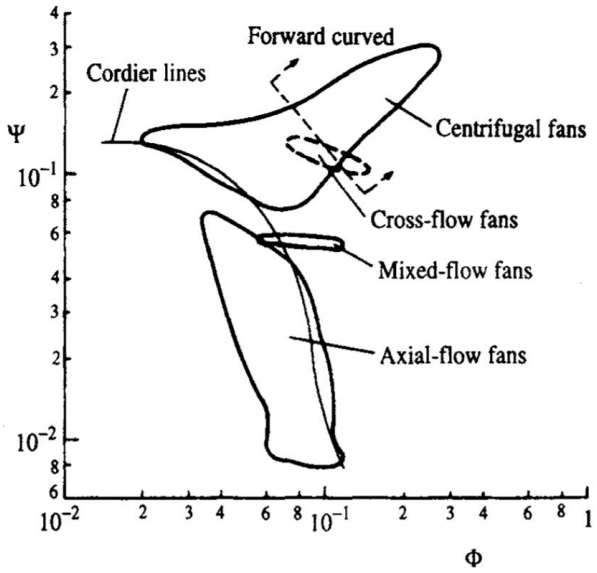

Figure 7.3: Optimum efficiency contours for various types of fan on ψ - ϕ_{t1} plot [47]

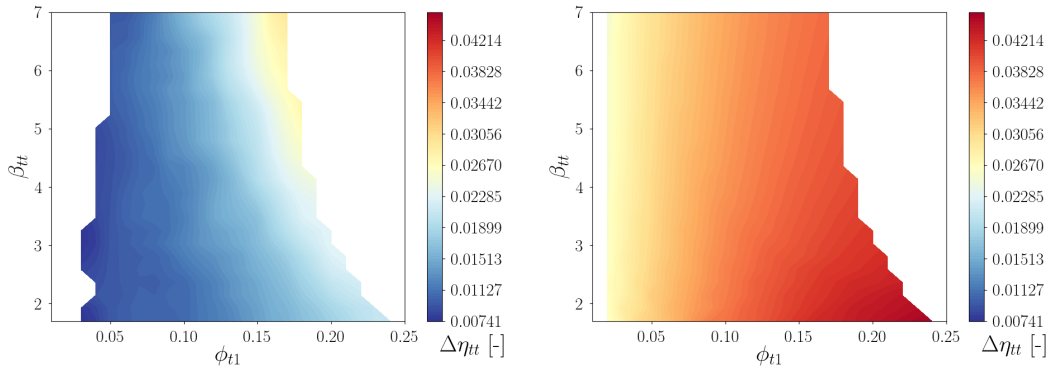

(a) (b)

Figure 7.4: Efficiency drop, $\Delta\eta_{tt}$ computed with (a) physics-based blade boundary layer loss model and (b) empirical skin friction model, in the ϕ-β_{tt} plane

the one predicted by the empirical loss models

The deviation in the prediction of the novel physics-based loss models and the empirical loss models is discussed in the following paragraphs.

7.3. Loss Generation Breakdown

To gain insight into the differences exhibited in the result from the previous comparison, the effect of individual loss sources obtained from the physics-based blade boundary loss and tip leakage loss model is discussed. The comparison is performed against corresponding losses used in the empirical loss models listed in Table 4.1. Blade boundary layer loss is compared with empirical skin friction loss, while the tip leakage loss is compared with empirical clearance loss. The comparison will be done in both the β_{tt}-ϕ_{t1} and the ψ-ϕ_{t1} planes.

7.3.1. Blade Boundary Loss

Figures 7.4 and 7.5 show the efficiency drop calculated with the empirical skin friction model and the physics-based blade boundary layer model. Focusing on the figures, some considerations can be formulated as follows:

- the two loss models exhibit a similar trend of efficiency drop in the ψ-ϕ_{t1} plane, but not in the β_{tt}-ϕ_{t1} plane

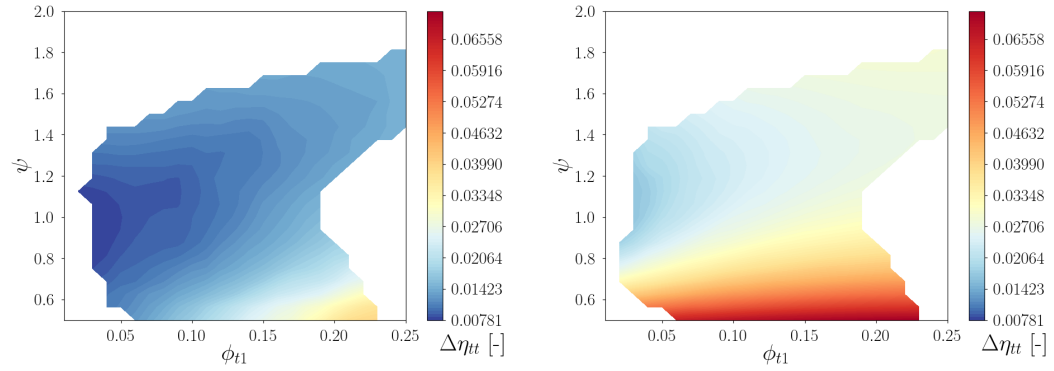

(a) (b)

Figure 7.5: Efficiency drop computed with (a) physics-based blade boundary layer loss model and (b) empirical skin friction model, in the ϕ-ψ plane

- the loss predicted by the physics-based blade boundary layer loss model is lower than that predicted by empirical skin friction model

Understandably, an increase in flow coefficient induces an increase in the blade boundary layer and the skin friction loss, as it corresponds to an increase in flow meridional velocity. Blade boundary layer loss is governed by the cube of velocity, as seen in Equation 4.14:

$$\dot{S} = \int_0^x \frac{\rho_e V_e^3 C_d}{T_e} dx$$

In a physical sense, an increase in velocity causes an increase in the boundary layer mechanical energy dissipation. The difference in the absolute value predicted, on the other hands, perfectly describes the main difference between the two models; the BL model implements dissipation coefficient C_d while skin friction model uses C_f. As discussed back in Section 6.4, C_f is highly affected by the boundary layer shape. The main assumption of the friction coefficient is the flow is a fully developed turbulent flow inside a straight pipe [5]. Due to this assumption, the value of C_f and the resulting entropy generation computed is overestimated (see Figure 6.13).
On the other hand, the trend of efficiency drop induced by the blade boundary layer loss with increasing compression ratio is different compared to that predicted using the empirical skin friction model. In Figure 7.4, the efficiency drop predicted by the empirical skin friction loss model is almost insensitive to the value of β_{tt}, while that computed with the physics-loss model is more sensitive to β_{tt}. Mathematically, this deviation may be explained by the velocity term in the formulation of each model. As seen in Equation 4.14, the entropy generation of each surface induced by the blade boundary layer is governed by the cube of the flow velocity of the respective surface. On the other hand, as seen in Table 4.1, the empirical skin friction loss is formulated as:

$$\Delta h_{t,sf} = 2C_f \frac{l_b}{D_{hyd}} \bar{W}^2$$

where,

$$\bar{w} = \frac{V_{1s} + V_2 + W_{1s} + 2W_{1h} + 3W_2}{8}$$

The empirical skin friction loss uses an average velocity in the formulation, which may lessen the actual effect of change in velocity, and in extension the compression ratio, on the entropy generation.

7.3.2. Tip Leakage loss

Figures 7.6 and 7.7 show the loss generation approximated using the physics-based tip leakage loss model and the empirical clearance model. From both figures, some important findings are:

- the efficiency drop calculated using the physics-based tip leakage loss is more sensitive to the value of β_{tt}, ψ and ϕ_{t1}.

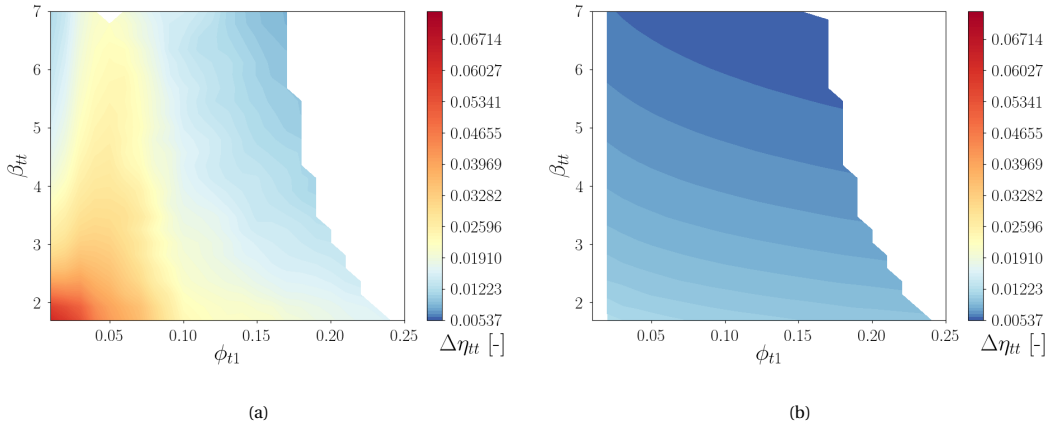

Figure 7.6: Efficiency drop, $\Delta\eta_{tt}$ computed with (a) physics-based tip leakage loss model and (b) empirical clearance model, in the ϕ-β_{tt} plane

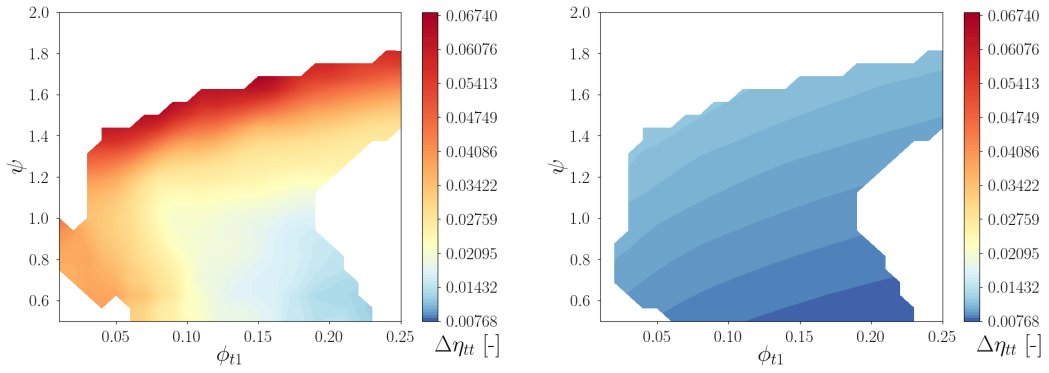

(a) (b)

Figure 7.7: Efficiency drop, $\Delta\eta_{tt}$ computed with (a) physics-based tip leakage loss model and (b) empirical clearance model, in the ϕ-ψ plane

- the efficiency drop values obtained using the physics-based tip leakage loss model is higher than those obtained using the empirical clearance loss model
- both the physics-based model and the empirical model predict maximum loss generation around low values of β_{tt} and ϕ_{t1}, and minimum loss generation at high values of β_{tt} and ϕ_{t1}. Similarly, both models also show an agreement in the maximum and minimum location of loss generation in the ψ-ϕ_{t1} plane (maximum at higher value of ψ and minimum at low value of ψ and high value of ϕ_{t1}).
- the efficiency drop in the optimum design region (ϕ_{t1} = 0.12 and ψ = 1.2) is around 2-3%, which agrees with the result of the work done by Moyle [48], using industrial experimental data.

The absolute value difference from the two models may be due to the choice of C_c. Nevertheless, the trend of both graph is still in agreement with the qualitative prediction of tip leakage loss by Denton: the efficiency drop increases with increased stage loading/work coefficient and with reduced flow coefficient, and vice versa. A possible explanation is that an increase in stage loading causes a high-velocity peak on the blade suction side, increasing the leakage mass flow, and hence, the leakage loss. A reduction in the flow coefficient, on the other hand, implies also a reduction in mass flow rate. Due to the reduction of the mass flow rate, the ratio of the leakage mass flow rate to the main channel mass flow rate is higher in impeller with a lower value of ϕ_{t1}. As the entropy generation due to the tip leakage loss is mainly due to mixing of tip gap flow into the main flow, the increase in this ratio also means an increase in the mixing losses, as seen in Equation 4.37:

$$T\Delta s = \frac{C_c g}{\dot{m}_{main}} \int_0^{l_\theta} W_{ss}^2 \left(1 - \frac{W_{ps}}{W_{ss}}\right) \sqrt{2\rho_{ss}\left(p_{ps} - p_{ss}\right)} ds$$

7.4. Effect of Physics-Based Loss Model on Overall Performance

After investigating the loss generation trend induced by each physics-based loss model developed in the current work, their effect on the overall impeller performance is analyzed. The compressor design map (the β_{tt}-ϕ_{t1} and ψ-ϕ_{t1} graphs) is reconstructed, substituting empirical skin friction and clearance loss models with physics-based blade boundary layer and tip leakage loss models, respectively. Figure 7.8 shows the effect of implementing the physics-based blade boundary layer loss model on the impeller overall performance, while Figure 7.9 shows the effect of implementing the physics-based tip leakage loss model.

The maximum efficiency locus computed with the physics-based loss models, the empirical loss models and Casey's model is then extracted and plotted in both the β_{tt}-ϕ_{t1} and ψ-ϕ_{t1} plane, as seen in Figures 7.10 and 7.11. From these comparisons, several key information can be derived:

- implementing the physics-based blade boundary loss model will cause an overall increase of impeller efficiency. This increase is as expected, due to the overestimation of entropy generation as a consequence of the assumption used within the empirical skin friction loss, as discussed in the previous section.

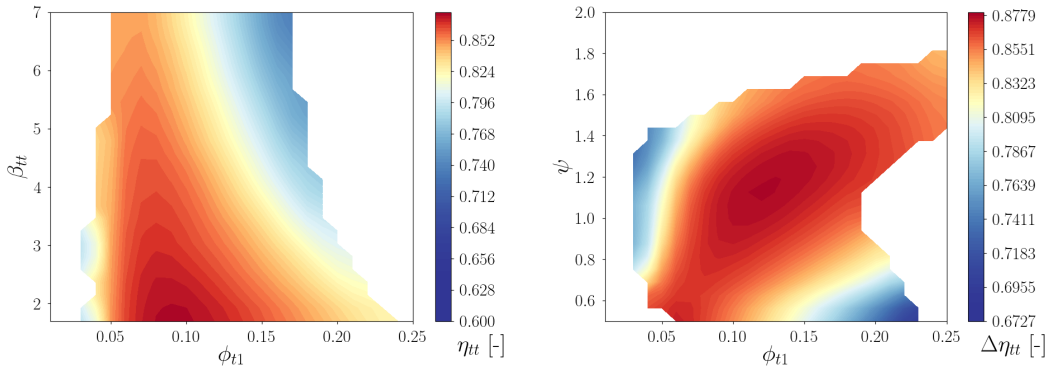

(a) (b)

Figure 7.8: Efficiency contour calculated by substituting empirical skin friction model with physics-based blade boundary layer model plotted in: (a) β_{tt}-ϕ_{t1} plane (b) ψ-ϕ_{t1} plane

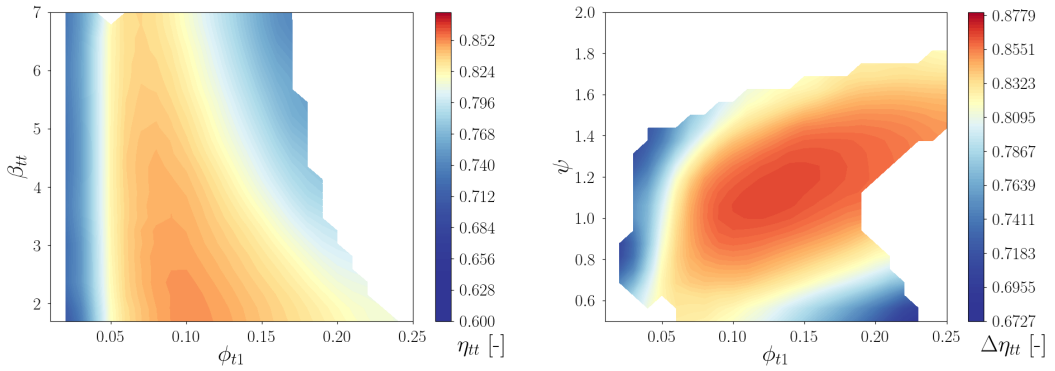

(a) (b)

Figure 7.9: Efficiency contour calculated by substituting empirical clearance model with physics-based tip leakage model plotted in: (a) β_{tt}-ϕ_{t1} plane (b) ψ-ϕ_{t1} plane

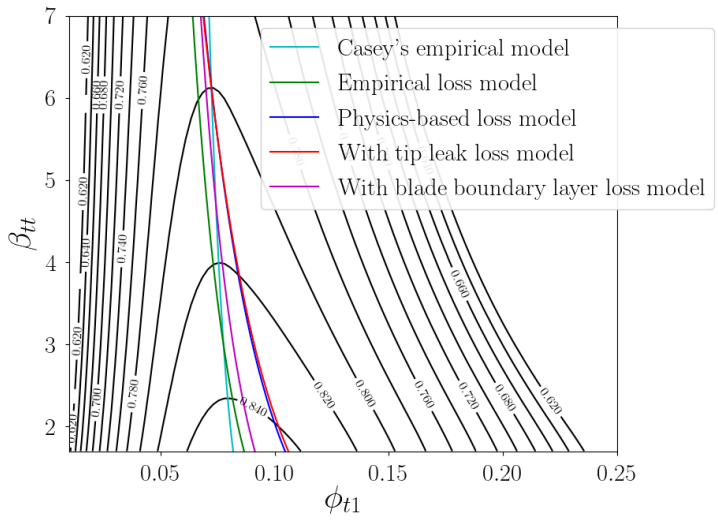

Figure 7.10: Maximum efficiency locus in the β_{tt}-ϕ_{t1} plane computed using physics-based loss models, compared with the result of the empirical loss models and Casey's model

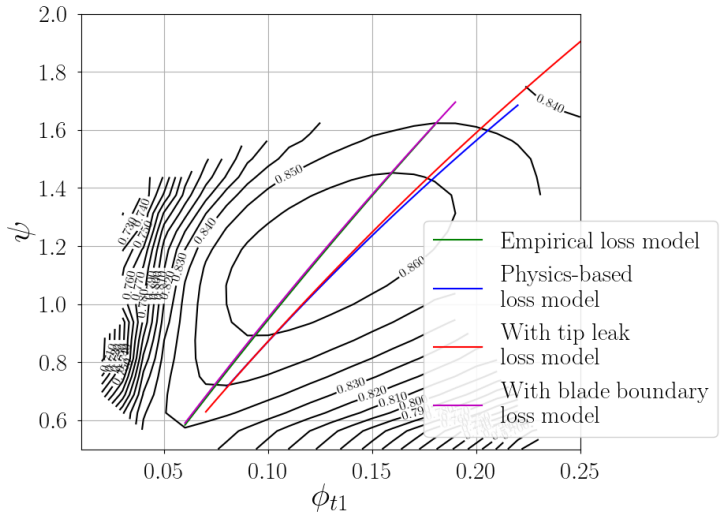

Figure 7.11: Maximum efficiency locus in the ψ-ϕ_{t1} plane computed using the physics-based loss models, compared with the result of the empirical loss models

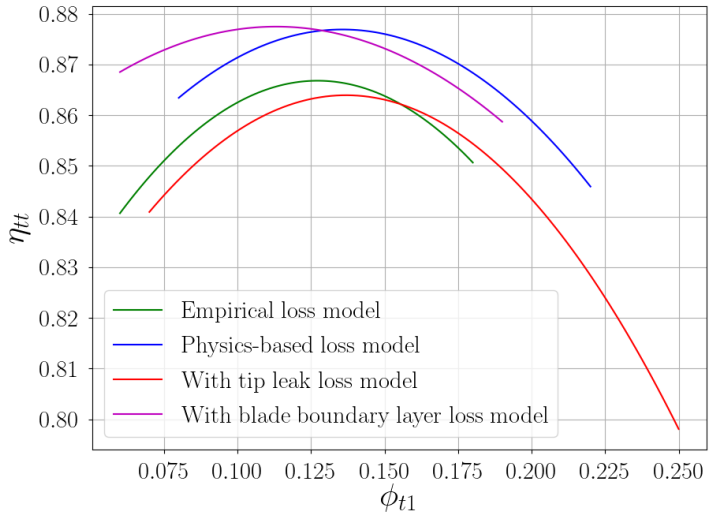

Figure 7.12: Efficiency values along the maximum efficiency locus lines in Figure 7.11

- the efficiency maxima locus calculated implementing the physics-based loss model shifts toward higher value of flow coefficient, compared to that obtained using full empirical loss models.
- The shift of the locus of maximum efficiency is caused mainly by the physics-based tip leakage loss model. This shift may be caused by the fixing of C_c value. Further improvement to the tip leakage model may be performed by implementing a simple model for C_c calculation inside the physics-based tip leakage loss calculation routine, such as the model developed by Moore [38].

8

Model Result for Unconventional Centrifugal Compressors

In this chapter, the effect of changes in fluid parameters, namely molecular complexity and thermodynamic conditions and compression ratio, on the efficiency drop induced by each loss generation mechanism is discussed. The emphasis on the analysis is on the novel physics-based blade boundary layer and tip leakage loss. The effect of these changes on the two physics-based loss model is examined. Additionally, the impact of flow non-ideality on the achievable efficiency and the shift of the optimum design region is analyzed. The input parameters used in this analysis are listed in Table 8.1.

8.1. Effect of Molecular Complexity

The molecular complexity of a fluid (N) is defined as the number of active degree of freedom of the molecule [49]. N is formulated as:

$$N = \frac{2\, MolarMass\, c_{v,ideal}}{R} \tag{8.1}$$

To analyze the effect of working fluid molecular complexity on centrifugal compressor performance, four different working fluids are used in conjunction with the other input parameters seen in Table 8.1. These working fluids are chosen due to their relevance in industrial applications:

- Air is the conventional working fluid for turbomachinery applications. As such, this fluid is taken as the benchmark for the following analysis.
- supercritical CO_2 is now being studied intensively as a candidate working fluid for closed Brayton cycles for power generation [50]. The usage of supercritical CO_2 is an attractive option to achieve high energy conversion efficiency at moderate maximum cycle temperature.
- refrigerant R134a is the standard working fluid used for domestic and small scale refrigeration and vapour compression systems.
- Hexamethyldisiloxane is a theoretical upper-limit case for the following analysis. It represents the most complex molecule considered in this work

Table 8.1: Input parameters used in the performance analysis of non-conventional centrifugal compressor

Parameter description	**Selected value**
Compression ratio (β_{tt})	2.5
Inlet shape factor (k)	0.9
Outlet radius (r_2)	0.225 m
Inlet absolute angle (α_1)	0^o
Tip gap (g)	0.03

Table 8.2: Physical characteristics of the chosen working fluids [49]

Fluid	Chemical Formula	Molar Mass [g/mol]	N [-]
air	N_2 (78.12%) + O_2 (20.96%) + Ar (0.92%) +	28.97	4.98
Carbon dioxide	CO_2	44.01	7
R134a	CH_2FCF_3	102.0	21.6
Hexamethyldisiloxane	$C_8H_18OSi_2$	162.4	77.4

Table 8.3: Reduced inlet thermodynamic conditions selected to investigate the impact of molecular complexity on centrifugal compressor performance

Working fluid	Reduced inlet thermodynamic properties	
	$\mathbf{T}_r$	$\mathbf{p}_r$
Air	0.4	5.0
CO_2	3.0	1.0
R134a	0.5	1.5
Hexamethyldisiloxane	0.25	1.4

The characteristics of these fluids are shown in Table 8.2. In this section, only the effect of molecular complexity is analysed. To ensure that the flow non-ideality effect is negligible in the present analysis, the reduced inlet conditions are selected so that all the thermodynamic transformations fall within the dilute gas region, i.e. the region where Z is close to 1 and γ_{pv} is close to γ_{ideal}, see Table 8.3 and Figure 8.1. The comparisons are performed at several values of β_{tt}. However, for the sake of brevity, only the comparison at β_{tt} = 2.5 is reported. The result of the analysis performed at other values of β_{tt} is shown on Appendix A.

The effect of fluid molecular complexity on the blade boundary layer loss and clearance loss is shown in Figures 8.2 and 8.3. The figures show the deviation of the efficiency drop induced by each loss source mechanism with respect to the one computed using air as the working fluid. From the figures, there are some key takeaways to be noted:

- There is no noticeable shift in the trend of the blade boundary layer loss due to the change in molecular complexity

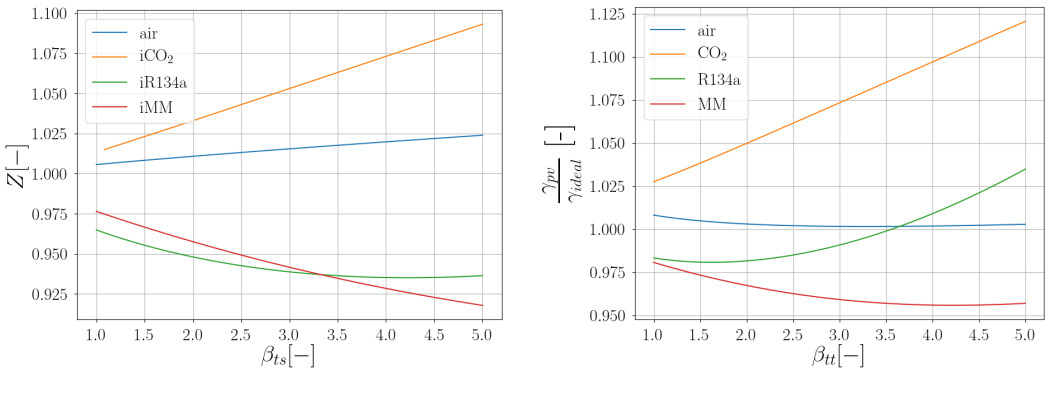

(a) (b)

Figure 8.1: Effect of compression ratio to fluid non-ideality in terms of Z and Γ along the compression for working fluid with reduced inlet thermodynamic properties listed on Table 8.3

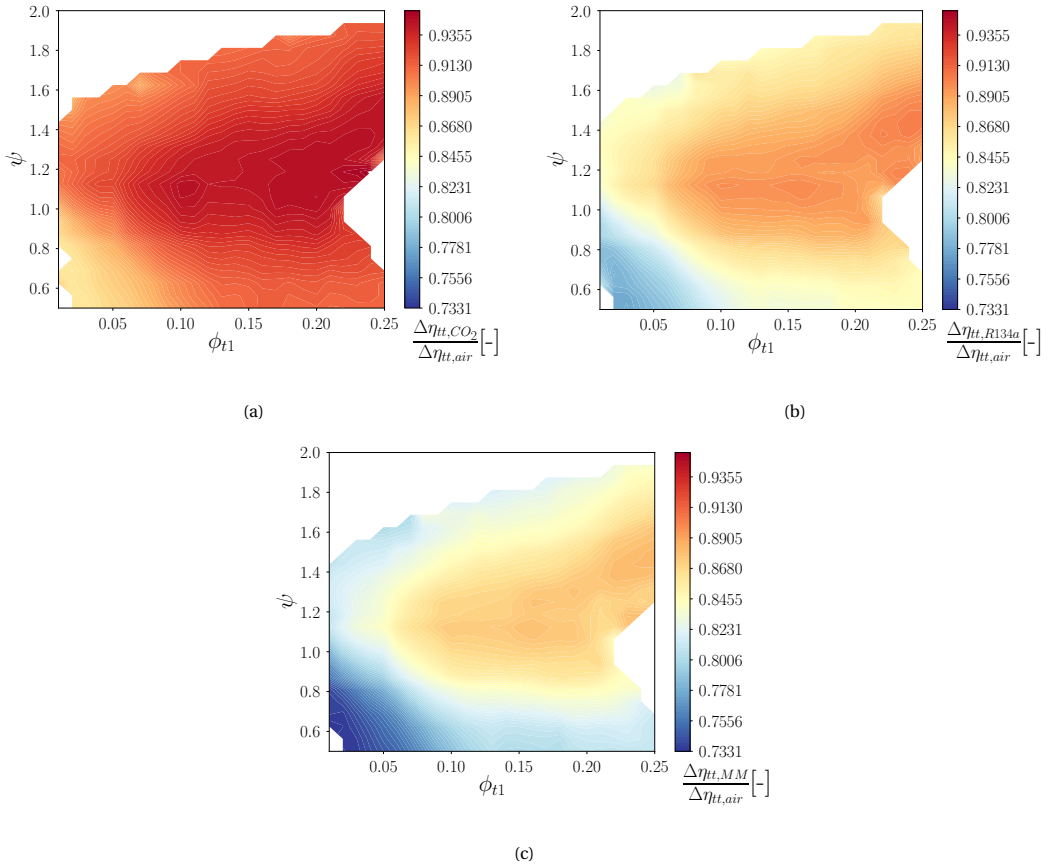

Figure 8.2: Effect of fluid molecular complexity on blade boundary layer loss; $\Delta\eta_{tt,BL}$ for: (a) CO_2 (b) R134a and (c) MM, normalized with $\Delta\eta_{tt,BL}$ of air

- A more complex molecule yields a smaller efficiency drop induced by blade boundary layer loss
- when increasing fluid molecular complexity, the value of $\Delta\eta_{tt,tipleakage}$ becomes more sensitive to the value of ψ
- An increase in molecular complexity generally decreases the efficiency drop induced by tip leakage.

As shown in Figure 8.4, the blade surface velocity at the same value of ϕ_{t1} and ψ generally decreases with increasing fluid molecular complexity. The more complex a fluid is, the higher the fluid density. This fact results in lower isentropic inlet-outlet total enthalpy difference $(h_{t2s} - h_{t1})$ with increasing fluid molecular complexity; the denser the gas, the less work is needed to compress the gas to reach similar compression ratio. Recalling Equation 4.14, entropy generation due to blade boundary loss is especially dependent on the blade surface velocity (V_e), as the entropy generation is related to the cube of the velocity. The decrease in surface velocity, in turn, decreases the boundary layer entropy generation.
The decrease in the entropy generation induced by tip leakage is also mainly caused by the variation on blade surface velocity with fluid molecular complexity. Recalling Equation 4.37, the tip leakage entropy generation is proportional to the square of the suction side blade surface velocity (w_{ss}) and the difference between the pressure and suction blade surface velocity$\left(1 - \frac{w_{ps}}{w_{ss}}\right)$. As seen in Figure 8.4, increasing the fluid molecular complexity decreases both the w_{ss} and the velocity difference between both blade surface. causing lower entropy generation. However, due to the dependence of the square of the suction side velocity, the fluid molecular complexity effect on entropy generation induced by tip leakage is less pronounced compared to that induced by boundary layer, which is a function of the cube of blade surface velocity.
Furthermore, the effect of molecular complexity on overall impeller performance is shown in Figure 8.5. The following key points can be highlighted:

- the fluid molecular complexity does not modify the optima design region, i.e the optimal efficiency

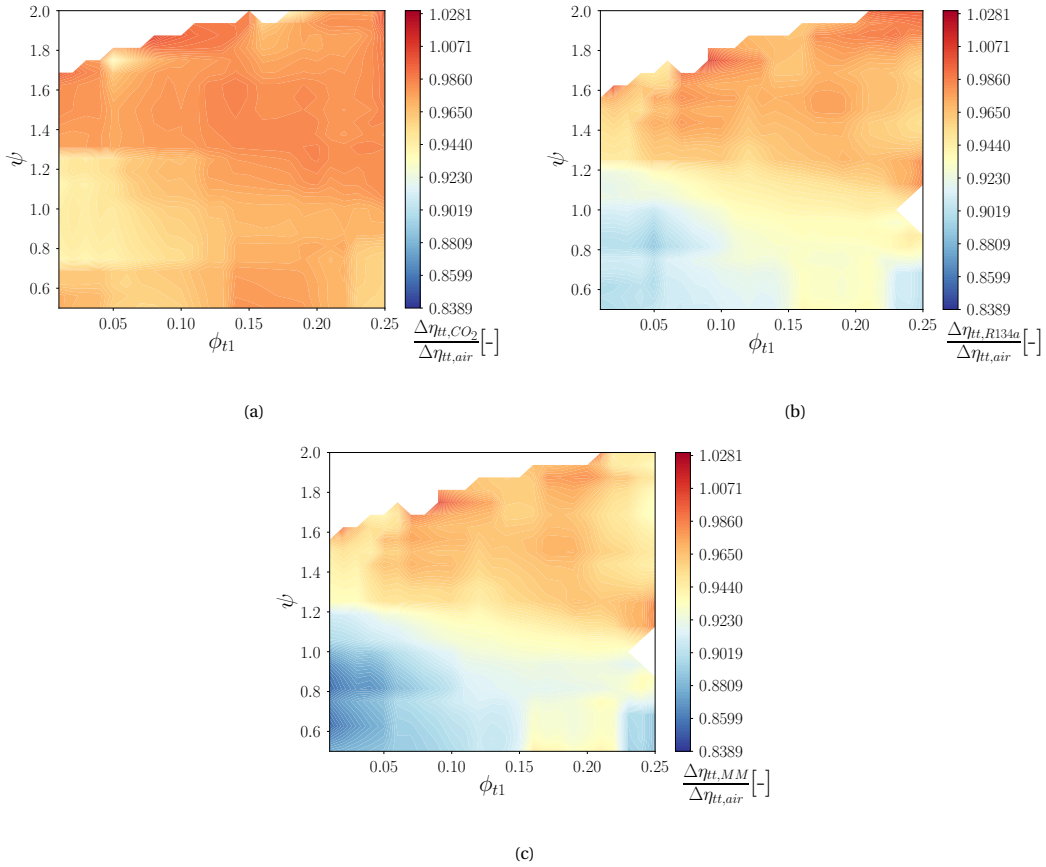

Figure 8.3: Effect of fluid molecular complexity on tip leakage loss; $\Delta\eta_{tt,tipleakage}$ of: (a) CO_2 (b) R134a and (c) MM, normalized with $\Delta\eta_{tt,tipleakage}$ of air

locus in the ψ-ϕ_{t1} plane.

- higher molecular complexity tends to decrease the total entropy generation in the impellers, leading to a higher absolute value of η_{tt}

In Figure 8.5a, the maximum efficiency locus is almost superimposed on top of the others. This insensitivity

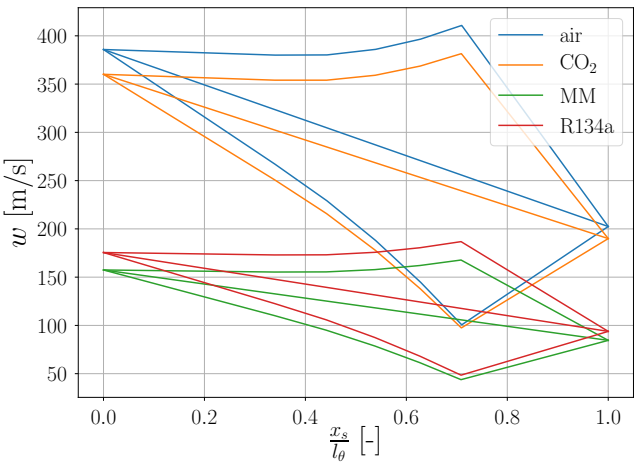

Figure 8.4: Effect of molecular complexity on blade surface velocity distribution, at: ϕ_{t1} = 0.16, ψ = 1.0

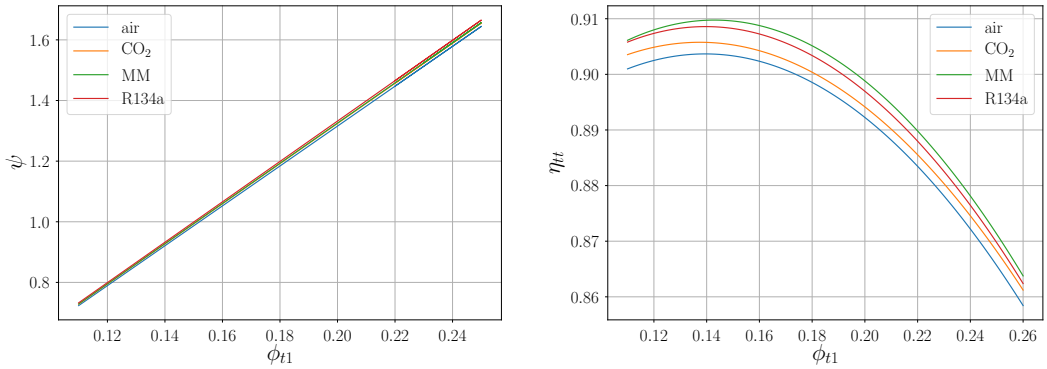

(a) (b)

Figure 8.5: Variation of the (a) optimum efficiency locus and (b) maximum achievable efficiency at $\beta_{tt} = 2.5$ for centrifugal impellers operating with fluids listed in Table 8.3

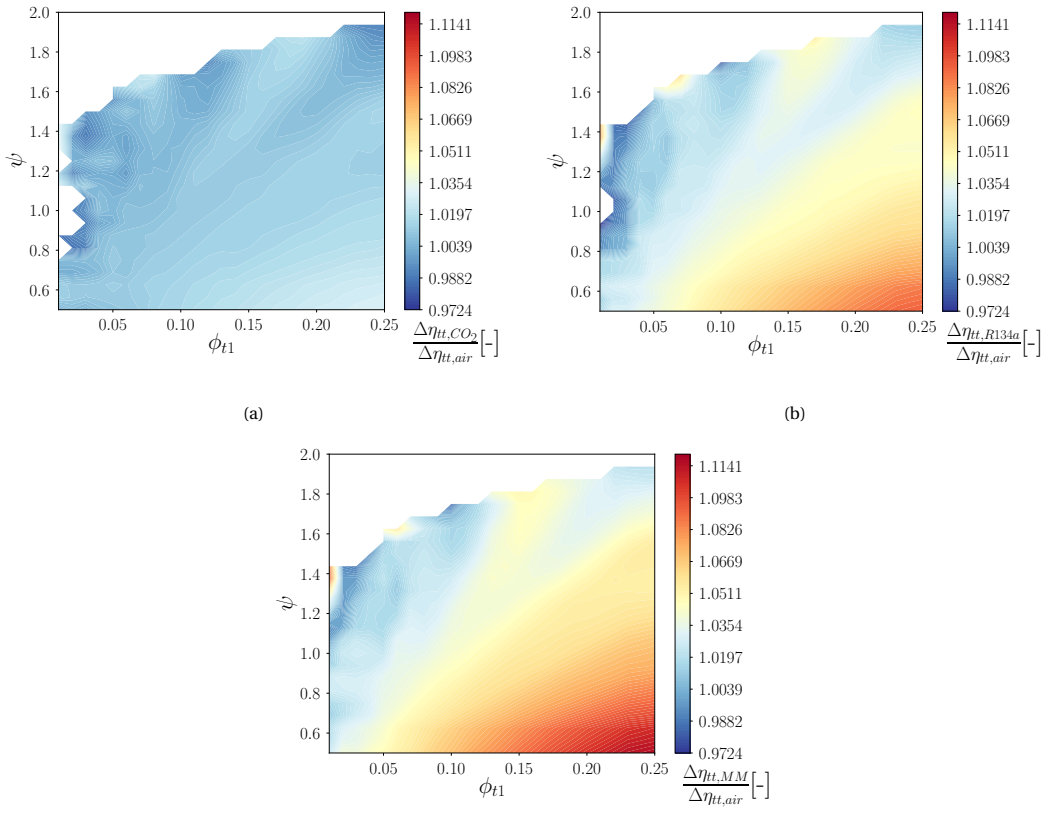

(a) (b)

(c)

Figure 8.6: Effect of fluid molecular complexity on mixing loss; $\Delta\eta_{tt,mixing}$ of: (a) CO_2 (b) R134a and (c) MM, normalized with $\Delta\eta_{tt,mixing}$ of air, loss calculated using empirical relation in Table 4.1

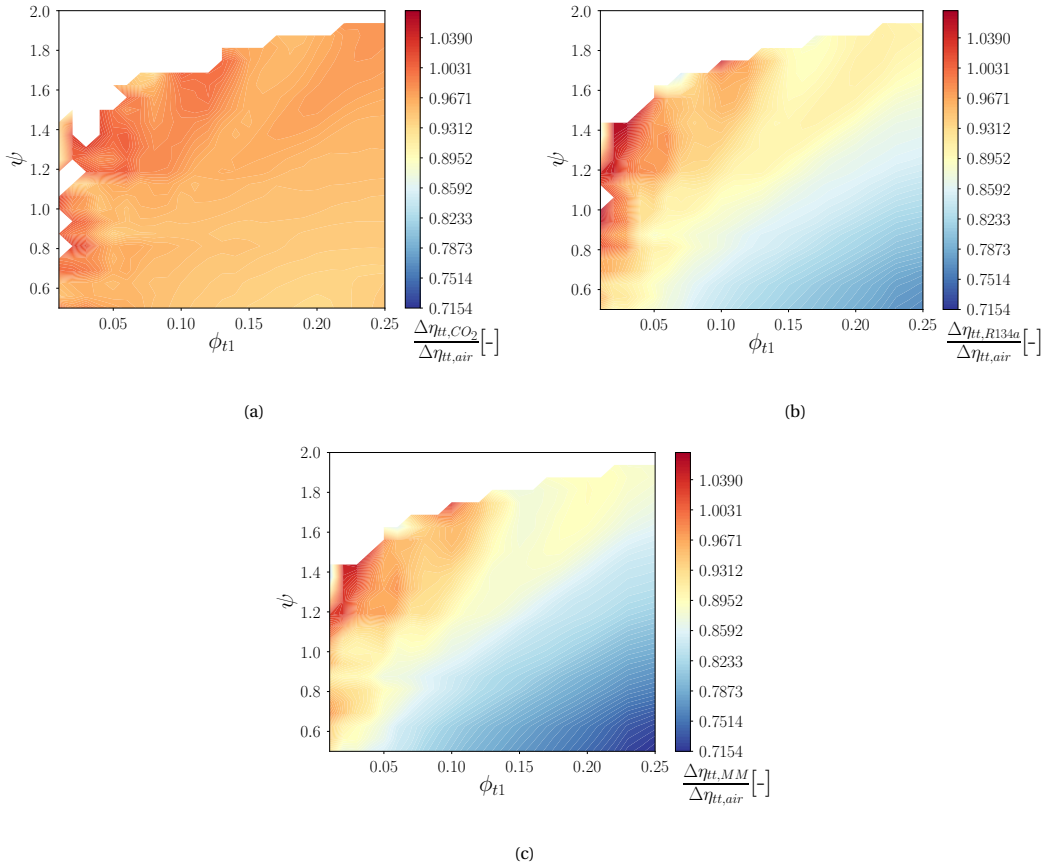

Figure 8.7: Effect of fluid molecular complexity on recirculation (secondary flow) loss; $\Delta\eta_{tt,recirculation}$ of: (a) CO_2 (b) R134a and (c) MM, normalized with $\Delta\eta_{tt,recirculation}$ of air, loss calculated using empirical relation in Table 4.1

is due to the current work only focusing on two loss generation mechanisms: blade boundary layer loss and tip leakage loss. Based on the loss breakdown shown in Figure 4.5, they only cover two out of the overall loss generation mechanisms. In the current work, the loss induced by other loss generation mechanisms is computed by means of empirical correlations. As seen in Figures 8.6 and 8.7, it can be seen that the effect of fluid molecular complexity on the wake mixing and secondary flow loss generation is not negligible, even when predicted using empirical formulations. Moreover, in a previous work by Howell [51], it is shown that for an axial compressor, secondary flow losses account for as much as 2/3 of the total loss. In a centrifugal compressor, the secondary flow loss is as important, if not more, due to the axial-radial bend induces strong flow convecting the blade surface boundary layers toward the casing [30]. Additionally, the jet-wake phenomena in the discharge of centrifugal impellers also underlines the importance of wake mixing loss in overall impeller performance [27] [28]. By modelling the mixing and secondary flow entropy generation mechanisms with physics-based loss models, the current maximum efficiency locus insensitivity may be remedied.

8.2. Effect of Flow Non-Ideality

In this section, the effect of flow non-ideality on impeller performance is analyzed. In this analysis, CO_2 and R134a are used as working fluid, while the compression ratio is fixed at $\beta = 2.5$. To capture the effect of flow non-ideality, the reduced inlet conditions are progressively shifted towards the critical point, as seen in Figure 8.8, and listed in Table 8.4. The effect of the reduced inlet conditions of the cases listed in Table 8.4 on the flow compressibility factor along the compression process is exhibited in Figure 8.9. As expected, the ideal cases (indicated by the letter "i" in the labels) have a value of Z around 1 , whereas the non-ideal cases (labels "ni") are characterized with decreasing value of Z as the inlet conditions are shifted closer towards the critical point.

Figures 8.10-8.13 shows the effect of flow non-ideality on the efficiency drop induced by blade boundary layer and tip leakage. From the figures several key findings can be listed:

Table 8.4: Reduced inlet conditions used to investigate NICFD effect

Fluid	**Case name**	Inlet reduced properties	
		p_r	T_r
CO_2	iCO_2	1.0	3.0
	$niCO_{2,1}$	2.0	1.54
	$niCO_{2,2}$	2.0	1.34
	$niCO_{2,3}$	2.0	1.14
R134a	iR134a	0.5	1.5
	$niR134a_1$	1.5	1.3
	$niR134a_2$	1.5	1.2
	$niR134a_3$	1.5	1.1

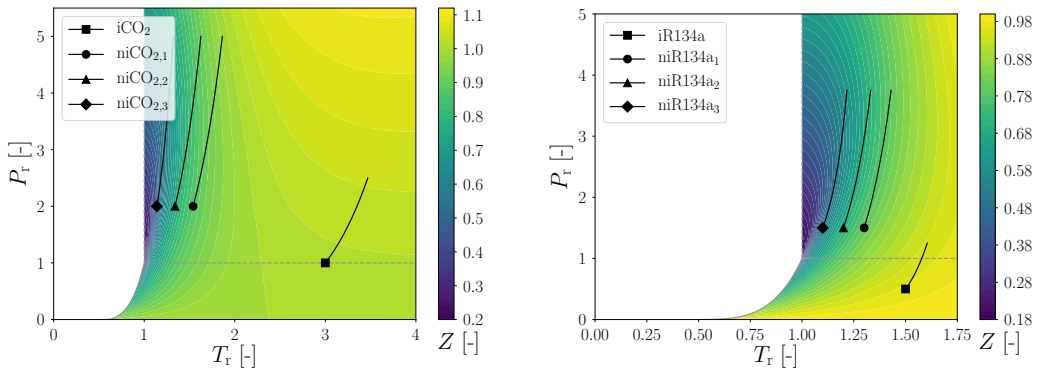

(a) (b)

Figure 8.8: Compressibility factor of (a) CO_2 and (b) R134a. β_{tt} = 2.5. The reduced inlet conditions are listed in Table 8.4

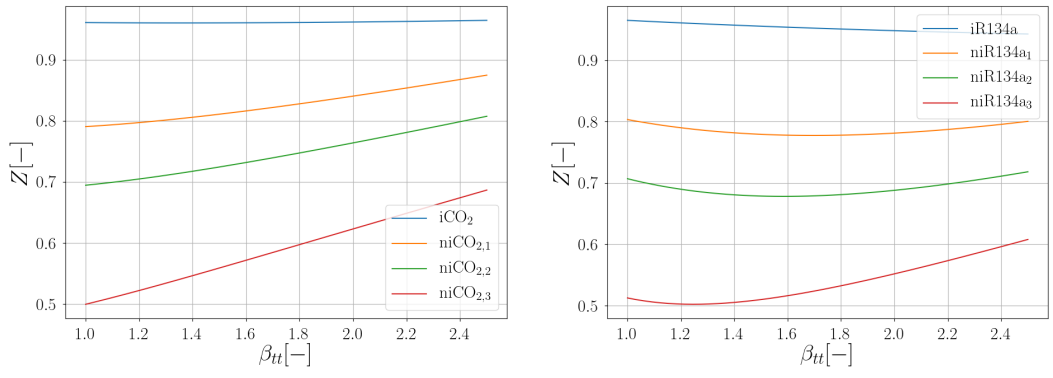

(a) (b)

Figure 8.9: Compressibility factor along the isentropic compression processes shown at Figure 8.8 of (a) CO_2 and (b) R134a. Reduced inlet condition are listed in Table 8.4

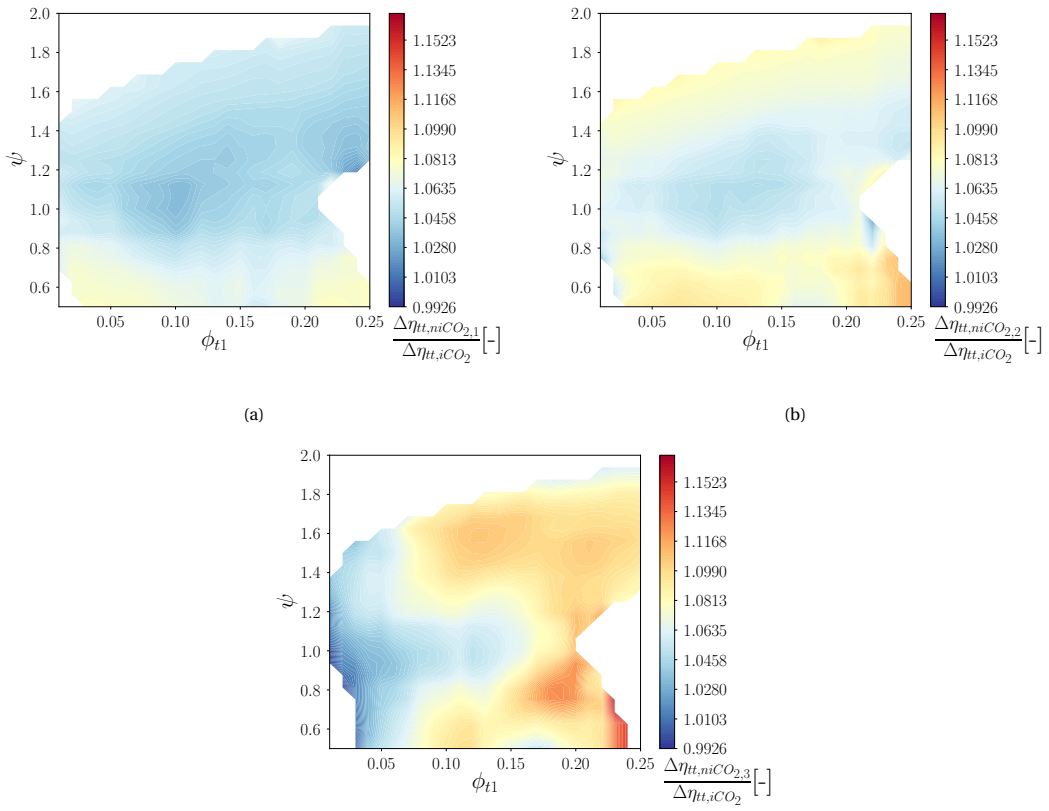

Figure 8.10: Efficiency drop induced by blade boundary layer with CO_2 as the working fluid for case: (a) $niCO_{2,1}$, (b) $niCO_{2,2}$ and (c) $niCO_{2,3}$. β_{tt} = 2.5. The value is normalized with $\Delta\eta_{tt,BL}$ of CO_2 case: iCO_2. The reduced inlet thermodynamic properties are listed in Table 8.4

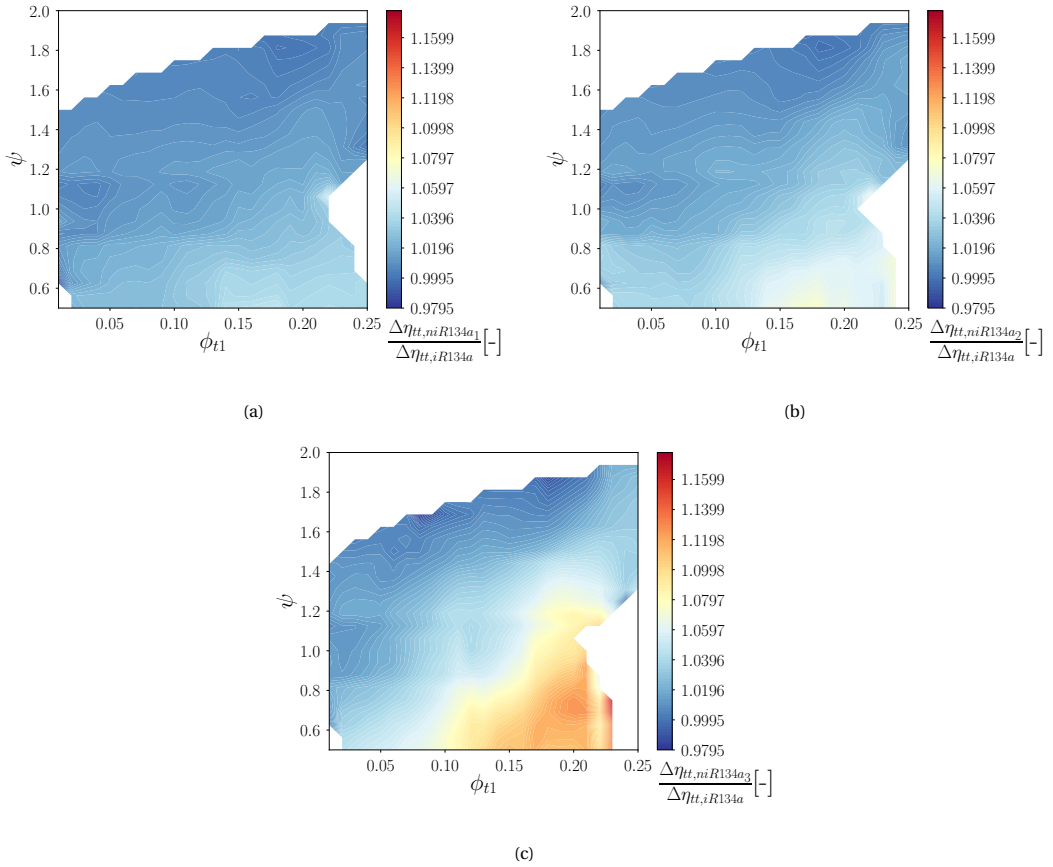

Figure 8.11: Efficiency drop induced by blade boundary layer with R134a as the working fluid for case: (a) niR134a$_1$, (b) niR134a$_2$ and (c) niR134a$_3$. β_{tt} = 2.5. The value is normalized with $\Delta\eta_{tt,BL}$ of R134a case: iR134a. The reduced inlet thermodynamic properties are listed in Table 8.4

- flow non-ideality causes the efficiency drop induced by blade boundary layer and tip leakage loss to be more sensitive to the change of ψ and ϕ_{t1}
- decreasing Z generally increases the efficiency drop induced by both blade boundary layer and tip leakage loss
- the effect of flow non-ideality on both blade boundary layer and tip leakage loss is more prominent for the simpler working fluid, at comparable values of Z
- flow non-ideality leads to an increase in entropy generation induced by blade boundary layer at high value of ϕ_{t1}, and in entropy generation induced by tip leakage at low values of ϕ_{t1}

In the presence of flow non-ideality, the efficiency drop induced by both blade boundary layer and tip leakage is increased. Looking at the blade surface distribution, as seen in Figure 8.14, the lower blade surface velocities suggest lower loss is generated in the presence of flow non-ideality, which is the opposite of the observed trend. Nevertheless, looking back at the governing equation of entropy generation due to blade boundary layer and tip leakage (Equations 4.14 and 4.37), which read:

$$\dot{S} = \int_0^x \frac{\rho_e V_e^3 C_d}{T_e} dx$$

and

$$T\Delta s = \frac{C_c g}{\dot{m}_{main}} \int_0^{l_\theta} W_{ss}^2 \left(1 - \frac{W_{ps}}{W_{ss}}\right) \sqrt{2\rho_{ss}\left(p_{ps} - p_{ss}\right)} ds$$

, the entropy generation is also dependent on the flow density (ρ). In fact, as seen in Figure 8.15, the increase in density trumps the effect of blade surface velocity decrease. This high dependence on flow density causes

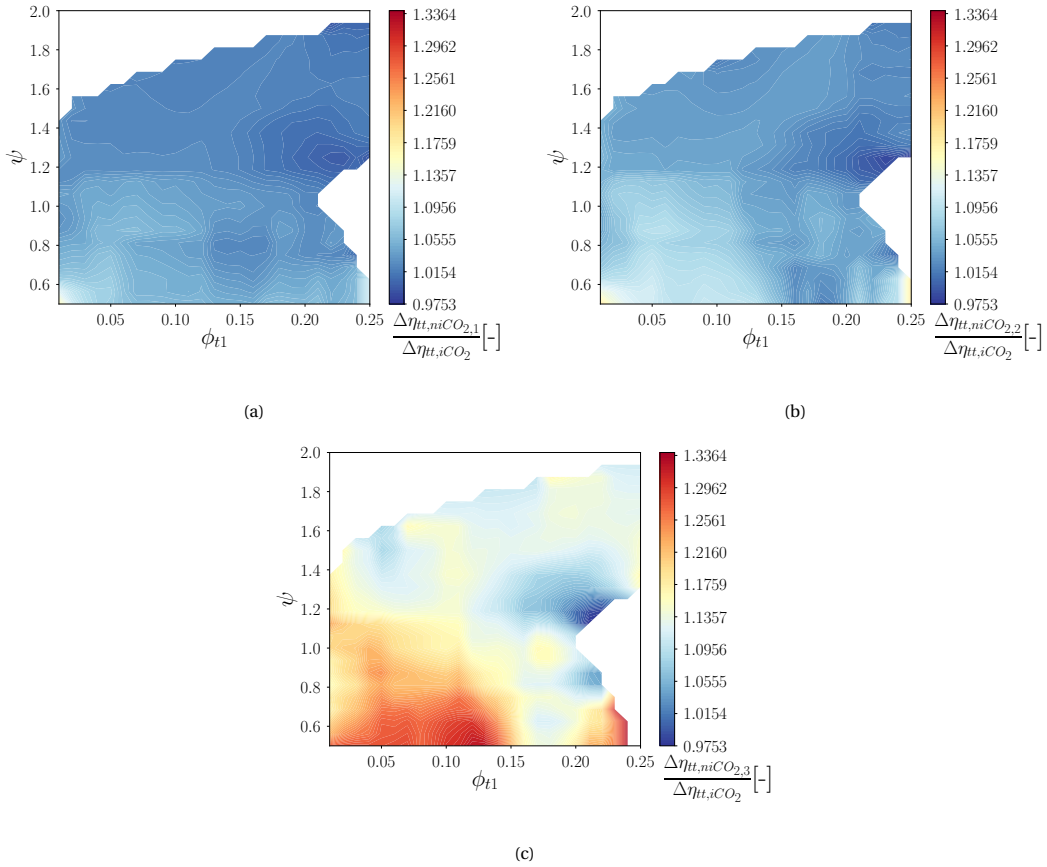

Figure 8.12: Efficiency drop induced by tip leakage with CO_2 as the working fluid for case: (a) niCO2,12, (b) $niCO_{2,2}$ and (c) $niCO_{2,3}$. β_{tt} = 2.5. The value is normalized with $\Delta\eta_{tt,tipleakage}$ of CO_2 case: iCO_2. The reduced inlet thermodynamic properties are listed in Table 8.4

the increase in efficiency drop in the presence of flow non-ideality.
Another interesting finding is the increase in efficiency drop induced by blade boundary layer loss with fluid non-ideality. From Figure 8.15, it is clear that the high density due to flow non-ideality causes an increase in entropy generation. Nevertheless, this effect is diminished by the overall lower flow velocity at lower value of ϕ_{t1}, as the entropy generation induced by blade boundary layer is governed by the cube of the blade surface velocity.
On the other hand, the presence of flow non-ideality also causes an increase in loss generation due to tip leakage loss at low value of ϕ_{t1}. The driving force of the tip leakage loss is the pressure difference between the pressure and suction surface, and the pressure is dependent on the density of the fluid. Referring to Figure 8.15, in the presence of flow non-ideality, the fluid density deviates greatly from the ideal case, implying a high pressure in the non-ideal case. Indeed, as shown in Figure 8.16, the presence of flow non-ideality causes a significant increase of the difference between p_{ps} and p_{ss} along the flow length (l_θ).
The effect of flow non-ideality on the impeller optimum design locus can be seen in 8.17. The most relevant findings can be summarized as follows:

- there is a slight shift of the optimum design locus towards lower values of ϕ_{t1} in cases with high flow non-ideality
- flow non-ideality decreases the maximum obtainable efficiency of the impeller
- the effect of flow non-ideality on the value of maximum efficiency is more prominent in fluids characterized by lower molecular complexity.

The more noticeable drop on maximum efficiency for CO_2 correctly mirrors the trend observed in the blade boundary layer and tip leakage loss generation. The implementation of physics-based loss model for other

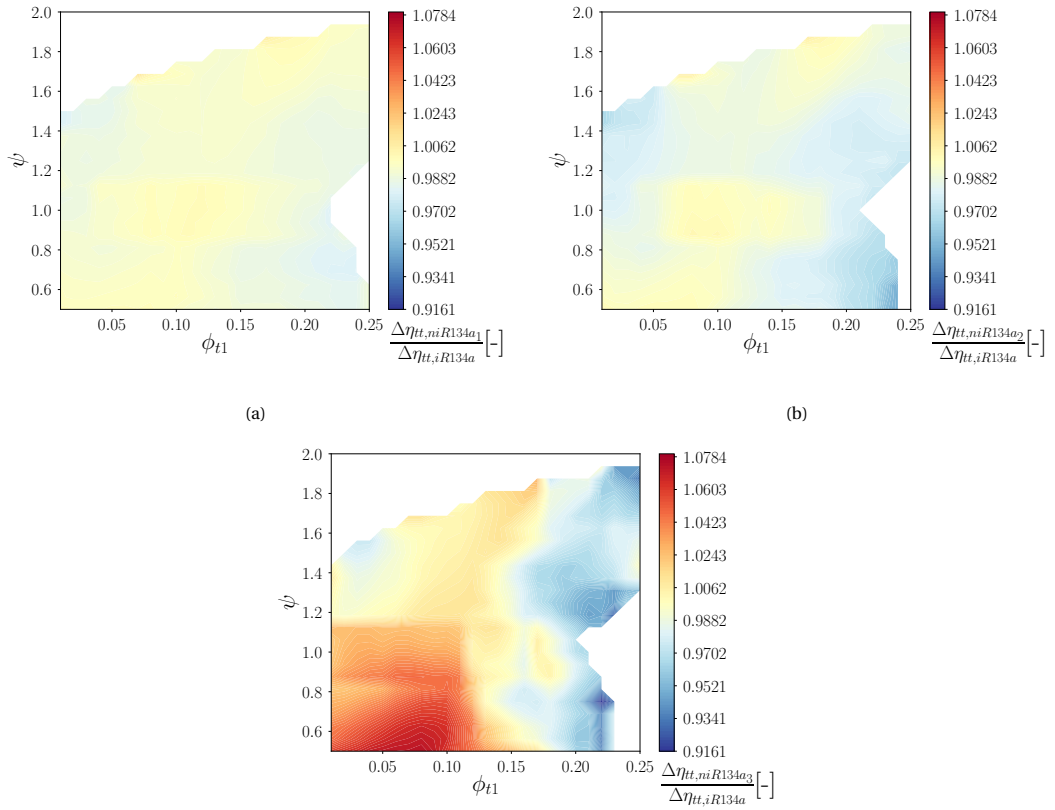

(a) (b)

(c)

Figure 8.13: Efficiency drop induced by tip leakage with R134a as the working fluid for case: (a) niR134a$_1$, (b) niR134a$_2$ and (c) niR134a$_3$. β_{tt} = 2.5. The value is normalized with $\Delta\eta_{tt,tipleakage}$ of R134a case: iR134a. The reduced inlet thermodynamic properties are listed in Table 8.4

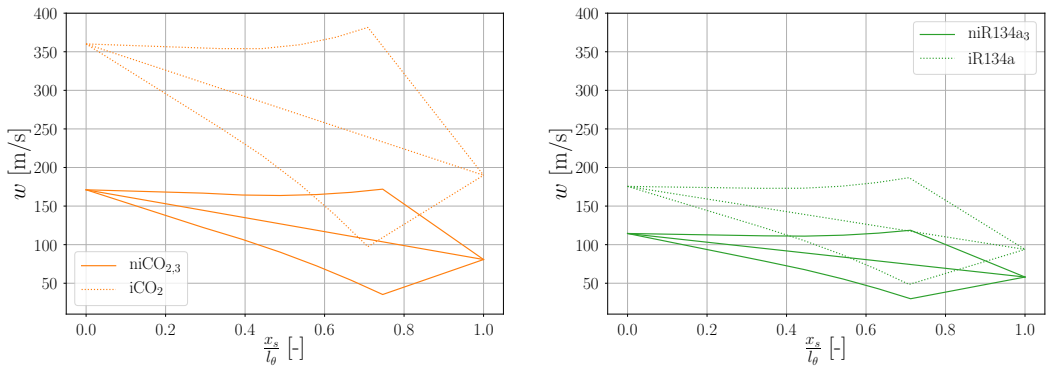

(a) (b)

Figure 8.14: Effect of flow non-ideality on blade surface velocity distribution, at ϕ_{t1} = 0.16 and ψ = 1.0 for (a) CO_2 and (b) R134a

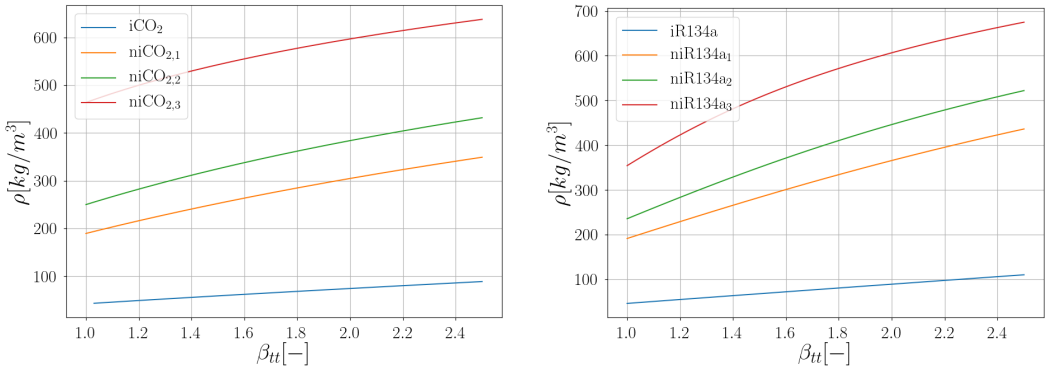

(a) (b)

Figure 8.15: Fluid density along isentropic compression of (a) CO_2 and (b) R134a. β_{tt} = 2.5. The reduced inlet thermodynamic properties values are as shown in Table 8.4

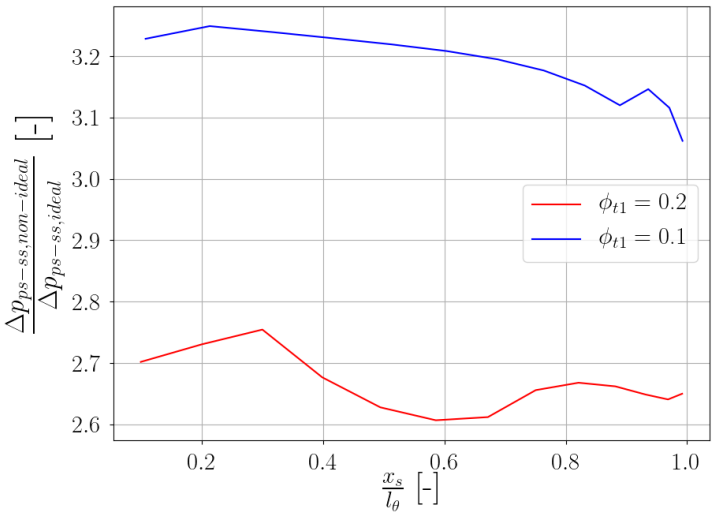

Figure 8.16: Effect of flow non-ideality on blade surface pressure difference. Fluid = R134a, ψ = 0.75

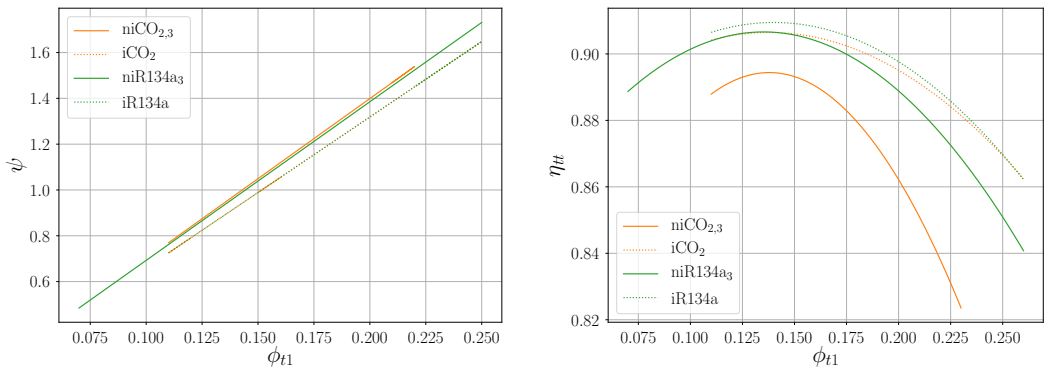

(a) (b)

Figure 8.17: Variation of the (a) optimum design locus and (b) maximum achievable efficiency at various cases listed in Table 8.4 for centrifugal compressors operating with β_{tt} = 2.5

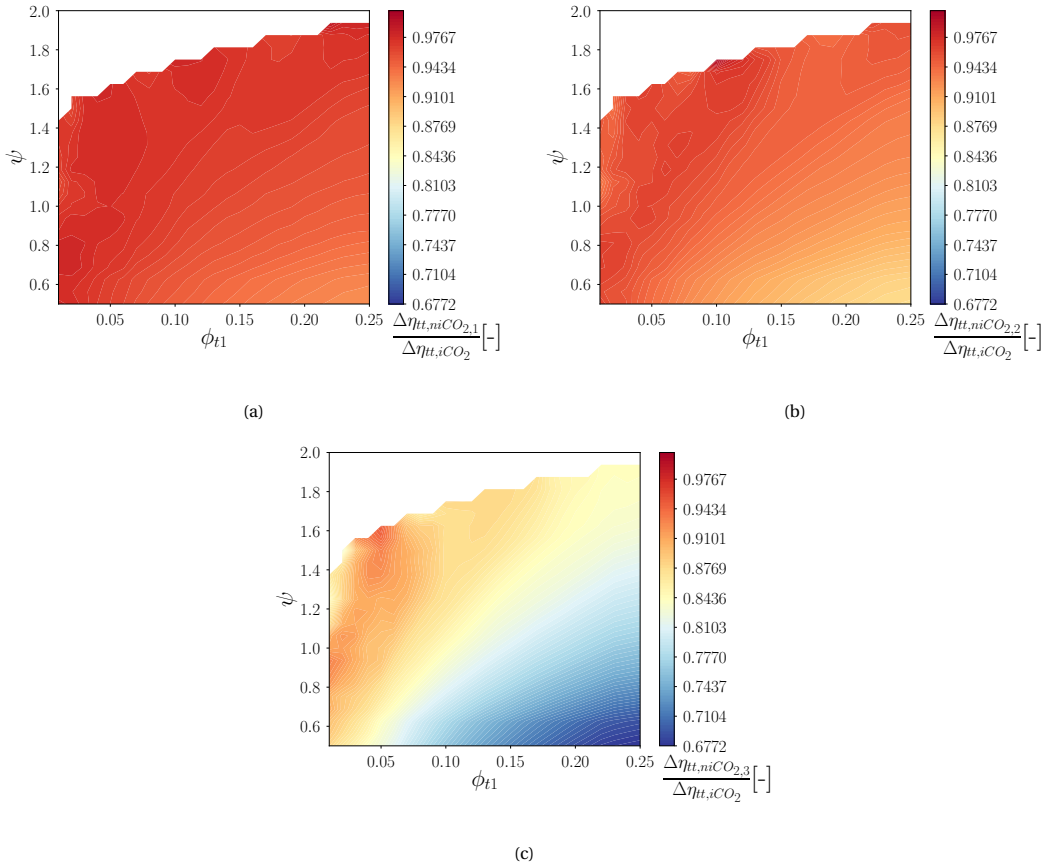

Figure 8.18: Efficiency drop induced by wake mixing with CO_2 as the working fluid for case: (a) $niCO_{2,1}$, (b) $niCO_{2,2}$ and (c) $niCO_{2,3}$. β_{tt} = 2.5. The value is normalized with $\Delta\eta_{tt,wakemixing}$ of CO_2 case: iCO_2. The reduced inlet thermodynamic properties as listed in Table 8.4

loss generation mechanism, however, may further consolidate or alter this trend. For example, the impact of flow non-ideality on efficiency drop induced by wake mixing is significant, even when computed using an empirical correlation, as shown in Figures 8.18 and 8.19. The increased sensitivity of $\Delta\eta_{tt,mixing}$ on ϕ_{t1}, for instance, indicates that the implementation of physics-based loss model for the wake mixing loss may change the decrease in maximum efficiency in Figure 8.17b and the optimum design locus shift in Figure 8.17a.

As a last remark, it is clear from the present analysis that the locus of optimal impeller efficiency is not only influenced by blade boundary and tip leakage loss. In turn, to better capture the influence of fluid molecular complexity and flow non-ideality on impeller performance trend, such as the position of the optimum design locus and the maximum efficiency limit, additional physics-based loss models have to be implemented orf other loss generation mechanisms such as wake mixing and secondary flow.

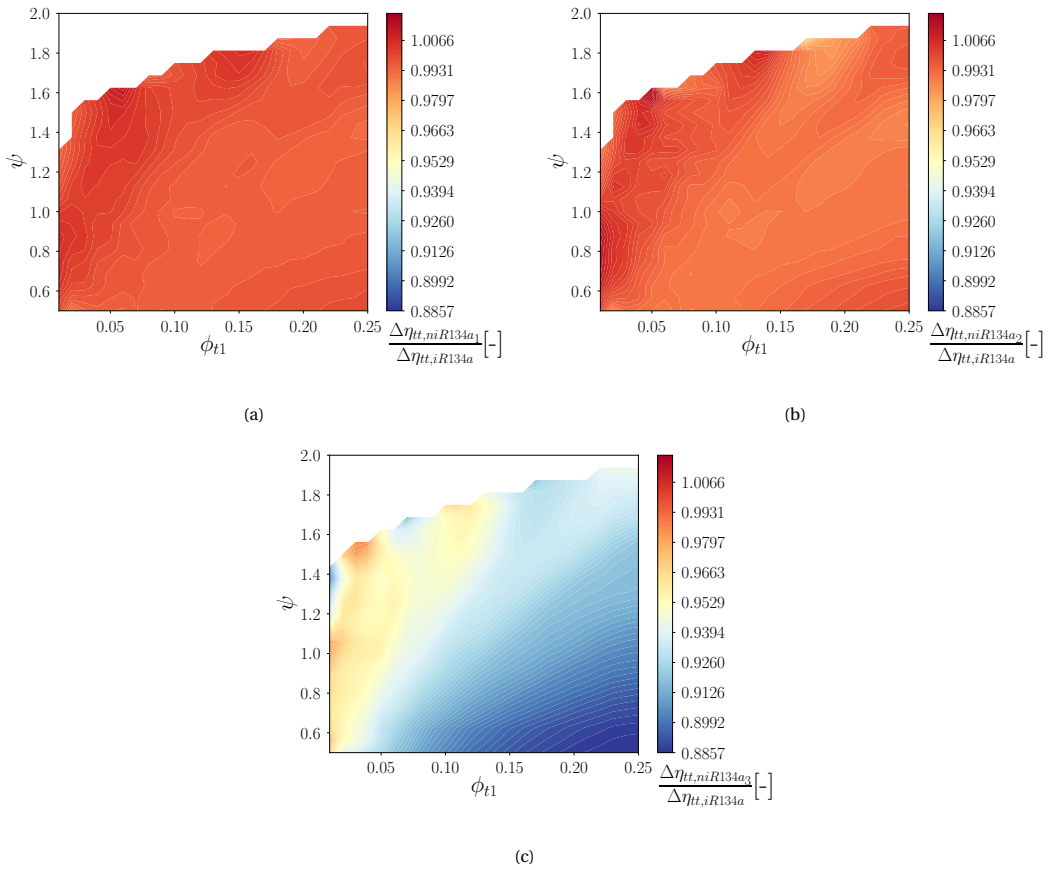

Figure 8.19: Efficiency drop induced by wake mixing with R134a as the working fluid for case: (a) niR134a$_1$, (b) niR134a$_2$ and (c) niR134a$_3$. β_{tt} = 2.5. The value is normalized with $\Delta\eta_{tt,wakemixing}$ of R134a case: iR134a. The reduced inlet thermodynamic properties as listed in Table 8.4

9

Conclusion and Recommendation

9.1. Conclusions

A general preliminary design guideline for centrifugal compressors operating with non-ideal compressible flows have been derived using physics-based loss models extended to arbitrary working fluids. The main findings of the current work can be summarized as follows:

- The generalized similarity equation valid for a generic centrifugal compressor operating with non-ideal compressible flows can be formularized by introducing the total-to-total compression ratio (β_{tt}) and the isentropic pressure-volume exponent (γ_{pv}). The two parameters replace the Mach number (M) and perfect gas heat capacity ratio (γ). The efficiency of a generic centrifugal compressor can be expressed as:

$$\eta_{tt} = f(\phi_{t1}, \psi, \beta_{tt}, \gamma_{pv}, Re, \sigma)$$

  .

- The average value of the isentropic pressure-volume exponent (γ_{pv}) can be used to characterize flow non-ideality effect. However, this parameter is a thermodynamic state variable. Thus, using this average value will cause the computed thermodynamic properties to deviate from the actual one in the presence of a strong (γ_{pv}) gradient along the thermodynamic process.

- The current work focuses on two loss generation mechanisms: the blade boundary layer loss and the tip leakage loss. The entropy generation induced by both loss models is strongly dependent on the blade surface flow velocity distribution. Some limitation on the developed physics-based loss models are:

  - conservatively fixed values of C_d = 0.002 and C_c = 0.8
  - linear mean relative velocity (w_{mean}) distribution between inlet and outlet

- The novel physics-based blade boundary layer and tip leakage loss models can predict a correct loss generation trend as compared with a higher-order numerical method, namely CFD. The deviation in the predicted efficiency drop induced by both loss models is within 1-3%.

- The trend maximum efficiency locus in the β_{tt}-ϕ_{t1} plane computed using the meanline program coupled with the physics-based loss models correctly reproduce the maximum efficiency locus trend obtained in the work of Casey [11]. The exact position of the locus computed using the physics-based loss models shifts towards higher values of ϕ_{t1}.

- An increase in fluid molecular complexity does not affect the position of optimum design locus in the ψ-ϕ_{t1} plane. However, a higher fluid molecular complexity increases the sensitivity of the computed efficiency drop induced by tip leakage to the duty coefficient (ψ and ϕ_{t1}) values. Moreover, a higher molecular complexity also decreases the efficiency drop induced by the blade boundary layer.

- The effect of flow non-ideality on the value and trend of both blade boundary layer and tip leakage loss generation is more prominent in flow with less molecular complexity. A higher flow non-ideality induces a higher efficiency drop due to blade boundary layer and tip leakage loss. Nevertheless, the position of optimum design locus in the ψ-ϕ_{t1} plane is only slightly shifted towards lower values of ϕ_{t1} due to the increased flow non-ideality.
- An increase in fluid molecular complexity and flow non-ideality decreases the overall impeller efficiency.

9.2. Recommendations

Based on the conclusions and limitations of the current work, some recommendations can be drawn for future studies.

- It is strongly suggested to investigate the physics-based modelling of the wake mixing loss. Fluid molecular complexity and flow non-ideality strongly affect the efficiency drop induced by wake mixing loss, even as the wake mixing loss is predicted using an empirical loss model. Using a physics-based wake mixing model has the potential to improve the accuracy of the meanline program. The jet-wake phenomena at impeller discharge discussed in the works of van den Braembussche[27] and Schneider [28] present a potential physics-based formulations and framework in wake mixing loss modelling. Using a physics-based wake mixing loss model will possibly highlight a stronger dependency of the impeller efficiency on the molecular complexity and flow non-ideality.
- Similarly, the development of a physics-based strategy to compute secondary flows loss can increase the accuracy and capability of the developed meanline program. The inherently separated flow near the impeller blade tip translates to the increased relevance of the secondary flow loss in centrifugal compressors.
- To improve the physics-based tip leakage loss model, it is important to implement also a physics-based model for the leakage flow. Replacing the current incompressible flow assumption for the tip leakage flow can prevent the use of empirical constants such as C_c, which in turn, can increase the accuracy of the model.
- Lastly, a more realistic mean relative velocity distribution between the impeller inlet and outlet may improve the accuracy of the entropy generation prediction of both the blade boundary layer loss and tip leakage loss. A more realistic mean relative velocity distribution results in a more accurate blade surface velocity distribution, which is the governing parameter of both loss models.

Bibliography

[1] A. Engeda. Early historical development of the centrifugal impeller. *ASME 98-GT-022*, June 1998. https://doi.org/10.1115/98-GT-022.

[2] C. B. Meher-Homji. The development of the whittle turbojet. *Journal of Engineering for Gas Turbines and Power*, 120(2), April 1998. https://doi.org/10.1115/1.2818112.

[3] Midland Air Museum. The jet engine and sir frank whittle, 2021. URL `http://www.midlandairmuseum.co.uk/jet.php`.

[4] S. L. Dixon and C. A. Hall. *Fluid Mechanics and Thermodynamics of Turbomachinery*. Elsevier Inc., 2014.

[5] A. Whitfield and N. C. Baines. *Design of Radial Turbomachines*. Longman Scientific & Technical, 1990.

[6] TU Delft. Nextgen ecs-based on the iorc concept, 2019. URL `https://www.tudelft.nl/en/ae/organisation/departments/aerodynamics-wind-energy-flight-performance-and-propulsion/flight-performance-and-propulsion/propulsion-power/research/ecs/`.

[7] A. Giuffre. Design guidelines for axial turbines operating with non-ideal compressible flows. Master's thesis, Politecnico di Milano, 2018.

[8] R. H. Aungier. Mean streamline aerodynamic performance analysis of centrifugal compressors. *Journal of Turbomachinery*, 117(3), July 1995. https://doi.org/10.1115/1.2835669.

[9] M. V. Casey and Robinson C. J. A guide to turbocharger compressor characteristics. *10. Symposium Dieselmotorentechnik*, July 1952.

[10] H. W. Oh, E. S. Yoon, and M. K Chung. An optimum set of loss models for performance prediction of centrifugal compressors. *Proceedings of the Institution of Mechanical Engineers, Part A: Journal of Power and Energy*, 211(4):331–338, 1997. doi:10.1243/0957650971537231.

[11] D. Rusch and M. V. Casey. The design space boundaries for high flow capacity centrifugal compressors. *Journal of Turbomachinery*, 135(3), March 2013. https://doi.org/10.1115/1.4007548.

[12] E. Buckingham. On physically similar systems; illustrations of the use of dimensional equations. *Physical Review*, 4(4), 1914. https://doi.org/10.1103/PhysRev.4.345.

[13] L. I. Lewis. *Turbomachinery Performance Analysis*. Elsevier Science & Technology Books, 1996.

[14] S. F. Smith. A simple correlation of turbine efficiency. *The Journal of the Royal Aeronautical Society*, 69 (655), 1965. https://doi.org/10.1017/S0001924000059108.

[15] E. Macchi and A. Perdichizzi. Efficiency prediction for axial-flow turbines operating with nonconventional fluids. *Journal of Engineering for Gas Turbines and Power*, 103(4), 1981. https://doi.org/10.1115/1.3230794.

[16] M. V. Casey. *Radial Turbomachinery Design*. Cambridge Turbomachinery Course 2008 academic year, 2012.

[17] P. Colonna and W. C. Reynolds. *Thermodynamics: Fundamentals and Engineering Applications*. Cambridge University Press, 2018.

[18] P. A. Thompson. A fundamental derivative in gasdynamics. *The Physics of Fluids*, 14(1843), 1971. https://doi.org/10.1063/1.1693693.

[19] P. Nederstigt. Real gas thermodynamics. Master's thesis, Delft University of Technology, 2017.

[20] D. A. Kouremenos. The normal shockwaves of real gases and the generalized isentropic exponents. *Forschung im Ingenieurwesen A*, 52(1), 1986. https://doi.org/10.1007/BF02558430.

[21] N. D. Baltadjiev, C. Lettieri, and Z. S. Spakovszky. An investigation of real gas effects in supercritical co 2 centrifugal compressors. *Journal of Turbomachinery*, 137(9), 2015. doi:10.1115/1.4029616.

[22] M. V. Herbert. *A Method of Performance Prediction for Centrifugal Compressors.* Her Majesty's Stationery Office, United Kingdom, 1980.

[23] W. Jansen. A method for calculating the flow in a centrifugal impeller when entropy gradients are present. *Royal Society Conference on Internal Aerodynamics (Turbomachinery)*, 1967.

[24] J. E. Coppage, et al. Study of supersonic radial compressors for refrigeration and pressurization systems. *WADC Report*, 55(257), 1956.

[25] J. P. Johnston and R. C. Dean Jr. Losses in vaneless diffusers of centrifugal compressors and pumps. analysis, experiment and design. *Journal of Engineering for Gas Turbines and Power*, 88(1), 1966. https://doi.org/10.1115/1.3678477.

[26] D. Eckardt. Detailed flow investigations within a high-speed centrifugal compressor impeller. *Journal of Fluids Engineering*, 98(3), 1976. https://doi.org/10.1115/1.3448334.

[27] R. Van den Braembussche. *Design and Analysis of Centrifugal Compressors.* ASME Press and John Wiley & Sons Ltd, 2019.

[28] M. Schneider, et al. Analytical loss prediction for turbocharger compressors. *Proceedings of 11th European Conference on Turbomachinery Fluid dynamics & Thermodynamics*, 11, March 2015.

[29] O. E. Balje. A contribution to the problem of designing radial turbomachines. *Transactions of the American Society of Mechanical Engineers*, 74(451), 1952.

[30] J. D. Denton. Loss mechanisms in turbomachineries. *Journal of Turbomachinery*, 115(4), 1993. https://doi.org/10.1115/1.2929299.

[31] C.H. Wu. A general theory of 3d flow in subsonic and supersonic turbomachines of axial, radial and mixed flow types. *National Advisory Committee for Aeronautics, Technical Note*, 2604, 1952.

[32] J. D. Stanitz and V. D. Prian. A rapid approximate method for determining velocity distribution on impeller blades of centrifugal compressors. *National Advisory Committee for Aeronautics, Technical Note*, 2421, 1951.

[33] J. Kramer, W. Osborn, and J. Hamrick. Design and tests of mixed flow and centrifugal impellers. *Journal of Engineering for Gas Turbines and Power*, 82(2), 1960. https://doi.org/10.1115/1.3672731.

[34] F. Bhinder and D. Ingham. The effect of inducer shape in the performance of high pressure ratio centrifugal compressors. *ASME 74-GT-122*, 1974. https://doi.org/10.1115/74-GT-122.

[35] H. Harada. Performance characteristics of shrouded and unshrouded impellers of a centrifugal compressor. *Journal of Engineering for Gas Turbines and Power*, 107(2), 1985. https://doi.org/10.1115/1.3239765.

[36] J. A. Storer. *Tip Clearance Flow in Axial Compressors.* PhD thesis, Cambridge University, United Kingdom, 1991.

[37] E. M. Greitzer, C. S. Tan, and M. B. Graf. *Internal flow concepts and applications.* Cambridge University Press, 2004.

[38] J. Moore and J. S. Tilton. Tip leakage flow in a linear turbine cascade. *Journal of Turbomachinery*, 110(1), 1988. https://doi.org/10.1115/1.3262162.

[39] G. Morphis and J. P. Bindon. The effects of relative motion, blade edge radius and gap size on the blade tip pressure distribution in an annular turbine cascade with clearance. *ASME 88-GT-256*, 1988. https://doi.org/10.1115/88-GT-256.

[40] M. I. Yaras and S. A. Sjolander. Effects of simulated rotation on tip leakage in a planar cascade of turbine blades. parts 1 and 2. *Journal of Turbomachinery*, 114(3), 1992. https://doi.org/10.1115/1.2929189.

[41] F. J. Wiesner. A review of slip factors for centrifugal impellers. *Journal of Engineering for Gas Turbines and Power*, 89(4), 1967. https://doi.org/10.1115/1.3616734.

[42] S. N. M. J. Al-Zubaidy. Axial length influence on the performance of centrifugal impellers. *Journal of Propulsion and Power*, 8(6), 1992. https://doi.org/10.2514/3.51342.

[43] J. D. Denton. Multall—an open source, computational fluid dynamics based, turbomachinery design system. *Journal of Turbomachinery*, 139(12), 2017. https://doi.org/10.1115/1.4037819.

[44] J. D. Denton. The calculation of three-dimensional viscous flow through multistage turbomachines. *Journal of Turbomachinery*, 114(1), 1992. https://doi.org/10.1115/1.2927983.

[45] S.A. Sjolander. Secondary and tip-clearance flows in axial turbines. *VKI Lecture Series*, 1997.

[46] H Schlichting and K Gersten. *Boundary-Layer Theory*, volume 9^{th}. Springer, 2017.

[47] ESDU. A guide to fan selection and performance. *ESDU*, 79037, 1980.

[48] I. N. Moyle. Analysis of efficiency sensitivity associated with tip clearance in axial flow compressors. *Journal of Turbomachinery*, 112, 1990. https://doi.org/10.1115/88-GT-216.

[49] J. Harinc, A. Guardone, and P. Colonna. The influence of molecular complexity on expanding flows of ideal and dense gases. *Physics of Fluids*, 21(8), 2009. https://doi.org/10.1063/1.3194308.

[50] R. Pecnic, E. Rinaldi, and Colonna P. Computational fluid dynamics of a radial compressor operating with supercritical CO_2. *Journal of Engineering for Gas Turbines and Power*, 134(12), 2012. https://doi.org/10.1115/1.4007196.

[51] A. R. Howell. Design of axial compressors. *Proceedings of the Institution of Mechanical Engineers*, 153(1), 1945. doi.org/10.1243/PIME_PROC_1945_153_050_02.

A

Effect of Compression Ratio on Performance of Non-Conventional Impeller

As an extension to the previous analysis regarding molecular complexity effect, CO_2 and R134a are chosen. To avoid including any NICFD effect, the reduced inlet thermodynamic properties are taken at the dilute gas region as in Table 8.3. The performance for both working fluids are performed under:

- $\beta_{tt} = 2.5$
- $\beta_{tt} = 3.5$
- $\beta_{tt} = 5$

The variation is limited until compression ratio 5 as a limit case of an impeller. As seen in Casey's graph (Figure 7.1a), increasing the design compression ratio causes a drop in optimum impeller efficiency. Moreover, from the same figure, it is implied that an increase in compression ratio will severely narrow the compressor optimum design range. Thus, in practice, an additional compressor stage is used to achieve a higher compression ratio. Based on the previous choices, the impact of compression ratio to impeller performance can be seen in Figures A.1 - A.4. Some key takeaways are:

- the sensitivity of $\Delta\eta_{tt,BL}$ to the value of ϕ_{t1} is generally increased with increasing compression ratio. In the optimum design region (between ϕ_{t1} = 0.10 - 0.12 and ψ = 0.9 - 1.1), however, the absolute efficiency drop value is similar

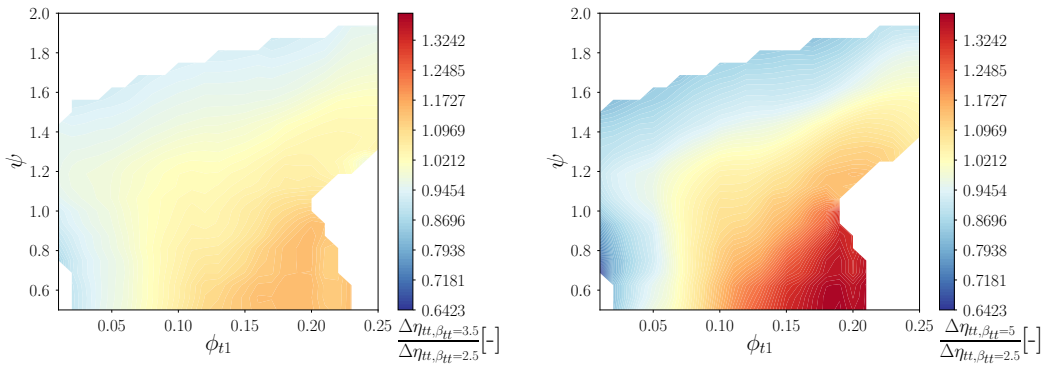

(a) (b)

Figure A.1: Efficiency drop induced by blade boundary layer loss; CO_2 as the working fluid. With: (a) β_{tt} = 3.5 and (b) β_{tt} = 5. The value is normalized with $\Delta\eta_{tt,BL}$ of CO_2 at β_{tt} = 2.5

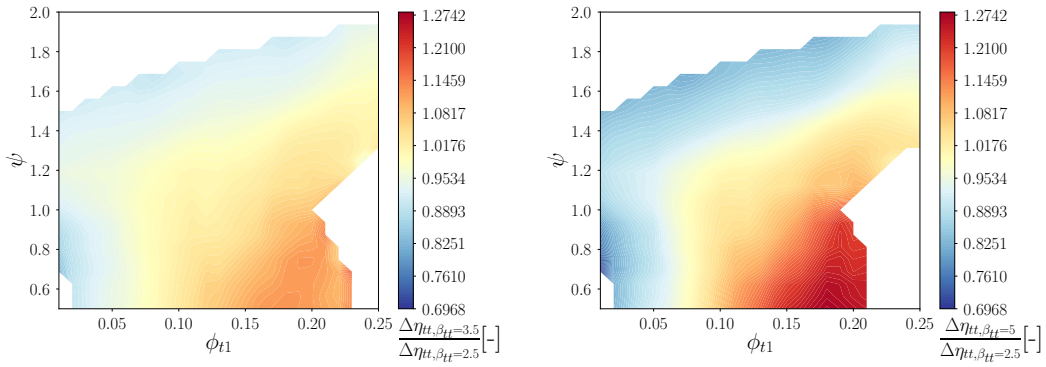

(a) (b)

Figure A.2: Efficiency drop induced by blade boundary layer loss; R134a as the working fluid. With: (a) $\beta_{tt} = 3.5$ and (b) $\beta_{tt} = 5$. The value is normalized with $\Delta\eta_{tt,BL}$ of R134a at $\beta_{tt} = 2.5$

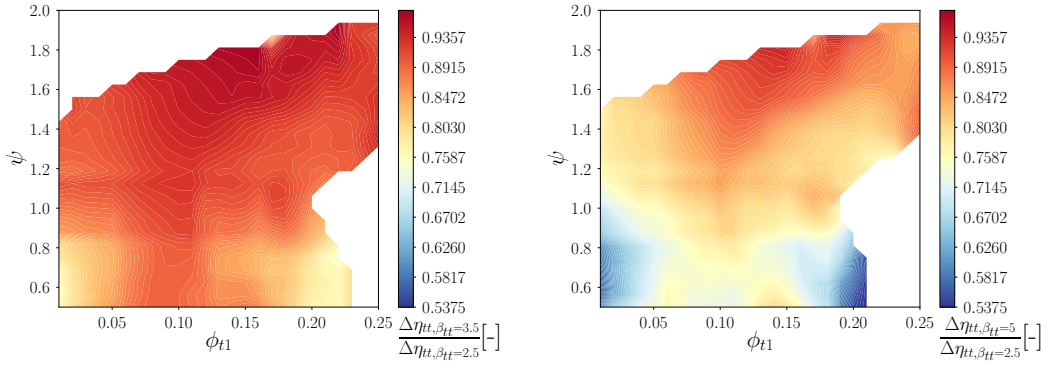

(a) (b)

Figure A.3: Efficiency drop induced by tip leakage loss; CO_2 as the working fluid. With: (a) $\beta_{tt} = 3.5$ and (b) $\beta_{tt} = 5$. The value is normalized with $\Delta\eta_{tt,tipleakage}$ of CO_2 at $\beta_{tt} = 2.5$

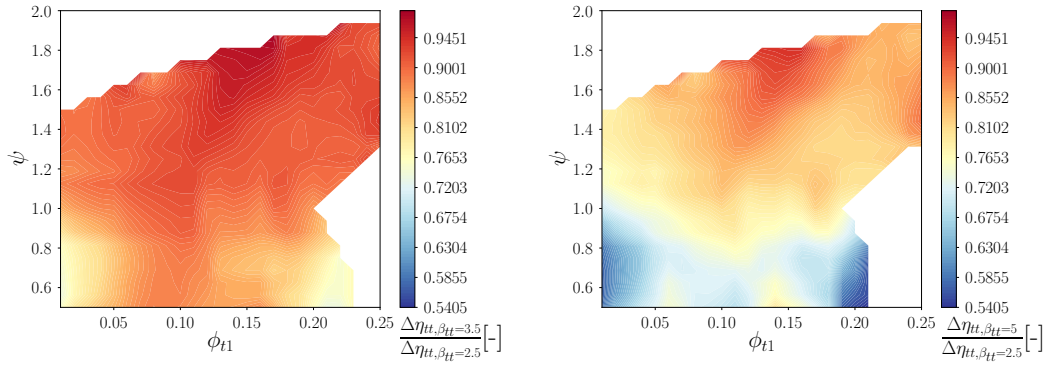

(a) (b)

Figure A.4: Efficiency drop induced by tip leakage loss; R134a as the working fluid. With: (a) β_{tt} = 3.5 and (b) β_{tt} = 5. The value is normalized with $\Delta\eta_{tt,tipleakage}$ of R134a at β_{tt} = 2.5

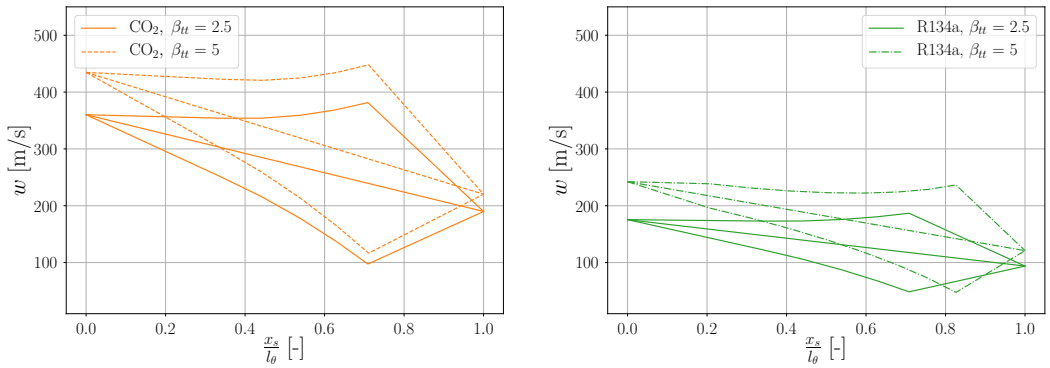

(a) (b)

Figure A.5: Effect of compression ratio on blade surface velocity distribution, at ϕ_{t1} = 0.16 and ψ = 1.0, for (a) CO_2 and (b) R134a as working fluid

- the sensitivity of $\Delta\eta_{tt,tipleakage}$ to the value of ψ is increased with increasing compression ratio
- there is little difference in the effect of compression ratio on the trend of efficiency drop caused by boundary layer loss and tip leakage loss of compressors utilizing different working fluids

The increased sensitivity of the blade boundary loss to ϕ_{t1} with increasing compression ratio may be explained mathematically. Increasing the compression ratio implies an increase in the compressor isentropic work. Referring back to the definition of work coefficient (Equation 5.9), in a constant ψ value, this isentropic work increase leads to an increase in impeller peripheral speed. Based on the definition of flow coefficient (Equation 2.23), a higher impeller peripheral speed leads to a higher increase in meridional velocity (v_m) when increasing the ϕ_{t1}. As the meridional velocity governs the impeller velocity triangle, the change of entropy generation with an increase in flow coefficient is augmented. Similarly, a higher isentropic work implies a larger impeller peripheral speed drop when increasing the working coefficient. With a constant value of ϕ_{t1}, a lower peripheral speed also means a lower meridional velocity. The entropy generation reduction with reduction of work coefficient is, in turn, amplified.
On the other hand, comparing the effect of compression ratio on the performance of compressors with two different working fluid, it is clear that the effect of compression ratio on the trend of efficiency drop induced by boundary layer loss and tip leakage loss in both cases is similar. This similarity can be traced back to the governing equation of both of the loss models (Equations 4.14 and 4.37). Boundary layer loss is a function of the flow velocity (v_e) and flow density (ρ_e). The increase of blade surface velocity is diminished in fluids with higher molecular complexity, as seen in Figure A.5. Nevertheless, the increase in molecular complexity also leads to a higher density. The contribution of ρ_e value lessens the effect of the lower increase of blade sur-

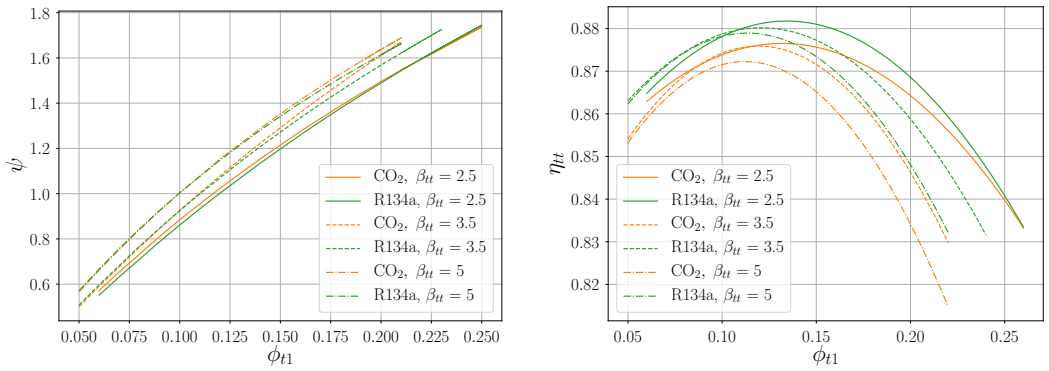

(a) (b)

Figure A.6: Variation of the (a) optimum efficiency locus and (b) maximum achievable efficiency at increasing values of β_{tt} for centrifugal compressors operating with CO_2 and R134a as working fluid

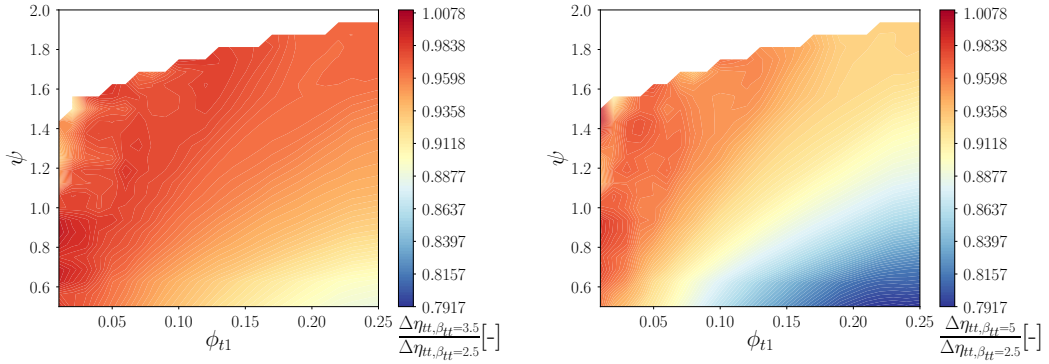

(a) (b)

Figure A.7: Efficiency drop induced by wake mixing; CO_2 as the working fluid. With: (a) β_{tt} = 3.5 and (b) β_{tt} = 5. The value is normalized with $\Delta\eta_{tt,wakemixing}$ of CO_2 at β_{tt} = 2.5

face velocity in the case with higher fluid molecular complexity. Similarly, the tip leakage loss is proportional to the pressure-suction velocity difference and the square root of the flow density. In the case with higher working fluid molecular complexity, the increase in blade surface velocity difference is lower than in the case with lower working fluid molecular complexity. Nevertheless, the high fluid density of the case with higher working fluid molecular complexity weakens the effect of the low increase in blade surface velocity. Due to these balancing effects, there is no noticeable difference in the entropy generation trend due to both the blade boundary layer and the tip leakage in cases with different molecular complexity. Similar to the analysis of the effect of molecular complexity in the previous section, the effect of compression ratio on impeller performance can also be performed. Some key information gained from this analysis are:

- increasing compression ratio will cause a leftward shift (towards lower flow coefficient) of the maximum efficiency locus, as seen in Figure A.6a.
- The locus shift is similar in cases with different working fluid molecular complexity
- n terms of absolute maximum optimum efficiency value shift, increasing the compression ratio will lower the overall optimum efficiency

As seen in Figure A.6a, a higher compression ratio will cause a leftward shift of the optimum design locus in the ψ-ϕ_{t1} graph. This shift is caused by the increased sensitivity of the boundary layer loss on the ϕ_{t1} coefficient value at a higher compression ratio. Moreover, this shift may be even more pronounced implementing physics-based loss models for wake mixing entropy generation. As seen in the Figures A.7 and A.8, the entropy generation due to wake mixing loss also exhibits increased sensitivity in higher compression ratio. This

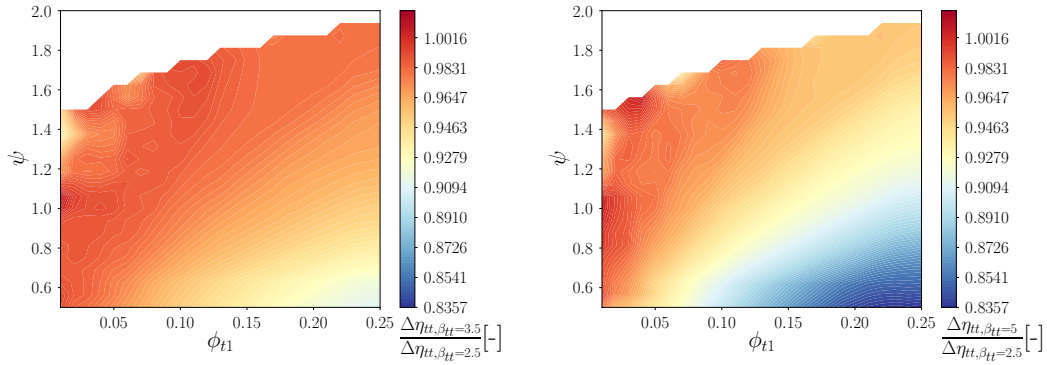

(a) (b)

Figure A.8: Efficiency drop induced by wake mixing; R134a as the working fluid. With: (a) β_{tt} = 3.5 and (b) β_{tt} = 5. The value is normalized with $\Delta\eta_{tt,wakemixing}$ of R134a at β_{tt} = 2.5; Value obtained using empirical correlation in Table 4.1

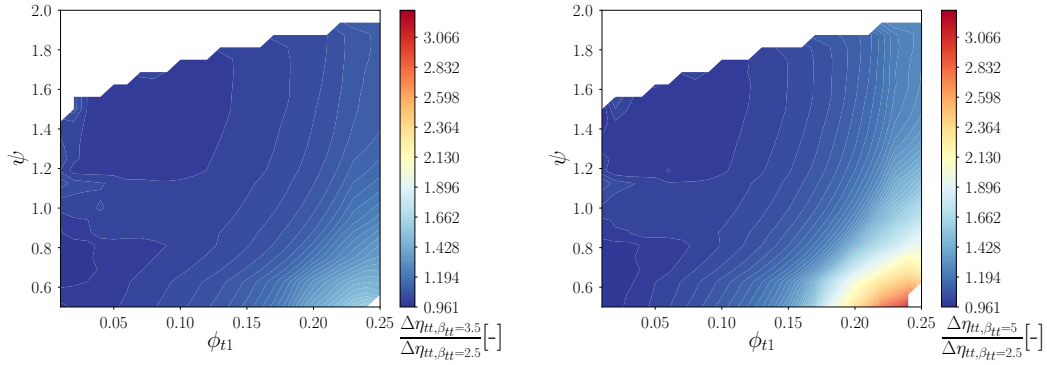

(a) (b)

Figure A.9: Efficiency drop induced by blade loading loss (part of secondary flow loss); CO_2 as the working fluid. With: (a) β_{tt} = 3.5 and (b) β_{tt} = 5. The value is normalized with $\Delta\eta_{tt,bladeloading}$ of CO_2 at β_{tt} = 2.5; Value obtained using empirical correlation in Table 4.1

sensitivity implies that the wake mixing loss has the potential to greatly affect the position of the optimum design locus. Additionally, although the effect of compression ratio on the trend of entropy generation does not seem to differ in cases with different working fluid molecular complexity, as seen in Figures A.7 and A.8, it must be understood both figures are computed using an empirical correlation, which may diminish the effect of fluid molecular complexity. Implementing a physics-based wake mixing model, such as the jet-wake flow model [27] [28] mentioned in Chapter 4, may remedy this problem.

Focusing on Figure A.6b, the efficiency drop with increasing β_{tt} is seemingly contradictory to the previous findings for the effect of compression ratio on efficiency drop due to boundary and tip leakage loss. The reason for this contradiction may lie in the entropy generation due to secondary flow. As shown in Figures A.9 and A.10, the efficiency drop due to secondary flow is greatly increased in a high compression ratio. This increase is physically sound, as a high compression ratio the results in a high adverse pressure gradient, increasing the severity of flow separation. In similar fashion with the mixing loss, further developments in the physics-based secondary flow loss model can improve the trend in Figure A.6b.

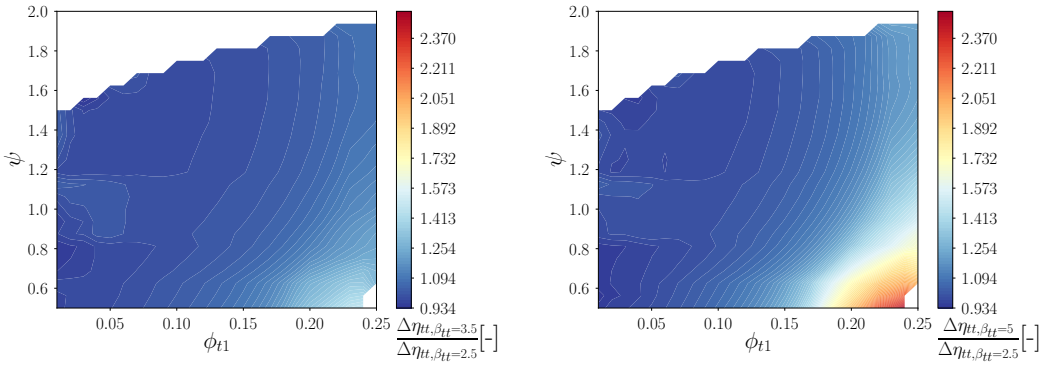

(a) (b)

Figure A.10: Efficiency drop induced by blade loading loss (part of secondary flow loss); R134a as the working fluid. With: (a) β_{tt} = 3.5 and (b) β_{tt} = 5. The value is normalized with $\Delta\eta_{tt,bladeloading}$ of R134a at β_{tt} = 2.5; Value obtained using empirical correlation in Table 4.1

B

Input Eckardt-O Impeller Geometry for Stagen.dat

```
 ********************** ROW NUMBER           1
 **********STARTING NEW BLADE SECTION, SECTION NUMBER       1
************************BLANK LINE****************************
    1                   INTYPE- TYPE OF BLADE GEOMETRY INPUT
    6  300    7         NPIN, NXPTS, NSMOOTH
0.0000           -32.8854           BLADE CENTRE LINE ANGLES
0.1337           -29.2527           BLADE CENTRE LINE ANGLES
0.3181           -23.7921           BLADE CENTRE LINE ANGLES
0.5281           -16.9688           BLADE CENTRE LINE ANGLES
0.7566           -8.9438           BLADE CENTRE LINE ANGLES
1.0000           0.0000           BLADE CENTRE LINE ANGLES
0.0150     0.0150       0.0150     0.3000    0.0200     0.0200       2.0000            BLADE SPECIFICATION
1.0000     1.0000       1.0000       FCHORD, FPERP, FTKSCALE
-0.0000     0.5000       0.5000                    ROTN,XROT,YROT
0.5000    0.2500  -32.8854     0.0000      XCUP, XCDWN, BETUP, BETDWN
  BLANK LINE
52              NUMBER OF POINTS ON THE STREAM SURFACE.
-0.02000    0.00000    0.00521    0.01042    0.01563    0.02084    0.02605   0.03126
0.03647    0.04168    0.04689    0.05210    0.05731    0.06253    0.06774   0.07295
0.07816    0.08337    0.08858    0.09379    0.09900    0.10421    0.10942   0.11463
0.11984    0.12505    0.13000    0.13000    0.13000    0.13000    0.13000   0.13000
0.13000    0.13000    0.13000    0.13000    0.13000    0.13000    0.13000   0.13000
0.13000    0.13000    0.13000    0.13000    0.13000    0.13000    0.13000   0.13000
0.13000    0.13000    0.13000    0.13000
0.04500    0.04500    0.04506    0.04523    0.04570    0.04700   0.04886    0.05053
0.05259    0.05478    0.05711    0.05956    0.06244    0.06586   0.06919    0.07302
0.07733    0.08205    0.08679    0.09205    0.09791    0.10477   0.11302    0.12394
0.13907    0.16222    0.20011    0.20552    0.21350    0.22169   0.22983    0.23797
0.24611    0.25426    0.26240    0.27054    0.27868    0.28682   0.29497    0.30311
0.31125    0.31939    0.32754    0.33568    0.34382    0.35196   0.36010    0.36825
0.37639    0.38453    0.39267    0.40000
0.00000       0.13000       0.04500       0.20011       LEADING AND TRAILING EDGE COORDINATES
 2.000     0.000     0.000     0.000     0.000   FCENTROID, FTANG, FLEAN, FSWEEP, FAXIAL
1.0000    0.0000                              FSCALE, FCONST
```

```
 ********************** ROW NUMBER           1
 **********STARTING NEW BLADE SECTION, SECTION NUMBER       5
************************BLANK LINE****************************
    1                   INTYPE- TYPE OF BLADE GEOMETRY INPUT
    6  300    7         NPIN, NXPTS, NSMOOTH
0.0000           -62.9981           BLADE CENTRE LINE ANGLES
0.1337           -59.5341           BLADE CENTRE LINE ANGLES
0.3181           -53.2298           BLADE CENTRE LINE ANGLES
0.5281           -42.8041           BLADE CENTRE LINE ANGLES
0.7566           -25.5326           BLADE CENTRE LINE ANGLES
1.0000           0.0000           BLADE CENTRE LINE ANGLES
0.0156     0.0156       0.0156     0.3000    0.0200     0.0200       2.0000            BLADE SPECIFICATION
1.0000     1.0000       1.0000       FCHORD, FPERP, FTKSCALE
0.0000     0.5000       0.5000                   ROTN,XROT,YROT
0.5000    0.2500  -62.9981     0.0000      XCUP, XCDWN, BETUP, BETDWN
  BLANK LINE
52              NUMBER OF POINTS ON THE STREAM SURFACE.
-0.02000    0.00000    0.00417    0.00834    0.01251    0.01667    0.02084   0.02501
0.02918    0.03335    0.03752    0.04168    0.04585    0.05002    0.05419   0.05836
0.06253    0.06669    0.07086    0.07503    0.07920    0.08337    0.08754   0.09170
0.09587    0.10004    0.10402    0.10446    0.10490    0.10534    0.10579   0.10623
0.10667    0.10711    0.10755    0.10799    0.10843    0.10887    0.10931   0.10975
0.11019    0.11064    0.11108    0.11152    0.11196    0.11240    0.11284   0.11328
0.11372    0.11416    0.11460    0.11500
0.14000    0.14000    0.14000    0.14000    0.14000    0.14000   0.14001    0.14001
0.14002    0.14003    0.14004    0.14006    0.14007    0.14009   0.14012    0.14075
0.14258    0.14483    0.14739    0.15035    0.15349    0.15740   0.16181    0.16738
0.17447    0.18365    0.20091    0.22581    0.23387    0.24253   0.24974    0.25648
0.26190    0.26499    0.26992    0.28173    0.28808    0.29469   0.30043    0.30654
0.31376    0.31979    0.32681    0.33491    0.34172    0.34692   0.35418    0.36170
0.36796    0.37336    0.38020    0.40000
0.00000       0.10402       0.14000       0.20091       LEADING AND TRAILING EDGE COORDINATES
 2.000     0.000     0.000     0.000     0.000   FCENTROID, FTANG, FLEAN, FSWEEP, FAXIAL
1.0000    0.0000                              FSCALE, FCONST
```